

## Towards labonachip optical trapping and Raman spectroscopy of extracellular vesicles using multiwaveguide traps

Loozen, G.B.

**DOI**

[10.4233/uuid:99f7be1f-af10-4f12-8331-f1d65c76bd8e](https://doi.org/10.4233/uuid:99f7be1f-af10-4f12-8331-f1d65c76bd8e)

**Publication date**

2023

**Document Version**

Final published version

**Citation (APA)**

Loozen, G. B. (2023). *Towards labonachip optical trapping and Raman spectroscopy of extracellular vesicles using multiwaveguide traps*. [Dissertation (TU Delft), Delft University of Technology]. <https://doi.org/10.4233/uuid:99f7be1f-af10-4f12-8331-f1d65c76bd8e>

**Important note**

To cite this publication, please use the final published version (if applicable). Please check the document version above.

**Copyright**

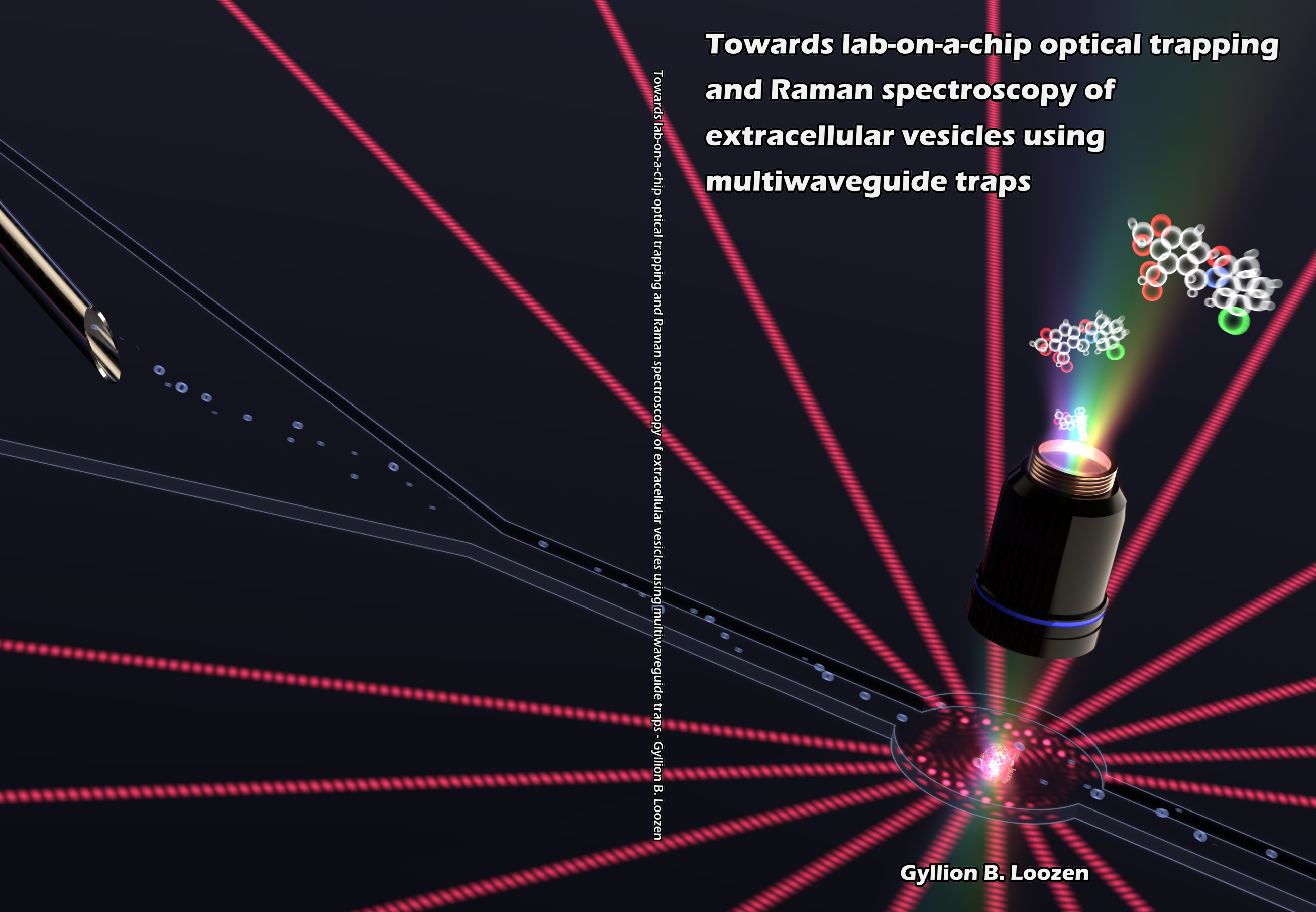
Other than for strictly personal use, it is not permitted to download, forward or distribute the text or part of it, without the consent of the author(s) and/or copyright holder(s), unless the work is under an open content license such as Creative Commons.

**Takedown policy**

Please contact us and provide details if you believe this document breaches copyrights. We will remove access to the work immediately and investigate your claim.

# Towards lab-on-a-chip optical trapping and Raman spectroscopy of extracellular vesicles using multiwaveguide traps

Towards lab-on-a-chip optical trapping and Raman spectroscopy of extracellular vesicles using multiwaveguide traps - Gyllion B. Loozen



Gyllion B. Loozen

**Towards lab-on-a-chip optical trapping  
and Raman spectroscopy of extracellular  
vesicles using multi-waveguide traps**



# **Towards lab-on-a-chip optical trapping and Raman spectroscopy of extracellular vesicles using multi-waveguide traps**

## **Proefschrift**

ter verkrijging van de graad van doctor  
aan de Technische Universiteit Delft,  
op gezag van de Rector Magnificus prof. dr. ir. TH.J.J. van der Hagen,  
voorzitter van het College voor Promoties,  
in het openbaar te verdedigen op donderdag 23 maart 2023 om 12.30 uur

door

**Gyllion Brian LOOZEN**

Natuurkundig Ingenieur,  
Technische Universiteit Delft, Delft, Nederland,  
geboren te Willemstad, Curaçao.

Dit proefschrift is goedgekeurd door de

promotor: Prof. dr. ir. L.J. van Vliet

promotor: Prof. dr. S. Stallinga

Samenstelling promotiecommissie:

Rector Magnificus,	voorzitter
Prof. dr. ir. L.J. van Vliet,	Technische Universiteit Delft
Prof. dr. S. Stallinga,	Technische Universiteit Delft

*Onafhankelijke leden:*

Dr. B.I. Avci,	Vrije Universiteit Amsterdam
Dr. P. Oostrum,	Universität für Bodenkultur Wien
Prof. dr. B. Rieger,	Technische Universiteit Delft
Prof. dr. S. Groeblacher,	Technische Universiteit Delft
Dr. N. Bhattacharya,	Technische Universiteit Delft



The work described in this thesis was conducted at the Quantitative Imaging section within the Impphys department at Delft University of Technology, The Netherlands. This work was supported by the Netherlands Organisation for Scientific Research - Domain Applied and Engineering Sciences (NWO-TTW), under the perspectief program Cancer-ID (project: 14197)

**Keywords:** optical trapping, Raman spectroscopy, lab-on-chip, extracellular vesicles

**Printed by:** Ridderprint|www.ridderprint.nl

**Cover design:** R.J. Moerland

Copyright © 2022 by G.B. Loozen, The Netherlands. All rights reserved. No parts of this thesis may be reproduced, stored in a retrieval system or transmitted in any form or by any means without permission of the author. Alle rechten voorbehouden. Niets uit deze uitgave mag worden vermenigvuldigd in enige vorm of op enige wijze, zonder voorafgaande schriftelijke toestemming van de auteur.

ISBN 978-94-6458-997-9

An electronic version of this dissertation is available at  
<http://repository.tudelft.nl/>.

*To God, my wife Damaris, our son Benjamin,  
my parents Leo & Sharine and my brother Dylan.*

Gyllion Brian Loozen



# Contents

<b>Summary</b>	<b>ix</b>
<b>Samenvatting</b>	<b>xi</b>
<b>1 Introduction</b>	<b>1</b>
1.1 Extracellular vesicles as bio-markers for disease identification . . .	1
1.2 Opto-fluidic lab-on-a-chip devices for single EV characterization . .	1
1.3 Raman scattering and spectroscopy. . . . .	2
1.4 Optical trapping . . . . .	4
1.5 On-chip trapping and Raman spectroscopy . . . . .	7
1.6 Research goal and thesis outline . . . . .	8
References. . . . .	9
<b>2 On-chip optical trapping of extracellular vesicles using box-shaped composite SiO<sub>2</sub>-Si<sub>3</sub>N<sub>4</sub> waveguides</b>	<b>13</b>
2.1 Introduction. . . . .	14
2.2 Device geometry and optical models for EVs. . . . .	15
2.3 Simulation approach. . . . .	16
2.4 Waveguide mode, emitted beam, and energy density in the trap . .	18
2.5 Force characteristics of the traps . . . . .	21
2.6 Trapping potentials . . . . .	24
2.7 Trapping stability. . . . .	25
2.8 Conclusion and outlook . . . . .	28
2.9 Funding . . . . .	29
2.10 Acknowledgements . . . . .	29
References. . . . .	29
<b>3 Multi-waveguide devices for optical trapping and Raman spectroscopy: design, fabrication &amp; performance demonstration</b>	<b>33</b>
3.1 Introduction. . . . .	34
3.2 Design of the multi-waveguide devices for trapping and Raman spectroscopy . . . . .	35
3.2.1 The excitation waveguides, their circuitry and their arrangement around the microbath . . . . .	36
3.2.2 Detection waveguides and their circuitry. . . . .	39
3.2.3 The microbath . . . . .	40
3.3 Experimental . . . . .	40
3.3.1 Fabrication of the multi-waveguide devices . . . . .	40
3.3.2 Experimental setup and sample preparation . . . . .	43

3.4	Results and Discussion . . . . .	44
3.4.1	Optical trapping with a 2-waveguide trap and a 16-waveguide trap . . . . .	44
3.4.2	Raman spectroscopy with the 2-waveguide trap and the 16-waveguide trap . . . . .	48
3.5	Conclusion . . . . .	49
3.6	Acknowledgements . . . . .	50
3.7	Funding . . . . .	50
	References . . . . .	50
<b>4</b>	<b>Trapping study of <i>Bacillus subtilis</i> spores in a 16 waveguide optical trap</b>	<b>53</b>
4.1	Introduction . . . . .	54
4.2	Materials and methods . . . . .	55
4.2.1	Experimental setup and sample preparation . . . . .	55
4.2.2	Trap stiffness measurement . . . . .	56
4.2.3	Data analysis and simulation . . . . .	58
4.3	Results and discussion . . . . .	61
4.4	Conclusion . . . . .	71
	References . . . . .	72
<b>5</b>	<b>Conclusion and outlook</b>	<b>75</b>
5.1	Conclusions . . . . .	76
5.2	Outlook . . . . .	80
	References . . . . .	82
	<b>Appendices</b>	<b>85</b>
<b>A</b>	<b>Particle tracking algorithm</b>	<b>87</b>
<b>B</b>	<b>Expected maximum intensity of a speckle pattern</b>	<b>93</b>
	References . . . . .	95
	<b>Curriculum Vitæ</b>	<b>97</b>
	<b>List of Publications</b>	<b>99</b>
	<b>Acknowledgements</b>	<b>101</b>

# Summary

Extracellular vesicles (EVs) are gaining attention for their applicability as biomarker in the identification of cancer. All cells release EVs into their environment, and the EVs carry information on their parent cell. Identification of EVs from tumour cells, however, calls for detection techniques with high sensitivity and specificity. In this regard, laser tweezer Raman spectroscopy (LTRS) is an attractive technique where highly confined optical fields are used to immobilize single EVs through optical trapping and to simultaneously generate a Raman signal for EV identification based on biomolecular composition. Lab-On-a-Chip (LOC) technology enables on-chip LTRS building blocks combined with microfluidic channels for EV supply. This has the potential for realising a compact and cheap device for EV identification and disease diagnosis.

This thesis presents the development of a LOC building block for combined on-chip optical trapping and Raman spectroscopy of single EVs. The building block is made-up of multiple optical waveguides terminating at the side-walls of a micro-fluidic channel. The coherent, counter-propagating beams from the waveguides interfere in the channel and form an optical interference pattern with multiple hotspots of strongly confined light, each suitable for optical trapping and Raman spectroscopy.

Firstly, an in-depth simulation study aimed at investigating the capabilities and limitations of a dual-waveguide trap for stable on-chip optical trapping of EVs is presented. The optical fields generated within a microfluidic channel are simulated with 3D finite-difference time-domain (FDTD) simulations. The optical forces acting on the EV and the attendant trap potentials follow from the simulated fields. Application of Ashkin's criterion yields a comprehensive overview of stable trapping conditions for EVs in terms of EV diameter and refractive index, and the injected optical power.

Then, novel multi-waveguide traps are designed and fabricated. These designs aim for stronger light confinement in the channel, resulting in improved optical trapping and Raman signal generation. The performance of a 2-waveguide and 16-waveguide trap are characterised using polystyrene beads. Optical trapping is quantified through trap stiffness values obtained both from experiments and from FDTD simulations. The two traps are compared through the stiffness values and the recorded Raman signal strength of the beads.

Finally, the 16-waveguide trap is used to demonstrate optical trapping of *B. subtilis* spores, as an intermediate step towards EVs. Optical trapping of the spores is studied with both experiments and simulations. Special attention is paid to the effect of random phase differences between the beams exiting the waveguides on the optical trap quality.



# Samenvatting

Buitencellulaire blaasjes (Extracellular Vesicles, EVs) krijgen steeds meer aandacht voor hun toepasbaarheid als biomarker bij de identificatie van kanker. Alle cellen laten EV's vrij in hun omgeving en de EV's dragen informatie over hun cel van afkomst. Identificatie van EV's afkomstig van tumorcellen vereist echter detectietechnieken met een hoge gevoeligheid en specificiteit. In dit opzicht is optisch pincet Raman-spectroscopie een aantrekkelijke techniek waarbij zeer geconcentreerde optische velden worden gebruikt om afzonderlijke EV's te immobiliseren, door middel van een optische val, en om tegelijkertijd een Raman signaal te genereren voor het identificeren van EVs op basis van biomoleculaire samenstelling. Lab-On-a-Chip (LOC) technologie maakt chip bouwstenen voor laser pincet Raman spectroscopie mogelijk in combinatie met microfluidische kanalen voor EV toevoer. Dit heeft de potentie om een compact en goedkoop apparaat te realiseren voor het identificeren van EVs en ziektediagnose.

Dit proefschrift behandelt de ontwikkeling van een LOC-bouwsteen voor een optische val waarin Raman-spectroscopie op enkelvoudige EV's bedreven kan worden. De bouwsteen bestaat uit meerdere optische golfgeleiders die eindigen op de zijwanden van een microfluidisch kanaal. De coherente, in tegengestelde richting voortplantende bundels, afkomstig van de golfgeleiders, interfereren in het kanaal en vormen een optisch interferentiepatroon samengesteld uit meerdere regio's van sterk geconcentreerd licht, elk geschikt voor optisch pincetwerking en Raman-spectroscopie.

Eerst wordt een gedetailleerd simulatiestudie behandeld die gericht is op het onderzoeken van de mogelijkheden en beperkingen van een twee-golfgeleider val voor stabiele optisch immobilisatie van EV's op de chip. De optische velden die in een microfluidisch kanaal worden gegenereerd, worden gesimuleerd met 3D electromagnetische veld-simulaties. De optische krachten op de EVs en de bijbehorende potentialen volgen uit de gesimuleerde velden. Toepassing van het criterium van Ashkin levert een uitgebreid overzicht op van omstandigheden voor een stabiele optische val voor EV's in termen van EV-diameter en brekingsindex, en het geïnjecteerde optische vermogen.

Vervolgens wordt ontwerp en fabricage van nieuwe multi-golfgeleider optische vallen beschreven. Deze ontwerpen zijn gericht op sterkere lichtopsluiting in het kanaal, wat leidt tot verbeterde optische pincetwerking en Raman-signaalgeneratie. Het gedrag van een val met twee golfgeleiders en 16 golfgeleiders wordt gekarakteriseerd met behulp van polystyreen bolletjes. De optische krachten worden gekwantificeerd door middel van valstijfheidswaarden die zowel uit experimenten als uit simulaties zijn verkregen. De twee vallen worden vergeleken door middel van de stijfheidswaarden en de gemeten Raman-signaalsterkte afkomstig van de bolletjes.

Ten slotte wordt de 16-golfgeleider val gebruikt om de eigenschappen van de optische pincetwerking op *B. subtilis* sporen te bestuderen, als tussenstap naar EV's. De optische krachten op de sporen worden bestudeerd met zowel experimenten als simulaties. Speciale aandacht is besteed aan het effect van willekeurige faseverschillen tussen de bundels afkomstig van de verschillende golfgeleiders op de kwaliteit van de optische val.



# 1

## Introduction

### 1.1. Extracellular vesicles as bio-markers for disease identification

Extracellular vesicles (EVs) are spherically shaped compartments with a phospholipid membrane, filled with fluid, lipids, RNA, and other biomolecules, and typically have diameters ranging from 30 nm to 1  $\mu\text{m}$  [1]. EVs originate from all cells, and are released into their environment including bodily fluids such as blood, saliva, and urine. EV concentration in these bodily fluids exceed  $10^{10}$  particles/ml with a variety of EVs that reflects the variety of cells from which they originate. EVs are excreted via the cell membrane and are employed by cells for various purposes, including but not limited to waste management, coagulation and inflammation, and intercellular communication. As a result, EVs carry physiological information of their parental cells [2]. In particular in case of disease, EV population in bodily fluids has been demonstrated to undergo changes through the increasing presence of disease related EVs, such as tumour derived EVs (tdEVs) [3]. Consequently, EVs have clinical relevance as biomarkers that can enable disease detection and diagnosis, and could be used for therapy development, as well as for monitoring therapy effectiveness [4, 5]. Application of EVs as biomarkers, however, requires characterization of the disease-associated EVs to distinguish their main physiochemical differences from health-associated EVs, which is challenging for a number of reasons. Firstly, a myriad of non-EV bioparticles such as protein aggregates and lipoproteins [6] are present in bodily fluids alongside the targeted EVs with similar sizes, even after sample purification. Secondly, the vast majority of EVs have a diameter between 30 nm to 200 nm which is below the detection range of conventional detection methods [7]. Thirdly, disease related EVs, such as tdEVs, are a minority of the total EV population, with concentrations roughly around  $10^4\text{mL}^{-1}$ , compared to the total EV concentration on the order of  $10^{10}\text{mL}^{-1}$  [8, 9]. The aforementioned application in disease detection and diagnosis and the associated challenges warrant development of novel technological platforms and methods to characterize single EVs. These techniques require the sensitivity and specificity to (i) discriminate between EVs and non-EV particles in a fluid medium, (ii) discriminate between the variety of EVs within the population to detect tdEVs (iii) to do so within reasonable times of a few hours at most.

### 1.2. Opto-fluidic lab-on-a-chip devices for single EV characterization

Among the methods to detect EVs, optical methods stand out as potential candidates for EV characterization on the level of single EVs [7]. Optical methods are mainly

based on elastic scattering, fluorescence or Raman spectroscopy, and have the main advantage of enabling non-invasive EV characterization within the sample medium, which ensures EV integrity and provides faithful representation of EV properties within native biological circumstances. Raman spectroscopy is particularly attractive, yielding biochemical information without needing to label the EVs [10, 11] with distinctive, optically detectable, markers. In addition, Raman spectroscopy combined with Rayleigh scattering during optical trapping has been demonstrated to make clear identification possible of tdEVs within a population of other EVs and non-EV particles [12]. Accumulation of enough single EV data, however, will lead to measurement times on the order of hours. Furthermore, single EV characterization requires targeted analysis with precise control of small sample volumes for supplying EVs to and from the detection volume. The above problems are currently being tackled within lab-on-a-chip (LOC) research.

LOC research aims for the miniaturization and integration of multiple laboratory processes on a single chip [13, 14]. Opto-fluidic LOCs combine micro-fluidics and integrated photonics technologies [15, 16] and are of particular interest for application to single EV characterization. In micro-fluidic technology fluidic networks on the scale of micrometers are designed and realized with specific functionalities including, but not limited to, single particle transport and analysis with precise control of small amounts of sample fluid. In addition, this technology enables on-chip multiplexing of single particle analysis by including multiple copies of the same building blocks, thus leading to an increase in throughput and thus reduction of total measurement time. Recent developments have demonstrated the feasibility of micro-fluidic chips with functionalities that include isolation, multi-disciplinary analysis and sorting for both cells [17, 18] and also for EVs [19].

Integrated photonics deals with the development of chips that contain waveguide circuitry for controlled transport and manipulation of light to realize and integrate on-chip sensing building blocks and functionalities, and miniaturize complex bulk optical systems. Recent developments in integrated photonics have demonstrated not only the capabilities in on-chip optical functionalities for single particle analysis but also single particle manipulation, and the near seamless compatibility of integrated photonics with microfluidics [20, 21].

In particular, silicon nitride ( $\text{Si}_3\text{Ni}_4$ ) and glass stand out as suitable integrated photonics platforms for the realization of opto-fluidic LOCs aimed at EV characterization. These platforms enable integrated photonics circuits operating at wavelengths in the visible and near-infrared that are typically used to avoid cell degradation, and by extension EV degradation, through photo-toxicity. In addition, these platforms are fully compatible with CMOS fabrication processes which makes mass-fabrication possible, thus ensuring opto-fluidic chips with reproducible performance, and which are also cost-effective. Speed-up of EV characterisation can then be achieved by employing multiple copies of the same opto-fluidic building blocks in parallel.

### 1.3. Raman scattering and spectroscopy

Scattering of light [22] occurs when monochromatic light with frequency  $\nu_0$  is incident on a medium that interacts with light of that frequency. Analysis of the spectral content of the scattered light will primarily yield light with the same frequency as the frequency

of the incident light  $\nu_0$ , also known as elastic (Rayleigh or Mie) scattered light. The spectral analysis will also yield light with a shifted frequency  $\nu'$ , known as inelastic or Raman scattered light. In case of Rayleigh/Mie scattering, light is elastically scattered because the energy of all scattered photons with respect to the incident photons is unchanged. On the other hand, for Raman scattering the photons are inelastically scattered as energy transfer takes place between the incident photons and molecular vibrations in the medium leading to a shift in energy of the scattered photons. This shift in photonic energy is expressed as:

$$h\nu' = h\nu_0 - h\Delta\nu \quad (1.1)$$

where  $h$  is Planck's constant. The Raman shift  $h\Delta\nu$  corresponds to a quantum of energy which is required for excitation of specific molecular vibrations and is observed as a frequency shift  $\Delta\nu = \nu' - \nu_0$  in the detected light. The Raman shift can leave Raman scattered photons with either larger or smaller energy than that of the incident photons [23, 24]. The scattering molecules start off in the ground state when Raman scattered photons end up having a lower energy. The Raman shift is then called a Stokes shift and leads to lower frequency (longer wavelength) of scattered light. In the opposite case, the scattering molecules start off in an excited state, and the Raman shift is called an anti-Stokes shift and the scattered light ends up with a higher frequency (shorter wavelength). Typically, the intensity of Stokes shifted Raman light, also known as spontaneous Raman scattering, is higher than the intensity of anti-Stokes shifted Raman light, as most of the molecules are in the ground state. The above examples of Raman scattering are schematically illustrated in the Jablonski diagrams of Figure 1.1a).

As  $\Delta\nu$  is molecule specific, biological media comprising a vast collection of complex molecular structures such as EVs, will yield a spectrum of Raman scattered photons which is a fingerprint of the biochemical composition. The Raman shift is typically quantified in terms of relative wavenumber,  $\sigma_{\text{rel}}$ , expressed in units of  $\text{cm}^{-1}$ . This can be expressed in terms of wavelength of incident light,  $\lambda_0$ , and Raman scattered light,  $\lambda'$ , as follows:

$$\sigma_{\text{rel}} = \frac{1}{\lambda_0} - \frac{1}{\lambda'} \quad (1.2)$$

with  $\lambda_0$  and  $\lambda'$  in cm. An example of a spontaneous Raman spectrum of polystyrene is shown in Figure 1.1b).

The Raman intensity,  $I_{\text{Raman}}$ , of each peak is proportional to the intensity of incident light,  $I_0$ , the Raman scattering cross-section,  $\sigma_{\text{Raman}}$ , and the number of molecules,  $N$ , that exhibit the same vibrational mode. Spontaneous Raman scattering, however, is inherently weak with roughly one Raman scattered photon occurring for every  $10^6$  scattered Rayleigh/Mie scattered photons. Hence, collection of enough Raman photons for a Raman spectrum with sufficiently high signal to noise ratio typically requires integration times of several seconds to a few minutes, and can then only be accomplished with a high-power laser. As a result, Raman spectroscopy of EVs requires strongly focused laser light, so that many photon-EV interactions can take place, thus maximizing the Raman output signal strength.

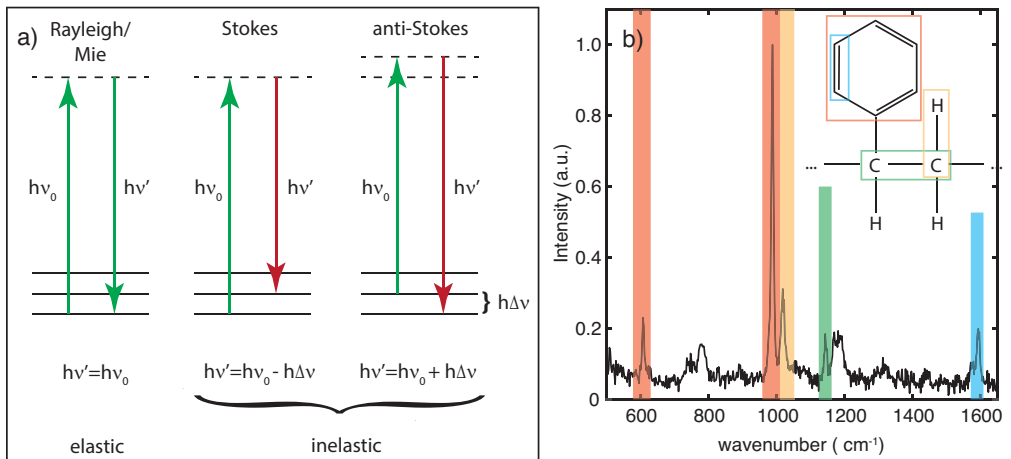


Figure 1.1: a) Jablonski diagrams illustrating photonic energy transfer in Rayleigh/Mie, Stokes Raman and anti-Stokes Raman processes. b) Spontaneous Raman spectrum of polystyrene along with the chemical structure of a polystyrene chain element. Characteristic polystyrene peaks are highlighted with various shades of color and corresponding molecular structures are annotated by boxes of the same color. Highlighted peaks include the ones at  $621 \text{ cm}^{-1}$  from the ring deformation mode, at  $1001 \text{ cm}^{-1}$  from the ring breathing mode, at  $1031 \text{ cm}^{-1}$  from C-H in-plane deformation mode, at  $1155 \text{ cm}^{-1}$  from the C-C stretch mode, and at  $1583 \text{ cm}^{-1}$  from the C=C stretch mode [25].

#### 1.4. Optical trapping

A surprising advantage of generating a Raman signal with focused light is that the narrow laser spot can also be exploited to confine the EV, as enough optical force is generated to stably hold or trap the EV in suspension. This so-called optical trapping is commonly associated with optical tweezers [26], in which an objective lens is used to tightly focus a laser beam to form an optical trap at the focal point. The high intensity of light at the focal point generates optical forces strong enough to confine micrometer and sub-micrometer particles in suspension. This was first reported by Ashkin who made an optical trap to manipulate micron-sized latex spheres in water [27], and was awarded the Nobel Prize in Physics in 2018 for this achievement. Since its discovery, optical trapping has strongly impacted several fields with applications ranging from particle manipulation to the study of single cells [28–30], and single bio-molecule mechanical properties [31].

The working principle of optical trapping can be described within three regimes, which are the Rayleigh, Mie and ray optics regime. The main criterion dividing these three regimes is the size of the particle,  $d_p$ , compared to the wavelength,  $\lambda$ . For the sake of simplicity, the trapped particle is considered to be a spherically shaped dielectric particle with refractive index,  $n_p$ , suspended in a medium with lower refractive index,  $n_m$ . In the ray optics regime  $d_p \gg \lambda$ , the interaction between particle and light is accurately described using geometric optics. The optical field is then described as a collection of rays, each of which carries a portion of the total optical power and linear momentum in proportion to the carried power. Upon reaching the particle surface, part of the light will be reflected, while the remainder will be refracted. The directions of propagation of the reflected and refracted rays differ from the direction of propagation of the incident ray, leading to a change in the overall momentum of the optical field. As

a consequence there will be a force on the particle, to conserve the momentum of the total system, comprising the optical field and the particle. This is shown schematically for an optical tweezer in figures 1.2 a) and b).

In the Rayleigh regime  $d_p \ll \lambda$ , the particle can be approximated as a point dipole [32] with a dipole moment,  $\vec{p}$ , expressed as:

$$\vec{p}(\mathbf{r}) = \alpha_e \vec{E}(\mathbf{r}) \quad (1.3)$$

where  $\mathbf{r}$  is the position of the dipole,  $\vec{E}$  the complex electric field amplitude at angular frequency  $\omega$  and  $\alpha_e$  the complex polarizability. The cycle averaged optical force in a linearly polarized optical field can be analytically expressed [33] as:

$$\vec{F} = \frac{\alpha'_e}{4} \langle \vec{\nabla} (|\vec{E}|^2) \rangle + \frac{2\pi\alpha''_e}{\lambda\epsilon_0 c} \langle \vec{S} \rangle \quad (1.4)$$

where  $\langle \dots \rangle$  denotes cycle averaging, with  $\vec{S}$  the Poynting vector,  $\alpha'_e$  and  $\alpha''_e$  the real and imaginary parts, respectively, of  $\alpha_e$ ,  $\epsilon_0$  the electric permittivity in vacuum, and  $c$  the vacuum speed of light. The first term in equation 1.4 is called the gradient force,  $\vec{F}_g$ , which is conservative in nature and describes a force that pushes the particle to regions of highly concentrated optical intensity,  $I = \epsilon_0 c \langle |\vec{E}|^2 \rangle$ . The second term is known as the scattering force,  $\vec{F}_k$ , and is proportional to the flow of power and linear momentum  $\langle \vec{S} \rangle$  along the local direction of light propagation, and to the scattering cross-section,  $\sigma_{\text{scatt}} = 2\pi\alpha''_e/\lambda\epsilon_0 c$ . The scattering force  $\vec{F}_k$  is non-conservative and takes into account the radiation pressure. It tends to push the particle along the main direction of propagation along the optical axis of the focused beam, out of the trap, thus competing with the stabilizing gradient force  $\vec{F}_g$ . For the optical tweezer to function well, the light must be sufficiently strongly focused to have  $|\vec{F}_g| > |\vec{F}_k|$ . Then the trapped particle is confined to a region around the mechanical equilibrium position on the optical axis, slightly displaced from the focal point. Optical trapping in the Rayleigh regime is schematically visualized in figure 1.2 c).

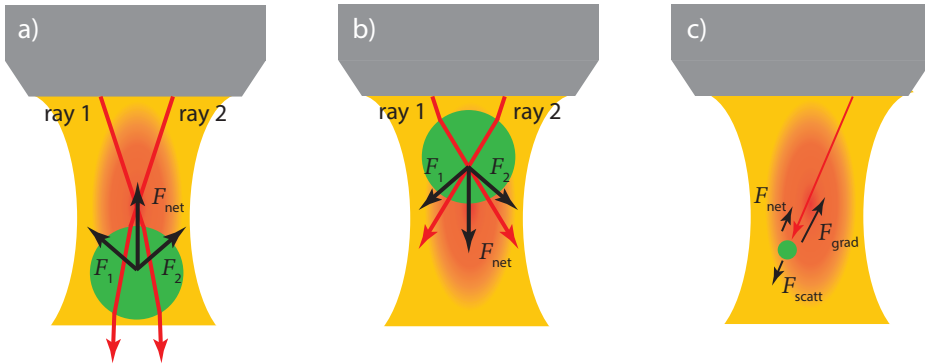


Figure 1.2: Schematic illustration of the ray optics view of optical trapping with the particle located a) below focus and b) above focus, and c) the Rayleigh view of optical trapping.

The above descriptions provide insight into general properties of optical trapping. Furthermore, equations 1.3 and 1.4 can also prove useful in a quantitative analysis of

optical trapping forces on EVs which have diameters,  $d_{\text{EV}}$ , falling within the Rayleigh regime. It appears, however, that EVs of size  $d_{\text{p}} \sim \lambda$  are of main interest, which point to intermediate Mie regime. Here a more rigorous approach is required, taking the full interaction between particle and optical field into account [35, 36]. In practice, numerical methods are required for computing the optical trapping forces in cases of more general field distributions and particle refractive index structures. One such method is the 3D finite-difference time-domain (FDTD) method, which is used to directly solve the Maxwell's equations and compute the electromagnetic vector fields on a 3D rectilinear grid, at equidistant points within a time interval [37].

The optical force is computed by integrating the so-called Maxwell stress tensor over a surface enclosing the particle:

$$F_{\alpha} = \oiint_S \sum_{\beta=x,y,z} \frac{1}{2} \text{Re}(T_{\alpha\beta} \hat{n}_{\beta}) dS \quad (1.5)$$

where  $\alpha = x, y, z$  indicate the Cartesian components,  $\hat{n}$  is the unit-vector normal to the surface  $S$ , and  $T_{\alpha\beta}$  the components of the Maxwell stress tensor, which can be expressed as:

$$T_{\alpha\beta} = D_{\alpha} E_{\beta}^* + H_{\alpha} B_{\beta}^* - \frac{1}{2} \delta_{\alpha\beta} (\vec{D} \cdot \vec{E}^* + \vec{H} \cdot \vec{B}^*) \quad (1.6)$$

Here  $\vec{B}$  is the magnetic field,  $\vec{D}$  and  $\vec{H}$  are the auxiliary electric and magnetic fields, respectively,  $\delta_{\alpha\beta}$  is the Kronecker delta, and the asterisk denotes complex conjugation. An advantage of using the Maxwell stress tensor to compute the optical force is that it requires relatively little computational resources, e.g. memory, as it only uses electromagnetic field data at the surface of the dielectric particle. This method, however, turns out inaccurate for small optical forces acting on EVs, with small  $d_{\text{EV}}$  and low refractive index contrast with suspending medium. In this case it has been shown that direct integration of the Lorentz force density over the volume of the particle is more accurate [38].

Experimentally, the optical forces of an optical trap are assessed by measuring the optical trap stiffness [39]. When displaced from the trap center, a trapped particle is subjected to a restoring force courtesy of the gradient force term in equation 1.4. For small displacements,  $x$ , from the trap center, the restoring force is linearly proportional to the displacement and is expressed as:

$$F_{\text{trap}} = -\kappa \cdot x \quad (1.7)$$

where  $\kappa$  is the trap stiffness. Here, we stick to a 1D description for the sake of simplicity. As a result, the trap potential is harmonic and thus expressed as:

$$U(x) = \frac{1}{2} \kappa (x - x_0)^2 \quad (1.8)$$

with  $x_0$  the trap center. According to the equipartition theorem [40], the time averaged thermal energy imparted to the trapped particle by the suspending medium as kinetic energy is  $k_{\text{B}}T/2$  in each direction of motion, with  $k_{\text{B}}$ , Boltzmann's constant and  $T$ , the absolute temperature. Consequently, an optically trapped particle experiences

confined Brownian motion and will explore the harmonic potential well to a degree depending on its thermal energy. The probability  $P(x)$  for a trapped particle to be found at position  $x$  in the trap is given by:

$$P(x) = \frac{1}{Z} \exp\left(-\frac{U(x)}{k_B T}\right) = \frac{1}{Z} \exp\left(-\frac{\kappa(x - x_0)^2}{2k_B T}\right) \quad (1.9)$$

with  $Z$  the partition function, as normalisation factor. The expression in equation 1.9 is a Gaussian function with variance  $\sigma^2 = k_B T / \kappa$ , leading to an expected value  $\langle U(x) \rangle = k_B T / 2$ , in agreement with the equipartition theorem. This implies that  $\kappa$  can be determined experimentally by fitting a Gaussian function to a measured histogram of trapped particle positions.

### 1.5. On-chip trapping and Raman spectroscopy

The focused laser beam trap is the foundation for development of novel on-chip optical trapping devices [21]. These devices are realized with integrated photonics structures designed to generate regions of highly confined optical fields leading to strong optical gradient forces to trap bio-particles for sensing. Two classes of on-chip traps have been realized, near-field traps and divergent field traps. Near-field traps generate a region of strongly concentrated light close to the device top surface, such as the localized resonant modes in photonic crystals [41]. Photonic crystal based traps employ strong gradient forces to trap and have been reported to optically trap bacteria [42, 43] and even nanoscopic bioparticles such as proteins [44]. The drawback of near-field traps is that optical trapping occurs in close proximity to surfaces which can lead to unwanted surface interactions that in turn can influence properties of the trapped particle. Additionally, when considering Raman spectroscopy, the proximity to the chip surface can also lead to unwanted background Raman signals.

These problems are not an issue in the case of divergent field traps which employ counter-propagating beams emitted by waveguides into a micro-fluidic environment. Coherent beams will interfere to form a standing wave with multiple hot spots of highly concentrated light. The main contribution to the optical force is again the gradient force as the scattering forces from the two opposing beams approximately cancel each other out, thus making the overall trapping force conservative [45]. In contrast to near-field traps, divergent beam traps permit optical trapping in suspension, away from the chip surface and thus closer to normal biological circumstances. These traps have been reported for use in combined on-chip optical trapping and Raman spectroscopy [46–48]. Of particular interest is the TripleX based dual-waveguide trap in ref. [48], which uses the same light sources for both optical trapping and Raman signal generation. TripleX is a  $\text{Si}_3\text{N}_4$  based waveguide technology in which alternating layers of  $\text{Si}_3\text{N}_4$  and silicon dioxide ( $\text{SiO}_2$ ) are used to realize waveguiding structures [49]. Besides yielding integrated photonic systems operating in wavelength ranges attractive for bio-sensing, TripleX is an established, CMOS-compatible platform allowing for mass fabrication. Hence, TripleX is chosen as the suitable material platform for the development of LOC systems for EV characterization with optical trapping and Raman spectroscopy.

## 1.6. Research goal and thesis outline

This thesis builds on the work presented by Boerkamp et al. [48], using the TripleX dual-waveguide trap as a starting point. The feasibility of on-chip optical trapping for EV-like particles, which are small in size and have low refractive index contrast with surrounding medium, is studied in-depth.

A novel multi-waveguide trap with more than two waveguides is designed, realized and tested with the aim to improve optical trapping capabilities compared to the dual-waveguide trap. The rationale for this development is to tailor the optical field distribution within the trap to enhance the optical field concentration within the trapping volume. This in turn will not only enhance the trapping forces but also the Raman yield from the trapped particle.

This thesis is centered around the main research question we address with the research presented in this thesis.

**Main research question:** *Is on chip optical trapping and Raman spectroscopy with multi-waveguide traps a viable technique for high throughput EV diagnosis?*

This is decomposed in the following subquestions:

**Question 1:** *What are the capabilities and limitations of the dual-waveguide trap for stable on-chip optical trapping of EVs?*

**Question 2:** *Can a micro-fabricated waveguide trap comprising more than 2 waveguides be realised with improved on-chip optical trapping and Raman signal generation compared with the dual-waveguide trap?*

**Question 3:** *Is on-chip optical trapping and Raman spectroscopy with a multi-waveguide trap feasible for (sub-)micron sized biological particles?*

The outline of the thesis is as follows. Chapter 2 deals with an in-depth simulation study regarding the optical trapping capabilities and limitations of the TripleX dual-waveguide trap presented in ref. [48]. The field distribution generated within traps of three different sizes are simulated with 3D FDTD simulations, and optical forces are computed for EVs according to two different refractive index models, the approximated homogenous sphere model and the more realistic core-shell model. The optical trapping results along with Ashkin's criterion for stable trapping [27] yield a detailed overview of the dual-waveguide trapping capabilities for EVs. This aim of this chapter is to answer question 1.

Chapter 3 presents the full development process of the novel multi-waveguide trap. This includes simulation studies, design considerations, fabrication process and performance evaluation. The optical trapping and Raman signal generation capabilities of a dual-waveguide trap and a multi-waveguide trap are compared using polystyrene beads of  $1\ \mu\text{m}$  and  $3\ \mu\text{m}$  in diameter. The aim of this chapter is to answer question 2.

In chapter 4, the multi-waveguide trap capabilities for optical trapping biological

particles is experimentally demonstrated on 1  $\mu\text{m}$  sized *Bacillus subtilis* spores. The quality of the optical trap is quantitatively studied with FDTD simulations and in experiment. Special attention is paid to the effects of waveguide phase errors on the optical field within the trap and thus the optical trapping forces. This chapter provides an indication of the multi-waveguide trap capabilities for optical trapping and Raman spectroscopy of EVs. The aim of this chapter is to answer question 3.

The findings of chapters 2 to 4 are gathered in chapter 5 to answer the main research question and draw general conclusions. Based on these conclusions, an outlook with suggestions for further research is proposed focused on development of on-chip EV characterisation techniques. This includes improvement of the on-chip Raman detection technique and alternative optical characterization techniques.

The appendices detail the computational and analytical methods used in this thesis to evaluate the multi-waveguide trap quality.

## References

- [1] E.R. Abels, X.O. Breakefield, "Introduction to extracellular vesicles: biogenesis, RNA cargo selection, content, release, and uptake", *Cellular and Molecular Neurobiology* 36(3), 301-312 (2016).
- [2] E. van der Pol, A.N. Böing, P. Harrison, A. Sturk, and R. Nieuwland, "Classification, functions, and clinical relevance of extracellular vesicles", *Pharmacological Reviews* 64(3), 676-705 (2012).
- [3] M. Verma, T.K. Lam, E. Hebert, and R.L. Divi, "Extracellular vesicles: potential applications in cancer diagnosis, prognosis, and epidemiology," *BMC Clinical Pathology* 15(6), 1-9 (2015).
- [4] A. Nanou, F.A.W. Coumans, G. van Dalum, L.L. Zeune, D. Dolling, et al., "Circulating tumor cells, tumor-derived extracellular vesicles and plasma cytokeratins in castration-resistant prostate cancer patients", *Oncotarget* 9(27), 19283 (2018).
- [5] Y. Meng, J. Sun, X. Wang, T. Hu, Y. Ma, et al., "Exosomes: A Promising Avenue for the Diagnosis of Breast Cancer", *Technology in cancer research & treatment* 18, 1533033818821421 (2019).
- [6] J.B. Simonsen, "What Are We Looking At? Extracellular Vesicles, Lipoproteins, or Both?", *Circulation Research* 121(8), 920–922 (2017).
- [7] E. van der Pol, A.G. Hoekstra, A. Sturk, C. Otto, T.G. van Leeuwen, et al., "Optical and non-optical methods for detection and characterization of microparticles and exosomes", *Journal of Thrombosis and Hemostasis* 8(12), 2596-2607 (2010).
- [8] L. Margolis, Y. Sadovsky, "The biology of extracellular vesicles: the known unknowns", *PLoS Biology* 17(7), e3000363 (2019).
- [9] K.B. Johnsen, J.M. Gudbergsson, T.L. Andresen, and J.B. Simonsen, "What is the blood concentration of extracellular vesicles? Implications for the use of extracellular vesicles as blood-borne biomarkers of cancer", *Biochimica et Biophysica Acta (BBA) - Reviews on Cancer* 1871(1), 109-116 (2019).

- [10] R.P. Carney, S. Hazari, M. Colquhoun, D. Tran, B. Hwang, et al., "Multispectral Optical Tweezers for Biochemical Fingerprinting of CD9-Positive Exosome Subpopulations", *Analytical Chemistry* 89 (10), 5357-5363 (2017).
- [11] W. Lee, A. Nanou, L. Rikkert, F.A.W. Coumans, C. Otto, et al., "Label-Free Prostate Cancer Detection by Characterization of Extracellular Vesicles Using Raman Spectroscopy", *Analytical Chemistry* 90 (19), 11290-11296 (2018).
- [12] A. Enciso-Martinez, E. van der Pol, A. T.M. Lenferink, L.W.M.M. Terstappen, T.G. van Leeuwen, et al., "Synchronized Rayleigh and Raman scattering for the characterization of single optically trapped extracellular vesicles", *Nanomedicine: Nanotechnology, Biology and Medicine* 24, 102109 (2020).
- [13] Á. Ríos, M. Zougagh, and M. Avila, "Miniaturization through lab-on-a-chip: Utopia or reality for routine laboratories? A review," *Analytica chimica acta* 740, 1-11 (2012).
- [14] S. Gupta, K. Ramesh, S. Ahmed, V. Kakkar, "Lab-on-chip technology: A review on design trends and future scope in biomedical applications," *International Journal of Bio-Science and Bio-Technology* 8, 311-322 (2016).
- [15] P. Paiè, T. Zandrini, R.M. Vázquez, R. Osellame, and F. Bragheri, "Particle manipulation by optical forces in microfluidic devices," *Micromachines* 9(5), 200 (2018).
- [16] H. Dawson, J. Elias, P. Etienne, and S. Calas-Etienne, "The Rise of the OM-LoC: Opto-Microfluidic Enabled Lab-on-Chip", *Micromachines* 12(12), 1467 (2021).
- [17] V. Lecault, A.K. White, A. Singhal, and C.L. Hansen, "Microfluidic single cell analysis: from promise to practice", *Current opinion in chemical biology*, 16(3-4), 381-390 (2012).
- [18] H. Tavakoli, W. Zhou, L. Ma, S. Perez, A. Ibarra, et al., "Recent advances in microfluidic platforms for single-cell analysis in cancer biology, diagnosis and therapy", *TrAC Trends in Analytical Chemistry* 117, 13-26 (2019).
- [19] C.M. Abreu, B. Costa-Silva, R.L. Reis, S.C. Kundu, and D. Caballero, "Microfluidic platforms for extracellular vesicle isolation, analysis and therapy in cancer", *Lab on a Chip* 22(6), 1093-1125 (2022).
- [20] R.J. Yang, F. Lung-Ming, and H.H. Hou, "Review and perspectives on microfluidic flow cytometers," *Sensors and Actuators B: Chemical* 266, 26-45 (2018).
- [21] J.E. Baker, R.P. Badman, and M.D. Wang, "Nanophotonic trapping: precise manipulation and measurement of biomolecular arrays", *Wiley Interdisciplinary Reviews: Nanomedicine and Nanobiotechnology* 10(1), e1477 (2018).
- [22] H.C. van de Hulst, "Light scattering by small particles," Courier Corporation, 1981.
- [23] D.A. Long, "Raman spectroscopy", New York, 1 (1977).
- [24] P. Larkin, "Infrared and Raman spectroscopy: principles and spectral interpretation," Elsevier, 2017.

- [25] M. Mazilu, A.C. De Luca, A. Riches, C.S. Herrington, and K. Dholakia, "Optimal algorithm for fluorescence suppression of modulated Raman spectroscopy," *Opt. Express* 18, 11382-11395 (2010).
- [26] A. Jonáš, and P. Zemanek, "Light at work: The use of optical forces for particle manipulation, sorting, and analysis. Electrophoresis," 29(24), 4813-4851 (2008).
- [27] A. Ashkin, J.M. Dziedzic, J. E. Bjorkholm, and S. Chu, "Observation of a single-beam gradient force optical trap for dielectric particles," *Optics Letters* 11(5), 288-290 (1986).
- [28] T. Avsievich, R. Zhu, A. Popov, A. Bykov, and I. Meglinski, "The advancement of blood cell research by optical tweezers", *Reviews in Physics* 5, 100043 (2020).
- [29] I.C.D. Lenton, E.K. Scott, H. Rubinsztein-Dunlop, and. I.A. Favre-Bulle, "Optical Tweezers Exploring Neuroscience", *Frontiers in Bioengineering and Biotechnology* 8, 602797 (2020).
- [30] H.M. Nussenzveig, "Cell membrane biophysics with optical tweezers", *European Biophysics Journal* 47, 499–514 (2018).
- [31] C.J. Bustamante, Y.R. Chemla, S. Liu, S. Liu, and M.D. Wang, "Optical tweezers in single-molecule biophysics", *Nature Reviews Methods Primers* 1(25), 1-29 (2021).
- [32] A. Yevick, D. J. Evans, and D.G. Grier, "Photokinetic analysis of the forces and torques exerted by optical tweezers carrying angular momentum", *Philosophical Transactions of the Royal Society A: Mathematical, Physical and Engineering Sciences*, 375(2087), 20150432 (2017).
- [33] S. Albaladejo, M.I. Marques, M. Laroche, and J.J. Saenz, "Scattering forces from the curl of the spin angular momentum of a light field", *Physical review letters* 103(11), 113602 (2009).
- [34] A. Zangwill, "Modern electrodynamics", Cambridge University Press, 2013.
- [35] P.A. Maia Neto, and H.M. Nussenzveig, "Theory of optical tweezers", *Europhys. Lett.* 50, 702-708 (2000).
- [36] A. Mazzoli, A. Maia Neto, and H.M. Nussenzveig, "Theory of trapping forces in optical tweezers", *P. Roy. Soc. Lond. A* 459, 3021-3041 (2003).
- [37] A. Taflove, A. Oskooi, and S.G. Johnson, "Advances in FDTD computational electrodynamics: photonics and nanotechnology", Artech House, 2013.
- [38] Lumerical FDTD Solutions, Inc., <https://support.lumerical.com/hc/en-us/articles/360042214594-Methodology-for-optical-force-calculations>.
- [39] G. Pesce, P.H. Jones, O.M. Maragò, and G. Volpe, "Optical tweezers: theory and practice", *The European Physical Journal Plus* 135(12), 1-38 (2020).
- [40] D.V. Schroeder, "An introduction to thermal physics," Addison Wesley Longman, 2000.

- [41] T. van Leest, J. Heldens, B. van der Gaag, and J. Caro, "Photonic crystal cavities for resonant evanescent field trapping of single bacteria", In *Biophotonics: Photonic Solutions for Better Health Care III SPIE 8427*, 147-157 (2012).
- [42] T. van Leest, J. Caro, "Cavity-enhanced optical trapping of bacteria using a silicon photonic crystal", *Lab Chip* 13(22), 4358–4365 (2013).
- [43] M. Tardif, J. B. Jager, P. R. Marcoux, K. Uchiyamada, E. Picard, et al., "Single-cell bacterium identification with a SOI optical microcavity", *Applied Physics Letters*, 109(13), 133510 (2016).
- [44] Y. Chen, X. Serey, R. Sarkar, P. Chen, and D. Erickson, "Controlled Photonic Manipulation of Proteins and Other Nanomaterials", *Nano Letters* 12 (3), 1633-1637 (2012).
- [45] J. Du, C. Yuen, X. Li, K. Ding, G. Du, et al., "Tailoring Optical Gradient Force and Optical Scattering and Absorption Force", *Scientific Reports*, 7(1), 1-7 (2017).
- [46] S. Dochow, M. Becker, R. Spittel, C. Beleites, S. Stanca, et al., "Raman-on-chip device and detection fibres with fibre Bragg grating for analysis of solutions and particles," *Lab Chip* 13(6), 1109–1113 (2013).
- [47] P. Løvhaugen, B.S. Ahluwalia, T.R. Huser, and O. G. Hellesø, "Serial Raman spectroscopy of particles trapped on a waveguide," *Opt. Express* 21(3), 2964–2970 (2013).
- [48] M. Boerkamp, T. van Leest, J. Heldens, A. Leinse, M. Hoekman, et al., "On-chip optical trapping and Raman spectroscopy using a TripleX dual-waveguide trap", *Optics Express* 22(25), 30528-30537 (2014).
- [49] K. Wörhoff, R.G. Heideman, A. Leinse, and M. Hoekman, "TriPleX: a versatile dielectric photonic platform", *Advanced Optical Technologies* 4(2), 189-207 (2015).

# 2

## On-chip optical trapping of extracellular vesicles using box-shaped composite $\text{SiO}_2$ - $\text{Si}_3\text{N}_4$ waveguides

*The application of on-chip optical trapping and Raman spectroscopy using a dual-waveguide trap has so far been limited to relatively big synthetic and biological particles, e.g. polystyrene beads and blood cells. Here, from simulations, we present the capabilities of dual-waveguide traps built from composite  $\text{SiO}_2$ - $\text{Si}_3\text{N}_4$  waveguides for optical trapping of extracellular vesicles (EVs). EVs, tiny cell-derived particles of size in the range 30-1000 nm, strongly attract attention as potential biomarkers for cancer. In general, EVs are hard to trap, because of their smallness and low index contrast w.r.t. water. This poses a challenge for a lab-on-a-chip device for trapping of EVs. From finite-difference time-domain simulations we obtain the narrow beam emitted from the waveguide facet into water, for a wavelength of 785 nm. For a pair of such beams, in a counter-propagating geometry and for facet separations of 5, 10 and 15  $\mu\text{m}$ , we derive the inter-facet optical field, which has a characteristic interference pattern with hot spots for trapping, and calculate the optical force exerted on EVs of size in the range 50-1000 nm, as a function of EV position. In this procedure two refractive index models represent the EV optical properties. Integration of the force curves leads to the trapping potentials, which are well-shaped in the transverse and oscillatory in the longitudinal direction. By applying Ashkin's criterion, the conditions for stable trapping in the traps are established, the central result of this work. Very small EVs can be stably trapped with the dual-waveguide traps by applying a power also suitable for Raman spectroscopy, down to a smallest EV diameter of 115 nm. Based on this, we argue, this dual-waveguide trap is a promising lab-on-a-chip device with clinical relevance for diagnosis of cancer.*

---

As published in: G.B. Loozen, J. Caro, "On-chip optical trapping of extracellular vesicles using box-shaped composite  $\text{SiO}_2$ - $\text{Si}_3\text{N}_4$  waveguides," *Optics Express* **26**, 21 (2018).

## 2.1. Introduction

A class of lab-on-a-chip devices for optical analysis of particles is based on using integrated photonic waveguides for manipulating and spectroscopic fingerprinting the particles, with the goal of their identification. Possible application fields are various, and include point-of-care diagnostics and drinking water technology [1], with a focus on, for example, detection of human cells indicative of a disease and harmful bacteria. Examples in this field are labs-on-a-chip for optical trapping and Raman spectroscopy. These are on-chip versions of a laser-tweezers Raman spectroscopy (LTRS) setup [2]. LTRS unifies particle trapping with a focused laser beam and Raman spectroscopy of the trapped particle using the same concentrated light. This leads to Raman identification of the trapped particle. Prominent examples of on-chip versions are dual-fibre or dual-waveguide traps, often combined with microfluidics for particle supply. These traps are based on two opposing fibres or integrated photonics waveguides, from which counter-propagating beams emanate that define the concentrated optical field for trapping and Raman spectroscopy.

The dual-fibre trap in [3] has been used to hold and manoeuvre human cells to record their Raman signals. The trap in [4], apart from fibres for trapping and Raman generation, has fibers for collecting Raman signals. A preference is arising towards dual-waveguide devices based on microfabricated waveguides, thus avoiding delicate mounting of fibres and aiming for mass production. An important step in this direction is reported in [5, 6], where the waveguides are created by local modification of the index of glass using accurate writing with a femtosecond laser beam. The resulting devices can successfully trap and stretch red blood cells (RBCs). The laser-writing technique is inherently sequential, making it particularly suitable for fast prototyping. We further mention the traps reported in [7, 8], based on microfabricated  $\text{Ta}_2\text{O}_5$  waveguides. In [7] trapping of synthetic particles and RBCs is demonstrated, with supply of particles to the trap by optical propulsion on the waveguides. In [8] Raman spectra of trapped synthetic spheres are reported, but the spectra are induced using a separate laser beam and not by the beams emitted by the waveguides. In our work [9], we have exploited the counter-propagating beams in a dual-waveguide trap built from special waveguides microfabricated with semiconductor processing techniques to their full capability, using the beams both for trapping synthetic particles and for inducing Raman signals from the trapped particles.

Recently, LTRS has been applied for studying human extracellular vesicles (EVs) [10–12]. These cell-derived particles are present in bodily fluids such as urine and have a diameter ranging from 30 to 1000 nm, the size-distribution's maximum occurring below 200 nm. An EV comprises a lipid-bilayer membrane of the parental cell, enclosing mainly cell-derived cytoplasm with suspended DNA, RNA and proteins. Tumor-derived EVs strongly attract attention as potential biomarkers for cancer [13, 14]. For cancer diagnosis such EVs may play a role similar to that of circulating tumor cells (CTCs [15]). The bio-chemical composition of a fraction of EVs may already deviate from regular in a very early stage of carcinogenesis of the organ from which the EVs derive [16], while presence of CTCs indicates full existence of organ cancer. Thus, determining EV composition using LTRS can lead to early cancer diagnosis [17]. However, only a small sub-population of EVs in bodily fluids shows a signature of carcinogenesis, if present. This circumstance asks for high throughput platforms, e.g. lab-on-a-chip

devices scaled to versions with multiple parallelism [18]. Further, EVs are very small and have a low index contrast w.r.t. the suspending medium, making on-chip optical trapping of EVs challenging.

Here, from a simulation study, we present the capabilities for trapping of EVs of the dual-waveguide trap we apply in [9]. The novelty compared to [9] is that we here simulate for this type of trap the full range of optical and trapping properties, leading to qualification for the characterization of EVs. Further, our simulation results provide guidance for design and development of dual-waveguide devices for optical trapping and Raman spectroscopy of a broad range of bio-particles relevant for health and medicine.

## 2.2. Device geometry and optical models for EVs

The building block of the dual-waveguide trap is a waveguide with a box-shaped composite  $\text{Si}_3\text{N}_4 - \text{SiO}_2$  structure. Its cross section of  $1 \times 1 \mu\text{m}^2$  is shown in figure 2.1 (a). The walls of the square box are 50 nm thick  $\text{Si}_3\text{N}_4$  layers. The material inside and outside the box is  $\text{SiO}_2$ . With this structure we model the slightly trapezoidal TripleX [20, 21] waveguides we apply for the dual-waveguide trap in [9].

The geometry of the dual-waveguide trap built from a pair of such waveguides is depicted in figure 2.1 (b). The waveguides are opposed and guide light to a fluidic channel, used for supply of EVs. The waveguide facets, which emit a narrow light beam, are part of the walls of the fluidic channel. The counter-propagating beams created in this way define a strongly confined optical field and thus form an optical trap. The gap width  $w$  between the waveguide facets is 5, 10 or 15  $\mu\text{m}$ , equal to the widths in the devices leading to the results in [9]. The trap centre is the origin of the coordinate-system (see figure 2.1 (b)). The  $x$ -direction is the longitudinal direction and the  $y$ - and  $z$ -directions are the transverse directions.

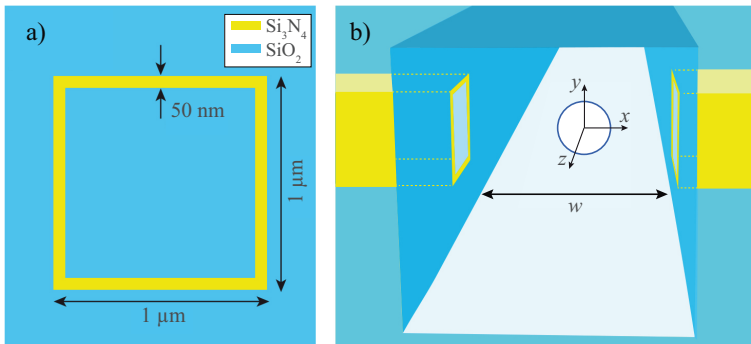


Figure 2.1: (a) Cross section of the composite  $\text{SiO}_2 - \text{Si}_3\text{N}_4$  waveguide, the building block of the dual-waveguide trap. The material inside and outside the square box with  $\text{Si}_3\text{N}_4$  walls is  $\text{SiO}_2$ . (b) Three-dimensional impression of the dual-waveguide trap. The waveguide facets, with separation  $w$ , are part of the walls of the fluidic channel. The origin of the coordinate system is the trap centre, where in the figure an EV is located with a core-shell structure.

EVs are spherical particles [22], with a diameter  $d_{EV}$ . We represent their optical properties by two models for the refractive index  $n$ . The first model assumes a homogeneous EV index, for which we take  $n_{hom} = 1.37$  [23]. In the second model we apply the realistic core-shell structure of EVs, using  $n_{core} = 1.37$  and  $n_{shell} = 1.46$  [24], and taking a shell thickness of 5 nm. The homogeneous index can be accurate enough for big vesicles since these have a small surface-to-volume ratio. The core-shell model will be more appropriate for small vesicles since for these the shell contribution to the total optical force is expected to be rather high.

### 2.3. Simulation approach

We derive the electromagnetic fields in the traps with the 3D finite-difference time-domain (FDTD) method, using Lumerical FDTD solutions [25]. The first goal is to obtain the optical forces acting on an EV, as a function of its position on the three axes defined in figure 2.1 (b), and for the 10 or 15  $\mu\text{m}$  traps on other axes parallel to the  $y$ -axis. This is done by simulating traps containing an EV and empty traps. The fields with the EV in the trap are needed for Lumerical's force calculations. The fields for the empty trap are used to independently calculate the forces for comparison with Lumerical's method, as discussed below. The TE mode obtained from Lumerical's mode solver is excited in each waveguide, for wavelength  $\lambda_0 = 785\text{nm}$ . This is our preferential wavelength [9], in view of generating Raman signals from the trapped particle. We use planar sources, placed at 2  $\mu\text{m}$  from the waveguide facet, that oscillate in phase and emit a short Gaussian pulse of carrier frequency  $f = c/\lambda_0$ , the frequency corresponding to the mode's wavelength. The time traces of the electromagnetic fields at each mesh point are Fourier transformed to obtain the spatial dependence of the complex amplitudes of the harmonic fields for  $\lambda_0$ . This procedure yields the beams emitted from the facets, which according to the TE polarization have  $\vec{E}/\hat{z}$ .

The mesh size must be small enough to resolve the fields, on the scale of i) the wavelength in the highest index material, ii) the smallest structure of the device and iii) the details of the EV structure. The simulation time, however, is inversely proportional to the mesh size to the fourth power, implying a practical limit. To fulfill the mesh-size requirements, while keeping simulation time within reasonable bounds, we subdivide the total simulation domain into three subdomains of different mesh size. The total simulation domain is 17 and 11  $\mu\text{m}$  in the  $y$ - and  $z$ -direction, respectively. The length in the  $y$ -direction exceeds that in the  $x$ -direction for the TE polarization used, in view of the side lobes emitted away from the beam axis (see Section 2.4). In the  $x$ -direction the simulation domain is  $5.4+w$   $\mu\text{m}$ . At the domain's boundaries we use 2  $\mu\text{m}$  thick perfectly matched absorbing layers.

The first subdomain is a rectangular block of cross section  $2 \times 2$   $\mu\text{m}^2$ , enclosing the waveguides. It has mesh size  $\Delta_1 = 10$  nm, imposed by the Si<sub>3</sub>N<sub>4</sub> waveguide walls. The block length equals the total domain's length in the  $x$ -direction. The second subdomain is a cube of edge  $d_{EV} + 10\Delta_2$  surrounding the EV. For the homogeneous index model, we choose  $\Delta_2 = d_{EV}/20$ , with an upper limit of 10 nm. For the core-shell model we take  $\Delta_2 = 2$  nm, in view of the thin EV shell. The third subdomain is the remainder of the total domain, for which we take  $\Delta_3 = \lambda_0/(14n_{\text{SiO}_2})$ . In simulating the empty trap, we use  $\Delta_4 = 10$  nm in the first and second subdomain and  $\Delta_3 = \lambda_0/(14n_{\text{SiO}_2})$  in the third subdomain.

We obtain the time-averaged force  $\vec{F}$  acting on an EV using Lumerical's volumetric technique, by calculating the volume integral of the time-averaged Lorentz force density for a cube enclosing the EV. The edge of the integration cube is  $d_{EV} + 7\Delta_2$ , some smaller than the cube's edge that defines the sub-meshing. The Lorentz force density  $\langle \vec{f} \rangle$  is calculated at each mesh point inside the cube and on its faces using:

$$\langle \vec{f} \rangle = \epsilon_0 \epsilon_b (\vec{\nabla} \cdot \langle \vec{E} \rangle) \langle \vec{E} \rangle + i\omega \epsilon_0 (\epsilon_{EV} - \epsilon_b) \langle \vec{E} \rangle \times \langle \vec{B} \rangle \quad (2.1)$$

Here  $\vec{E}$  and  $\vec{B}$  are the position dependent time-averaged electric and magnetic field, respectively, with the EV in the trap.  $\epsilon_0$  is the vacuum permittivity, while  $\epsilon_b$  and  $\epsilon_{EV}$  are the relative permittivity of the background medium (i.e. water) and the EV, respectively, the latter being a function of position for the core-shell model. We assume lossless materials, implying that the relative permittivities equal the square of the refractive indices.  $\omega = 2\pi c/785 \text{ nm}$  is the angular frequency of the light. The force on the background medium in the integration cube does not contribute to the net force on the EV. Based on the symmetry of the device geometry, we limit the force calculations to the three half-axes of the first octant, which gives all relevant information on the force behavior in the complete three-dimensional system. For a simulation of a single force point, i.e. for a single EV position, we used five so-called thin nodes of a supercomputer, each having 24 cores operating at 2.4 or 2.6 GHz, and 64 GB of RAM. On average such a single point simulation takes 10 minutes.

To calculate the forces for the smaller EVs with an independent approach, enabling comparison with Lumerical's method applied to EVs with an assumed homogenous index, we use the expression for the so-called time-averaged gradient force acting on a homogeneous dielectric particle, here an EV [26]:

$$\langle \vec{F} \rangle = \frac{\pi \epsilon_0 \epsilon_b d_{EV}^3}{8} \left( \frac{m^2 - 1}{m^2 + 2} \right) \langle \vec{\nabla} |\vec{E}|^2 \rangle, m = \epsilon_{EV} / \epsilon_0 \quad (2.2)$$

Here  $\langle \dots \rangle$  again denotes time-averaging, while in this case  $\vec{E}$  is the electric field in the empty trap. Equation 2.2 is valid for a dielectric particle small enough for the electric field to be virtually constant throughout its volume. For such particles the gradient force accurately represents the full optical force of a trap provided the scattering force is negligible or zero. This situation is known to occur in and close to the centre of free space traps with counter-propagating beams of equal intensity [27, 28].

The gradient force of Eq. 2.2 inherently is a conservative force. Consequently, in the approximation of negligible scattering force, a unique value of the trapping potential can be assigned at any point by integrating the force along a suitable path. We anticipate that the forces of the dual-waveguide trap obtained with the volumetric technique are rather close to the gradient force and thus can be considered as conservative. Therefore, we derive the position dependent optical potential by integrating the force obtained with the volumetric technique. For example, the transverse potential  $U_y(x_0, y_0, 0)$  in the point  $y_0$  for an axis parallel to the  $y$ -direction through the point  $(x_0, z = 0)$  ( $(x_0, y_0 \geq 0)$  the negative branches follow from symmetry) is given by:

$$U_y(x_0, y_0, 0) = - \int_{-\infty}^{y_0} \langle F_{x_0, y, 0}(y) \rangle dy \quad (2.3)$$

In Eq. 2.3  $x_0$  ( $x_0 \geq 0$ ) is the position of the minimum of the global potential for the  $x$ -direction (see Section 2.7). For the 5  $\mu\text{m}$  trap a single minimum occurs at  $x_0 = 0$ . For the 10 and 15  $\mu\text{m}$  traps,  $x_0$  is the position of one of the minima of the (symmetric) double-well potential, which is located near the facet (see Section 2.7). Loosely, the potential given by Eq. 2.3 will further be called  $U_y$ . For  $U_z$  an equation similar to Eq. 2.3 holds. For the  $x$ -direction  $F_x$  is only defined between the waveguide facets. Therefore, to calculate the longitudinal potential  $U_x(x_0)$  we limit the integration interval such that the EV is not in contact with the facet. This leads to:

$$U_x(x_0) \equiv U(x_0, 0, 0) = - \int_{x_1}^{x_0} \langle F_x(x) \rangle dx \quad (2.4)$$

Here, we choose  $x_1 = (w + d_{\text{EV}})/2 - 3\Delta_2$ . We add a constant to the outcome of Eq. 2.4, such that  $U_x(0) = U_y(0)$ .

Calculating the potential for three axes, yields the main information on the potential wells. For stable trapping of an EV the potential well should be deep enough. For this we use Ashkin's stability criterion, according to which trapping in a potential well of depth  $U_0$  is stable for  $U_0/kT \geq 10$  [19]. Since the well depth is proportional to the optical power supplied to the trap by the waveguides, the criterion leads to a condition for the optical power.

## 2.4. Waveguide mode, emitted beam, and energy density in the trap

We have calculated the TE mode of the waveguide of figure 2.2 (a) using Lumerical's mode solver for  $\lambda = 785\text{nm}$ . At this wavelength the waveguide supports a single mode per polarization. We use refractive indices of 2.00, 1.45 and 1.33 for Si<sub>3</sub>N<sub>4</sub>, SiO<sub>2</sub> and water, respectively. The mode profile is shown in figure 2.2 (a), where the colors represent the intensity of the light. As can be seen, for this polarization the electric field concentrates in the upper and lower Si<sub>3</sub>N<sub>4</sub> walls of the box. Further, the field is relatively low in the interior of the box (SiO<sub>2</sub>), quite contrary to the case of usual homogeneous ridge waveguides. The electric field drops abruptly upon entering the vertical walls of the box from inside or outside, satisfying the boundary condition for the normal component for the dielectric displacement.

FDTD simulation leads to the energy-density distribution in the  $xy$ -plane in figure 2.2 (b), both in the waveguide and the water, using a source in the waveguide emitting 1 W of power towards the facet. At the facet the guided mode is converted into radiation modes that enter the water present for  $x \geq 0$ . The oscillatory pattern inside the waveguide and its walls represents a standing wave resulting from interference of the forward propagating mode and its part reflected back from the facet. Near the facet, the radiation modes take the form of two coherent beamlets emitted by the upper and lower waveguide walls. These beamlets merge, yielding a main beam (further called beam) coaxial with the waveguide axis, which co-exists with two side lobes directed away from the axis. The beam reaches its energy-density maximum on the axis at 1.2  $\mu\text{m}$  from the facet, whereafter it decays smoothly and simultaneously broadens. The maximum and the decay of the beam are quantified by the longitudinal energy-density profile plotted in figure 2.2 (c). The transverse beam profiles in figure 2.2 (d) further quantify the beam, in particular its spreading with increasing

distance to the facet. The transverse profiles show shoulders at distances of 1.2 and 2.5  $\mu\text{m}$  that arise from the aforementioned side lobes. We have compared the beam in figure 2.2 (c) with the one we report in [29] for a  $\text{Si}_3\text{N}_4$  solid core waveguide of the same cross section. We find that the decay length of the present beam is about three times longer and the beam spreading correspondingly weaker, meaning that the composite  $\text{Si}_3\text{N}_4 - \text{SiO}_2$  waveguide produces a tighter beam and thus is a better waveguide to build a strong optical trap.

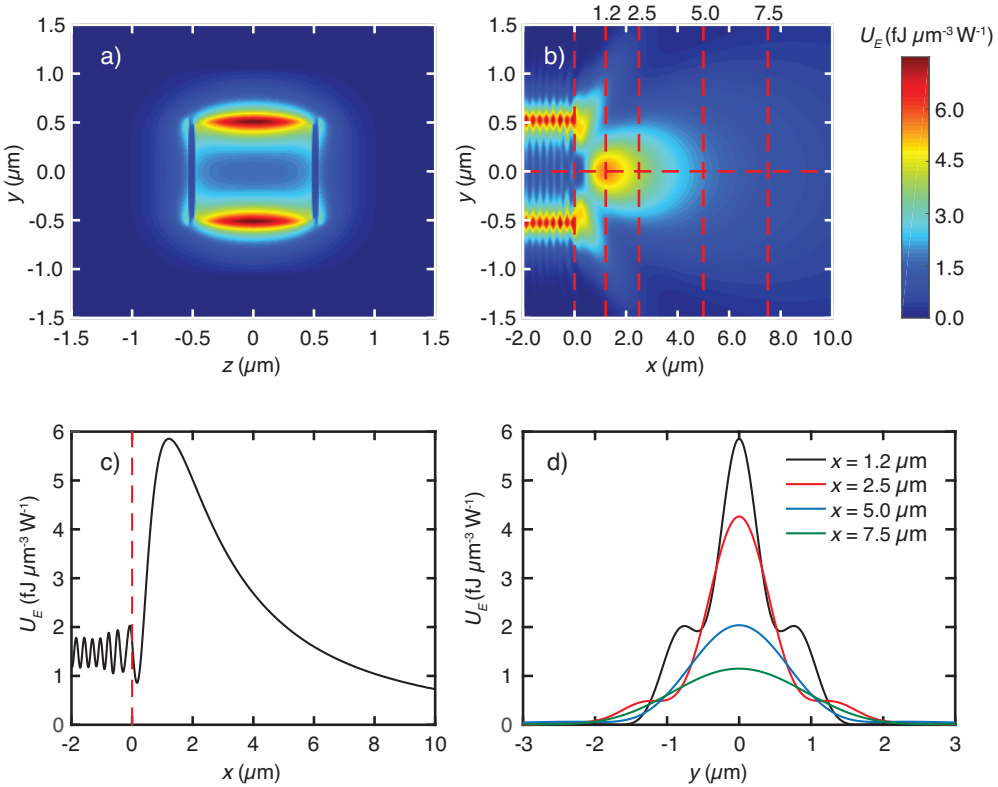


Figure 2.2: (a) Profile of the TE mode of the waveguide in figure 2.1 (a), for a wavelength of 785 nm. The colors indicate intensity, red (blue) meaning high (low), and do not relate to the scale bar to the right. (b) Energy density of the optical field in the  $xy$ -plane, both in the waveguide and the water, obtained from a FDTD simulation. The horizontal dashed line is the beam axis. Vertical dashed lines indicate the facet position and are the transverse lines for which in (d) beam profiles are plotted. The color bar defines the energy-density values. (c) Longitudinal energy-density profile on the beam axis. (d) Transverse beam profiles on the axes in (b).

For three traps built from the waveguide of figure 2.1 (a) with facet separations of 5, 10 and 15  $\mu\text{m}$  we have simulated the optical fields resulting from the coherent counter-propagating beams. In figure 2.3 we show time averaged energy-density distributions in  $xy$ -plane of the traps. A total power of 1 W is supplied to the traps, each waveguides contributing 0.5 W. We omit the distribution in the  $xz$ -plane, since it portrays the same type of behavior.

A common characteristic of the traps is the interference pattern between the facets, which has a period of 306 nm. The EV size distribution is such that a small EV can be locally trapped at a single maximum of the interference pattern, here further called hot spot. But also multiple small EVs may be trapped at one hot spot, similar to trapping of multiple EVs with a laser trap [10]. A hot spot is narrower in the longitudinal than in a transverse direction. Therefore, the confined Brownian motion of an EV has wider excursions in a transverse than in the longitudinal direction.

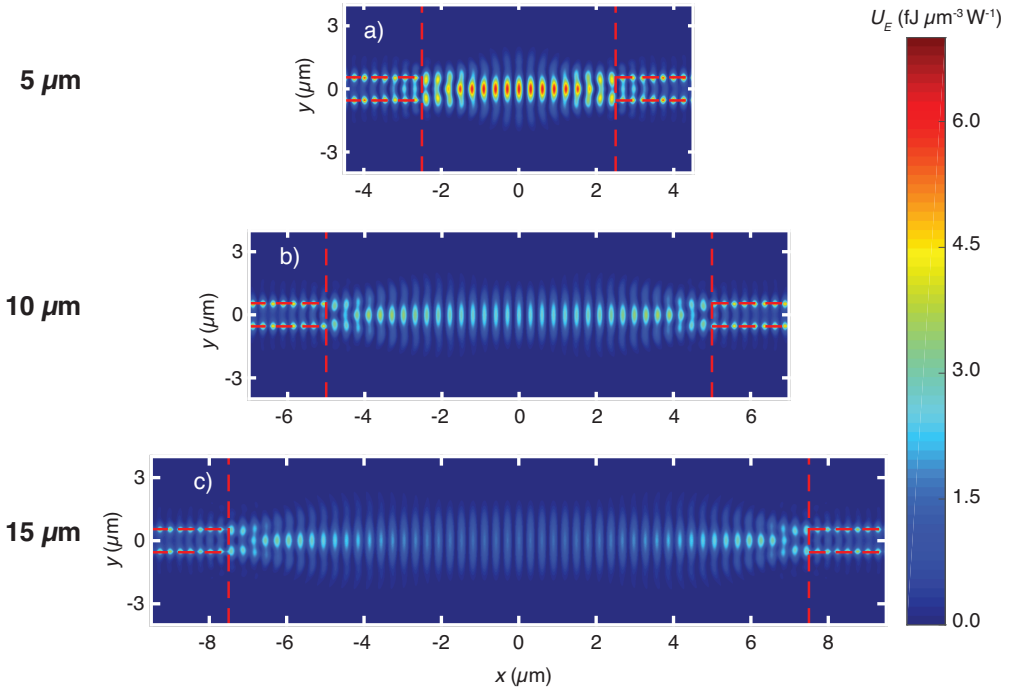


Figure 2.3: Time averaged energy density in the  $x$ - $y$ -plane for dual-waveguide traps with a facet separation of 5, 10 and 15  $\mu\text{m}$ . The total power supplied to each trap is 1 W. The 5  $\mu\text{m}$  trap has one global hot region centred between the facets. The 10 and 15  $\mu\text{m}$  traps have two global hot regions, each near a facets. The color bar defines the energy-density values.

The three traps, however, also show an important difference concerning the position of the regions where the interference maxima are strongest, i.e. the so-called global hot regions. For the 5  $\mu\text{m}$  trap a single global hot region exists (see figure 2.3), symmetrically placed around the center. The 10 and 15  $\mu\text{m}$  traps, on the contrary, have two global hot regions near the facets. This difference results from the longitudinal profile of the interfering beams shown in figure 2.2 (c), in particular their decay and the position of their maximum. These are such that the central global hot region of the 5  $\mu\text{m}$  gap is split into two global hot regions for the wider gaps. We note that the trap built from  $\text{Si}_3\text{N}_4$  solid core waveguides [29] already shows two global hot regions for facets 5  $\mu\text{m}$  apart. This agrees with the weaker beam decay in the present traps.

## 2.5. Force characteristics of the traps

We have calculated the longitudinal force curve  $F_x(x)$  and the transverse force curves  $F_y(y)$  and  $F_z(z)$  in the traps. For up to about two dozen diameters of homogeneous EVs in the range 50–1000 nm and for 6 diameters of core-shell EVs in the range 50–450 nm such curves have been obtained, of which a fraction is shown in figure 2.4. Forces acting on homogeneous EV have also been calculated using Eq. (2.2), giving the gradient force. Gradient-force data are included in figure 2.4 (a), 2.4(b) and 2.4(c) for  $d_{EV} = 100$  nm (black dots), but such data have been obtained for other diameters as well. We concentrate on the 5 and 15  $\mu\text{m}$  traps, since qualitatively results for the 10  $\mu\text{m}$  trap are very similar to those of the 15  $\mu\text{m}$  trap.

In Figs. 2.4(a), 2.4(b) and 2.4(c) curves  $F_y(y)$ ,  $F_z(z)$ , and  $F_x(x)$  for the 5  $\mu\text{m}$  trap are shown, respectively, for diameters as indicated and in figure 2.4 (a) and 2.4(b) for both index models. The unit of force is pN/W, i.e. the force is normalized to the power delivered to the trap. In figure 2.4 (d)  $F_x(x)$  is shown for the 15  $\mu\text{m}$  trap, restricted to homogeneous EVs of the same diameters as in the other sub-figures.

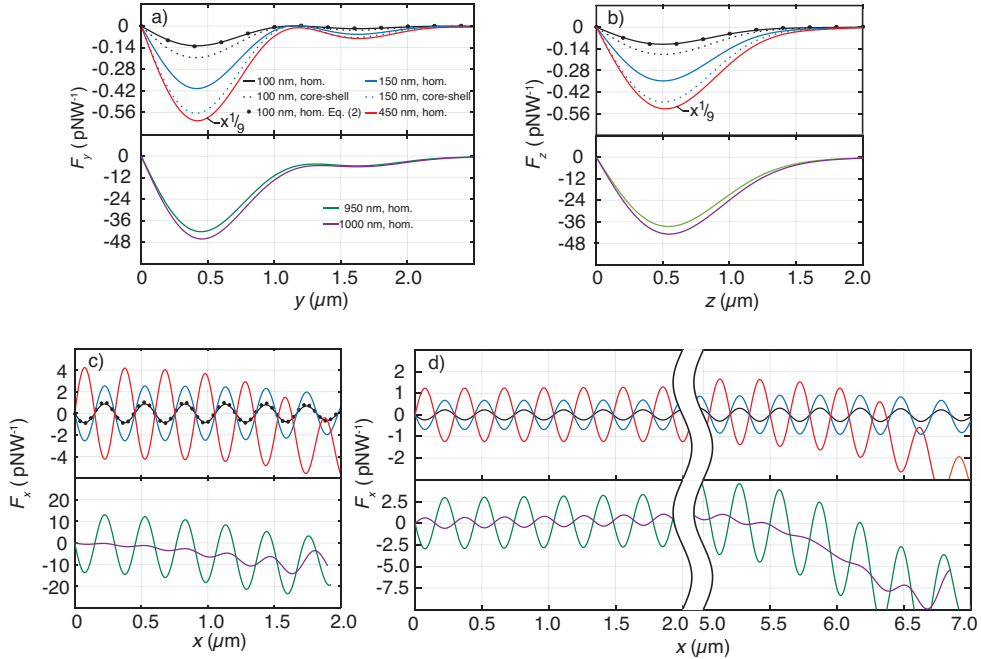


Figure 2.4: Force curves for the 5 and 15  $\mu\text{m}$  traps, calculated using the volumetric technique. The black dots have been obtained using Eq. (2.2). The legends in (a) define EV size and EV index model (homogeneous vs. core-shell) and apply to each panel. (a) Transverse force  $F_y(y)$  for the 5  $\mu\text{m}$  trap. (b) Transverse force  $F_z(z)$  for the 5  $\mu\text{m}$  trap. (c) Longitudinal force  $F_x(x)$  for the 5  $\mu\text{m}$  trap. (d) Longitudinal force  $F_x(x)$  for the 15  $\mu\text{m}$  trap, with part of the x-axis omitted to obtain the same horizontal scale as in (a-c). The curves in (a-d) are piecewise cubic spline interpolations between the data points.  $F_y(y)$  and  $F_z(z)$  curves have 15 data points.  $F_x(x)$  curves have 33 data points per  $\mu\text{m}$ .

In view of symmetry, the plots are limited to the positive half axes. Transverse force curves for the 15  $\mu\text{m}$  trap are omitted, since qualitatively these are similar to

those of the 5  $\mu\text{m}$  trap in figure 2.4 (a). In condensed form, the properties of the three traps are quantitatively reflected by trap stiffnesses in table 2.1 below and by stability curves in section 2.7.

$F_y(y)$  for the 5  $\mu\text{m}$  trap is linear near the origin and has a negative slope. This reflects the restoring character of a Hookean force pulling back the EV to the hot spot at the origin, a behavior described by  $F_y(y) = \kappa_y y$ , with  $\kappa_y$  the normalized stiffness for the  $y$ -direction. Normalized stiffnesses for the other directions are defined accordingly. With increasing distance  $|F_y(y)|$  reaches an absolute maximum, followed by a local maximum. The absolute maximum relates to the maximum gradient of the beam in figure 2.2 (b). The local maximum relates to the side lobes in that figure. For  $d_{\text{EV}} = 1000$  nm, the local maximum is less pronounced, since the EV for this size overlaps with both the beam and the side lobe, making their individual contributions less distinct. This behavior of  $F_y(y)$  applies to both index models, but for small diameters the force on core-shell EVs (curves shown for  $d_{\text{EV}} = 100, 150$  nm) is considerably higher than that for homogeneous EVs. For  $d_{\text{EV}} = 50$  nm,  $F_y$  on average is 110 % higher for the core-shell EV than for the homogeneous EV, while for  $d_{\text{EV}} = 250$  nm the percentage still is 25%. For  $d_{\text{EV}} = 500$  nm the forces for the two models are virtually the same. Apparently, for the smaller diameters the shell, though only 5 nm thick, contributes significantly to the force and thus cannot be omitted in the EV model.

As can be seen in figure 2.4 (b),  $F_z(z)$  behaves very much the same as  $F_y(y)$ , the differences being that  $|F_z(z)|$  is some smaller than  $|F_y(y)|$ , accompanied by a slightly less steep initial slope, that the maximum of  $|F_z(z)|$  occurs at a slightly larger distance and that a local minimum of  $|F_z(z)|$  is absent. These differences can be traced back to a less tight beam in the  $xz$ -plane and absence of side lobes in that plane.  $F_y(y)$  and  $F_z(z)$  being so close, we will further refer to  $F_y(y)$  as the transverse force.

$F_x(x)$  is an oscillatory function, as exemplified in Figs. 2.4(b) and 2.4(c) for the 5 and 15  $\mu\text{m}$  traps. The oscillation period equals the period of the fields in figure 2.3, implying that the origin is interference. As a function of EV size, a hot spot of the interference pattern attracts or repels the EV, depending on whether the local force-curve slope is negative or a positive. In Figs. 2.4(b) and 2.4(c) attraction occurs for 100, 150 and 950 nm, while repulsion occurs for 450 and 1000 nm. This sign reversal of the force agrees with [30], which reports that the sign in a standing wave trap depends periodically on particle size and that the particle's equilibrium position alternates between interference maxima and minima. Further [30], particle sizes exceeding the interference-pattern period exist for which the net optical force is zero as a result of complete cancellation of attractive forces of neighbouring hot spots. For the 1000 nm EV this cancellation almost occurs, giving weak oscillations in Figs. 2.4(b) and 2.4(c). EVs clearly smaller than the interference-pattern period are attracted by only a single hot spot, giving an amplitude of  $F_x(x)$  considerably higher than the maximum of  $|F_y(y)|$ . This results from the spot's stronger intensity gradient in the  $x$ -direction than in the  $y$ -direction. This difference in force strength for the two directions can clearly be seen from the curves for 100 and 150 nm EVs in Figs. 2.4(a) and 2.4(c).

The global hot region of the 5  $\mu\text{m}$  trap is centered at  $x = 0$ . Therefore, for the smaller EVs the force oscillations in figure 2.4 (b) are weaker towards the facets. The hot spots near the origin thus are more preferential trapping sites, and one may expect the type of hopping motion we report in [9] towards the center of the global

hot region. For the 1000 nm EV the situation is different, since for this size the less intense hot spots near the facet lead to increasingly weaker cancellation near the facet. Preferential trapping is still at the origin, in view of the force direction imposed by the background, on which the oscillations are superimposed.

For the 15  $\mu\text{m}$  trap the global hot regions are located near the facets. For most of the diameters in figure 2.4 (c) this leads to stronger oscillations with increasing distance from the center and thus to stronger local traps near the facets. For the 1000 nm EV the changed position of the global hot region leads to weaker oscillations towards the facet, followed by a few strong oscillations as a result of entering the relatively "cold" on-axis region very close to the facet (see figure 2.3).

We now compare the forces obtained using the volumetric technique and the gradient formula Eq. 2.2. In Figs. 2.4(a) and 2.4(b) it is seen that the results for  $d_{\text{EV}} = 100$  nm agree very well. The relative root-mean-square deviation between the forces according to the models amounts to 7% for  $F_y(y)$  and 11% for  $F_x(x)$ . For  $d_{\text{EV}} = 50$  nm (curve not shown) these differences are 2.9% and 2.5% , respectively. These differences indicate that the scattering force in this size range is only a small fraction of the total force. This results from the counter-propagation of the beams of low divergence. For larger EVs the difference increases, indicating break down of the dipole approximation, on which the gradient formula is based.

Table 2.1: Normalized trap stiffnesses  $\kappa_x$  and  $\kappa_y$  of the strongest trapping sites for the three traps for diameters of core-shell EVs as indicated. The quantities  $d_{\text{EV}}$ ,  $w$ ,  $\kappa_{x(y)}$  denote EV diameter, facet separation of the trap, and stiffnesses for the  $x(y)$ -direction, respectively.

$d_{\text{EV}}$ (nm)	$w$ ( $\mu\text{m}$ )	$\kappa_x$ (fN/nm/W)	$\kappa_y$ (fN/nm/W)
50	5	5.12	0.13
	10	2.57	0.10
	15	1.81	0.09
100	5	28.63	0.80
	10	14.35	0.59
	15	10.11	0.59
150	5	72.07	2.21
	10	36.12	1.70
	15	25.41	1.71

In Table 2.1 the values of the normalized trap stiffnesses  $\kappa_x$  and  $\kappa_y$  for the traps are compiled for 50, 100 and 150 nm core-shell EVs and for the strongest trapping sites, i.e. for the most intense hot spots of the respective global hot regions. The forces for the  $y$ - and  $z$ -direction being very comparable,  $\kappa_y$  is taken as representative for  $\kappa_z$ . The Table shows that both  $\kappa_x$  and  $\kappa_y$  decrease with increasing facet separation. This arises from the decreasing maximum constructive interference of the beams. Further, all  $\kappa_x$  strongly exceed the related  $\kappa_y$  owing to the much stronger gradients in the  $x$ -direction. Finally, the systematic increase of  $\kappa_x$  and  $\kappa_y$  with EV size for each trap agrees with the diameter dependence of the power required to trap core-shell EVs (Section 2.7).

We compare the stiffnesses in Table 2.1 to those in [31], which reports trapping experiments on synthetic core-shell EVs using a focussed laser beam. For EV diameters in the range 50-150 nm lateral stiffnesses in the range 1-7 fN/nm/W are reported [31]. Our  $\kappa_x$  values in Table 2.1 clearly exceed these laser-trap values, while our  $\kappa_y$  values

are smaller. Since for a laser trap the axial stiffness is several times smaller than its lateral stiffness, it follows that the important difference and advantage of the dual-waveguide trap for trapping of these nanometer-scale EVs is the up to ten times higher stiffness in the  $x$ -direction. This results from the interference of the beams.

## 2.6. Trapping potentials

We have integrated the force curves to obtain the trapping potentials, as prescribed in Section 3. From the forces in figure 2.4, a single potential well is expected for the transverse directions and a periodic potential for the longitudinal direction. Indeed, such behavior is seen in figure 2.5, which shows the potentials  $U_y(y)/kT$  [at  $(x, z)=(0, 0)$ ] and  $U_x(x)/kT$  [at  $(y, z)=(0, 0)$ ] derived from the force curves in Figs. 2.4(a), 2.4(c), and 2.4(d) for a power of 100 mW supplied to the trap, again using half axes. The potentials are normalized to  $kT$  ( $T = 293$  K) to easily connect to the criterion for stable trapping  $U_0/kT \geq 10$ [19].

In the plot of  $U_y(y)/kT$  in figure 2.5 (a) it is seen that the 5  $\mu\text{m}$  trap cannot stably trap 100 and 150 nm homogeneous EVs in the  $y$ -direction at 100 mW. The same holds for the 100 nm core-shell EV. The 150 nm core-shell EV, however, is almost stably trapped, implying that above 150 nm core-shell EVs are all stably trapped at this power level. The potentials for homogeneous EVs of  $d_{\text{EV}} = 450, 950$  and 1000 nm each indicate stable trapping.

$U_x(x)/kT$  of the 5 and 15  $\mu\text{m}$  traps shows periodic oscillations of a strength and phase depending on EV size, superimposed on a background potential that depends on EV size as well. Background potential with superimposed oscillations are called global potential. For the smaller EVs the individual wells of the periodic potential are not deep enough for stable trapping at 100 mW. Thermally activated hopping between wells will occur. For  $d_{\text{EV}} = 450, 950$  nm the individual wells are deep enough for stable trapping, while for these diameters the background potential is more apparent. For  $d_{\text{EV}} = 1000$  nm the oscillations are virtually absent, in agreement with the force-cancellation in figure 2.4. Considering the smoother global potentials in more detail and using symmetry w.r.t.  $x = 0$ , one recognises a single potential well centred at the origin for the 5  $\mu\text{m}$  trap and a double-well potential for the 15  $\mu\text{m}$  trap (from the potential levels at either side of the cut in figure 2.5 (c), one easily sees that the single-sided curves indeed define a double-well potential). These different potential shapes agree with the respective global hot regions for the three traps.

In calculating the potentials we have applied Eqs. 2.3 and 2.4, thus stretching the range where the optical force to a good approximation is found to be conservative (up to  $d_{\text{EV}} = 100$  nm, see Section 2.5) to  $d_{\text{EV}} = 1000$  nm. To estimate the error we make in this, we have calculated for  $d_{\text{EV}} = 1000$  nm and the 5 and 15  $\mu\text{m}$  traps the line integral of the optical force along different escape paths from the trap, starting at the origin. The maximum difference we find for the paths amounts to 10%. We believe this is acceptable, also since this is a worst case scenario: with decreasing EV size the relative contribution of the scattering force becomes smaller, i.e. the approximation of conservativity becomes better.

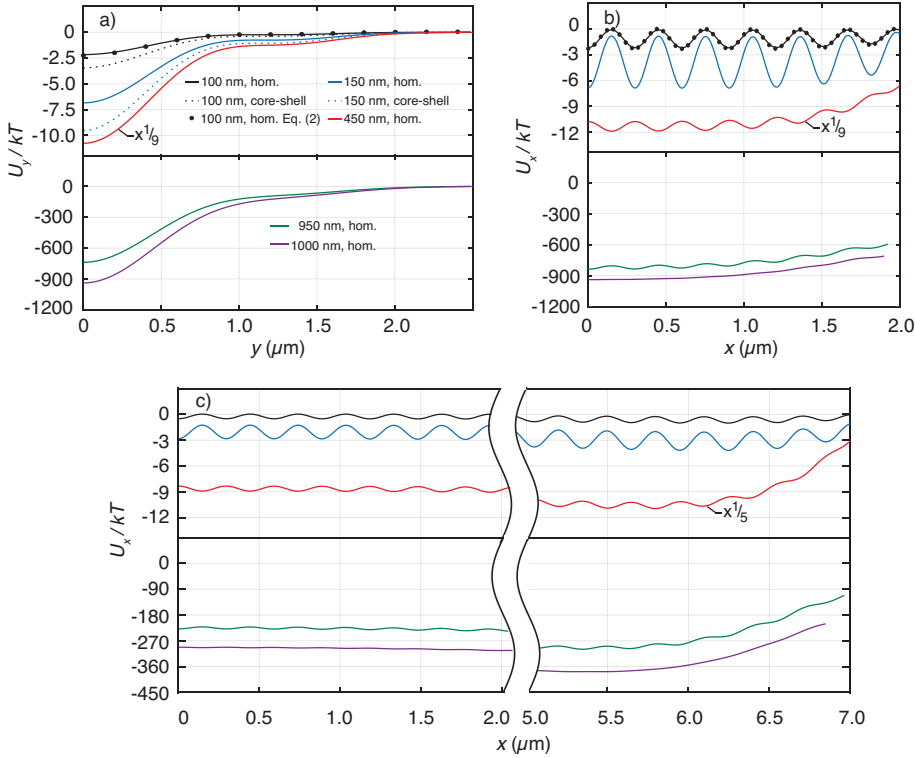


Figure 2.5: Normalized trapping potentials for the 5 and 15  $\mu\text{m}$  traps for 100 mW of optical power supplied to the traps, calculated from the force curves in figure 2.4. The legends in (a) define EV sizes and the EV index model (homogeneous versus core-shell) and apply to each panel. (a) transverse potential  $U_y(y)/kT$  for the 5  $\mu\text{m}$ . (b). Longitudinal potential  $U_x(x)/kT$  for the 5  $\mu\text{m}$  trap. (c) Longitudinal potential  $U_x(x)/kT$  for the 15  $\mu\text{m}$  trap, with part of the  $x$ -axis omitted to obtain the same horizontal scale as in (a) and (b).

## 2.7. Trapping stability

In line with Ashkin's criterion, the minimum power  $P_{\min}$  for stable trapping of an EV is defined by the demand that the depth of the normalized potential well in the three directions equals 10. We first make this demand explicit for the three potential wells obtained.

*The transverse potential well* is the well  $U_y/kT$  defined by curves as in figure 2.5 (a). We take the transverse axis through the  $x$ -position of the most intense hot spot, which for the 5, 10 and 15  $\mu\text{m}$  traps is at  $x = 0, \pm 3.6$  and  $\pm 6.3$   $\mu\text{m}$ , respectively. In figure 2.6 (a)  $U_y/kT$  is plotted for stable trapping in the 5  $\mu\text{m}$  trap. We define the maximum excursion during confined Brownian motion as the distance from  $y = 0$  to either of the knee points of the curve (indicated by arrows in figure 2.6 (a)), which is located closer to  $y = 0$  than the classical turning points at  $U_y/kT = 10$ . So, we avoid the strong influence of the very flat wings of the well. We thus get a single-sided excursion of 1.0  $\mu\text{m}$ . The overall picture for  $U_z/kT$  is similar.

*The deepest local well of the longitudinal potential* is, depending on EV size, the deepest local well of  $U_x/kT$  at the most intense hot spot or in between the two most intense hot spots (see figure 2.5 (b) for these situations). In figure 2.6 (b)  $U_x/kT$  is

plotted for stable trapping in the central local well of the 5  $\mu\text{m}$  trap. Local well depths near the centre being close, this case also represents stable trapping near the center. The single-sided maximum excursion is about 150 nm (i.e., half of the modulation period). Each of the local trapping wells near the center can be filled with one or more EVs. Access to each of these traps can be provided by translating the chip under the microscope objective for Raman spectroscopy or by shifting the interference pattern by applying a phase difference to the beams forming the trap using on-chip heaters.

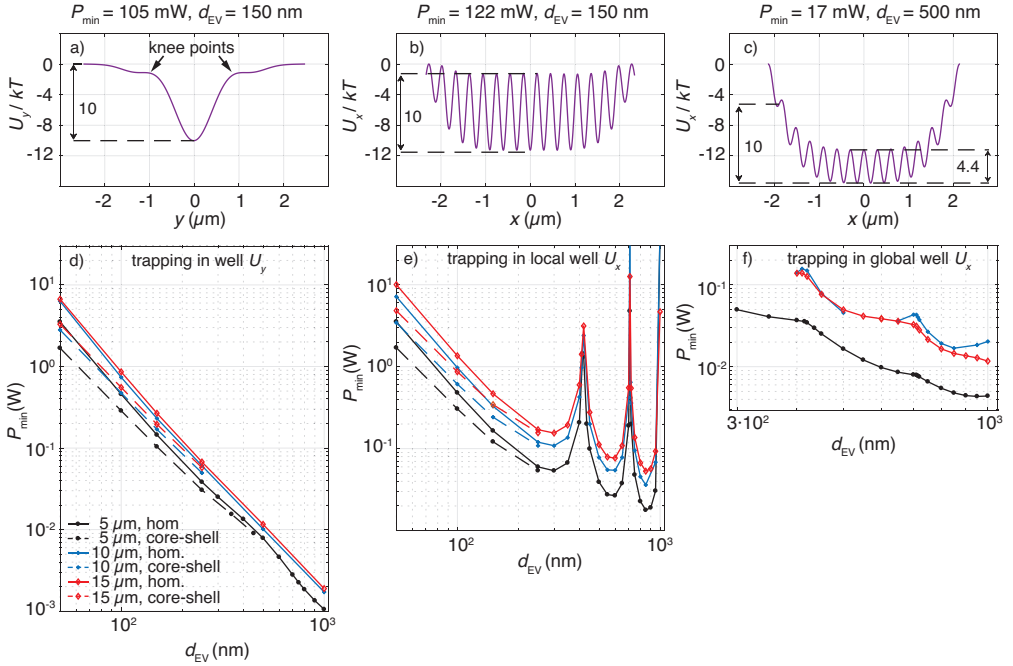


Figure 2.6: (a)-(c) Potential wells for the 5  $\mu\text{m}$  trap in case of stable trapping under conditions as indicated above the panels. (a) The transverse well  $U_y/kT$ . The indicated knee points limit the confined Brownian motion, as discussed in the text. (b) The deepest local well of  $U_x/kT$ . (c) The global well  $U_x/kT$ . (d)-(f) Stability curves for the three wells as mentioned in the panels. The legends in (d) define the trap sizes and the EV index model (homogeneous versus core-shell) and apply to each of the stability curves in (d), (e) and (f).

The *global longitudinal potential well*  $U_x/kT$  is defined as the background potential with superimposed oscillations. EV trapping in the global potential is only fundamentally different from trapping in an individual well if the potential's oscillatory part is weak compared to the background. If not, the EV can still spend considerable time in a single local well or EV motion is dominated by hopping between such wells. With some arbitrariness, we translate this to the additional demand that the ratio of the deepest local well to the global well depth of 10 is smaller than 0.6. For the 5  $\mu\text{m}$  trap we find  $P_{\text{min}}$  by making the well depth equal to 10 for classical turning points at  $x = \pm 1.9 \mu\text{m}$ , where the largest EV does just not touch the facet. This also defines the maximum excursion of 1.9  $\mu\text{m}$ . The demand of a weak enough oscillatory potential leads to the condition  $d_{\text{EV}} \geq 300 \text{ nm}$ . In figure 2.6 (c) by  $U_x/kT$  is plotted for stable

trapping in the global well of the 5  $\mu\text{m}$  trap.

For the 10 and 15  $\mu\text{m}$  traps  $P_{\text{min}}$  is chosen such that the barrier height between the global wells of the double-well potential amounts to 10. For these traps the minima of the individual wells coincide with aforementioned positions of the most intense hot spots. Taking half of the maximum double-sided excursion for these asymmetric wells, we get the maximum single-sided excursions 1.8 (3.1)  $\mu\text{m}$  for the 10 (15)  $\mu\text{m}$  trap. The demand of a weak enough oscillatory potential leads to the condition  $d_{\text{EV}} \geq 300$  (400) nm for the 5 (10 and 15)  $\mu\text{m}$  trap, while for the 10  $\mu\text{m}$  traps the range 500–650 nm is excluded.

Applying the demand of stable trapping to the three wells leads to the stability curves in Figs. 2.6(d)–2.6(f) for the traps. A stability curve is a plot of  $P_{\text{min}}$  versus  $d_{\text{EV}}$ . Points on and above a stability curve define stable trapping, while for points below a curve an EV cannot be stably trapped. Figures 2.6(d) and 2.6(e) are for both index models. Figure 2.6(f) is for the homogeneous index.

Figure 6(d) for  $U_y/kT$  shows that  $P_{\text{min}}$  at fixed  $d_{\text{EV}}$  increases with increasing trap size, the curves for the 10 and 15  $\mu\text{m}$  traps being close. This agrees with the decreasing energy density of the most intense hot spot with increasing trap size in figure 2.3. For small homogeneous EVs with  $d_{\text{EV}} \leq 150$  nm the curves are straight lines of a slope very close to  $-3$ . Thus, we approximately have  $P_{\text{min}} \propto 1/d_{\text{EV}}^3$ , in agreement with Eq. 2.2 and therefore with a dominating gradient force. For core-shell EVs with  $d_{\text{EV}} < 150$  nm, we find  $P_{\text{min}} \propto 1/d_{\text{EV}}^{2.56}$ , while for each trap the core-shell curve lies below the curve for the homogeneous EVs. These properties of the core-shell curves agree with the stronger force acting on core-shell EVs than on homogeneous EVs. Beyond this range, the curves of core-shell EVs asymptotically approach those of homogenous EVs. For 450 nm the effect of the core can still be seen in figure 2.6 (d).

In figure 2.6 (e), for small  $d_{\text{EV}}$ , the curves for the deepest local well of  $U_x/kT$  show similar behavior as in figure 2.6 (d). Different from figure 2.6 (d), however, and very prominent are the strong and broad peaks at  $d_{\text{EV}} \approx 420, 700$  and 1000 nm. For these diameters the oscillatory potential's amplitude is close to zero due to the cancellation effect. As a result, high powers are needed to create deep enough wells for stable trapping.

In figure 2.6 (f) the main features are the residues of the peaks in figure 2.6 (e). The weakness of these features results from the dominance of the background potential in its interplay with the oscillatory potential. Further comparison of figure 2.6 (f) with figure 2.6 (e) shows that for each trap the  $P_{\text{min}}-d_{\text{EV}}$  curve for trapping in the global well lies below the curve for trapping in the local well. Thus, when increasing the power at fixed  $d_{\text{EV}}$ , trapping is first realized in a global well, followed by trapping in a local well when the power hits the stability curve for local trapping. Finally, by considering the various global potential wells in detail, it is seen that for the 5  $\mu\text{m}$  trap the effect of the oscillations is smallest, as their amplitude is negligible at the classical turning points. For the 10 and 15  $\mu\text{m}$  traps the features are stronger due to relatively strong oscillations present at the barrier of the double-well potential. The curve of the 5  $\mu\text{m}$  trap is below those of the other traps. This relates to energy densities in figure 2.6.

In Figs. 2.6(d)–2.6(f)  $P_{\text{min}}$  covers the range from 1 mW at 1000 nm to 10 W at 50 nm (neglecting the peak values around 700 and 1000 nm). For Raman spectroscopy

limited EV excursions in the trap are preferred, suggesting trapping in a local well of  $U_x/kT$ . 300 mW can be supported by the glued butt coupling of a fiber to the waveguide facet at the chip edge and by the waveguide itself [32]. The maximum coupling efficiency between fiber and waveguide is 89% [32] and the estimated loss of the Y-junction used [9] to split the entrance waveguide into two waveguides routed to the trapping region is  $-1.0$  dB [32]. We thus arrive at a power of 210 mW available for trapping, which is in the range for Raman spectroscopy on single EVs [10–12]. Figures 2.6 (d) and 2.6 (e) indicate that with the 5  $\mu\text{m}$  trap core-shell EVs of many diameters outside the peaks, down to the smallest diameter of 115 nm, can be trapped for  $P_{\text{min}}=210$  mW. In 10 and 15  $\mu\text{m}$  traps this  $P_{\text{min}}$  enables stable trapping of a core-shell EV as small as 155 and 180 nm, respectively. With these smallest EVs that can be trapped, the largest part of the EV size range is covered. We thus argue that the size range that is addressed with our integrated photonics lab-on-a-chip device is clinically relevant, also in view of the results in [33], where it is demonstrated that already big EVs of a diameter of 1  $\mu\text{m}$  can be used to diagnose prostate cancer.

## 2.8. Conclusion and outlook

We have presented the capabilities of dual-waveguide traps based on box-shaped composite SiO<sub>2</sub>-Si<sub>3</sub>N<sub>4</sub> waveguides for optical trapping of extracellular vesicles (EVs), using FDTD simulations and optical force calculations. EVs are very tiny spherical, cell-derived particles of diameter in the range 30–1000 nm and have a low index contrast w.r.t. water and therefore are hard to trap. EVs attract strong attention as potential markers for cancer.

Owing to both the small size and special structure of the waveguides, the counter-propagating beams are narrow and weakly divergent, properties favorable for a tight optical trap. For facet spacings of 5, 10 and 15  $\mu\text{m}$  the optical field between the facets shows clear interference maxima or hot spots, leading to an oscillatory force acting on an EV as a function of its position and thus to multiple trapping sites. For certain EV sizes the forces exerted by several hot spots cancel and only a global longitudinal force remains.

By calculating forces using Lumerical's volumetric technique for EV diameters in the range 50–1000 nm using two refractive index distributions, viz. homogeneous and that of the realistic core-shell structure, we find that the shell, though only 5 nm thick, contributes considerably to the force up to a diameter of 450 nm. By comparing these forces with forces obtained using the gradient formula, we conclude that the gradient force clearly dominates the total force up to 100 nm EV diameter. This results from counter-propagation of the beams. Longitudinal trap stiffnesses derived from the force curves are up to ten times higher than the lateral stiffness of a laser-beam trap, a quality resulting from the interference.

The trapping potentials derived from the force curves lead to the so-called stability curves (i.e., curves of the minimum optical power required for stable EV trapping as a function of EV size). These curves indicate that EVs of a wide diameter range can be stably trapped with the attainable trapping power of 210 mW, down to a smallest size of 115 nm for the 5  $\mu\text{m}$  trap. This capability in combination with the power level sufficient for Raman spectroscopy of the trapped EV, qualify this dual-waveguide trap as a promising lab-on-a-chip device with clinical relevance. Finally, we note that the

drag force acting on an EV in a trap under fluidic flow can be incorporated in our procedure, leading to modified stability curves. Based on these, the smallest EV that can be stably trapped in the flow situation can again be chosen by setting the optical power, allowing all smaller EVs to be collected downstream. This defines the principle of a size filter for EVs and can be generalized to other bio-particles, such as proteins, cell fragments, and so forth.

As a short outlook, we mention that a multiple-waveguide geometry is a logical extension of the geometry presented here. Multiple waveguides lead to stronger light concentration and thus a stronger trap, since an interference pattern is created with beams coming from many directions. We have a fabrication run underway for dual-, quad-, and octo-waveguide traps tailored for experimental trapping and Raman studies of EVs.

## 2.9. Funding

Netherlands Organisation for Scientific Research (NWO) (14197); NWO Physical Sciences, (15316).

## 2.10. Acknowledgements

The authors thank M.R. Fanood and R.J. Moerland for stimulating discussions, A. Nanou for critical reading of the manuscript and R. Nieuwland for making us aware of reference 14. F. Schreuder, M. Hoekman and A. Leinse are acknowledged for their input on the composite  $\text{SiO}_2\text{-Si}_3\text{N}_4$  (TripleX) waveguides and E. van der Pol and A.G.J.M. van Leeuwen for sharing knowledge on extracellular vesicles. NWO Physical Sciences made the Supercomputer Cartesius available for the simulations (15316).

## References

- [1] G. Luka, A. Ahmadi, H. Najjaran, E. Alocilja, et al., "Microfluidics integrated biosensors: a leading technology towards lab-on-a-chip and sensing applications," *Sensors (Basel)* 15(12), 30011–30031 (2015).
- [2] J. W. Chan, "Recent advances in laser tweezers Raman spectroscopy (LTRS) for label-free analysis of single cells," *J. Biophotonics* 6(1), 36–48 (2013).
- [3] P. R. T. Jess, V. Garcés-Chávez, D. Smith, M. Mazilu, et al., "Dual beam fibre trap for Raman micro-spectroscopy of single cells," *Opt. Express* 14(12), 5779–5791 (2006).
- [4] S. Dochow, M. Becker, R. Spittel, C. Beleites, et al., "Raman-on-chip device and detection fibres with fibre Bragg grating for analysis of solutions and particles," *Lab Chip* 13(6), 1109–1113 (2013).
- [5] N. Bellini, K. C. Vishnubhatla, F. Bragheri, L. Ferrara, et al., "Femtosecond laser fabricated monolithic chip for optical trapping and stretching of single cells," *Opt. Express* 18(5), 4679–4688 (2010).
- [6] F. Bragheri, L. Ferrara, N. Bellini, K. C. Vishnubhatla, et al., "Optofluidic chip for single cell trapping and stretching fabricated by a femtosecond laser," *J. Biophotonics* 3(4), 234–243 (2010).

- 2
- [7] O. G. Hellesø, P. Løvhaugen, A. Z. Subramanian, J. S. Wilkinson, and B. S. Ahluwalia, "Surface transport and stable trapping of particles and cells by an optical waveguide loop," *Lab Chip* 12(18), 3436–3440 (2012).
- [8] P. Løvhaugen, B. S. Ahluwalia, T. R. Huser, and O. G. Hellesø, "Serial Raman spectroscopy of particles trapped on a waveguide," *Opt. Express* 21(3), 2964–2970 (2013).
- [9] M. Boerkamp, T. van Leest, J. Heldens, A. Leinse, et al., "On-chip optical trapping and Raman spectroscopy using a TripleX dual-waveguide trap," *Opt. Express* 22(25), 30528–30537 (2014).
- [10] I. Tatischeff, E. Larquet, J. M. Falcón-Pérez, P. Y. Turpin, and S. G. Kruglik, "Fast characterisation of cell-derived extracellular vesicles by nanoparticles tracking analysis, cryo-electron microscopy, and Raman tweezers microspectroscopy," *J. Extracell. Vesicles* 1(1), 19179 (2012).
- [11] R. P. Carney, S. Hazari, M. Colquhoun, D. Tran, et al., "Multispectral optical tweezers for biochemical fingerprinting of CD9-positive exosome subpopulations," *Anal. Chem.* 89(10), 5357–5363 (2017).
- [12] Z. J. Smith, C. Lee, T. Rojalin, R. P. Carney, et al., "Single exosome study reveals subpopulations distributed among cell lines with variability related to membrane content," *J. Extracell. Vesicles* 4(1), 28533 (2015).
- [13] F. Properzi, M. Logozzi, and S. Fais, "Exosomes: the future of biomarkers in medicine," *Biomarkers Med.* 7(5), 769–778 (2013).
- [14] J. Skog, T. Würdinger, S. van Rijn, D. H. Meijer, et al., "Glioblastoma microvesicles transport RNA and proteins that promote tumour growth and provide diagnostic biomarkers," *Nat. Cell Biol.* 10(12), 1470–1476 (2008).
- [15] W. J. Allard, J. Matera, M. C. Miller, M. Repollet, et al., "Tumor cells circulate in the peripheral blood of all major carcinomas but not in healthy subjects or patients with nonmalignant diseases," *Clin. Cancer Res.* 10(20), 6897–6904 (2004).
- [16] S. A. Melo, L. B. Luecke, C. Kahlert, A. F. Fernandez, et al., "Glypican-1 identifies cancer exosomes and detects early pancreatic cancer," *Nature* 523(7559), 177–182 (2015).
- [17] W. Lee, A. Nanou, L. Rikkert, F. A. Coumans, et al., "Label-free prostate cancer detection by characterization of extracellular vesicles using raman spectroscopy," *Analytical chemistry* 90(19), 11290–11296 (2018).
- [18] S. Vyawahare, A. D. Griffiths, and C. A. Merten, "Miniaturization and parallelization of biological and chemical assays in microfluidic devices," *Chem. Biol.* 17(10), 1052–1065 (2010).
- [19] A. Ashkin, J. M. Dziedzic, J. E. Bjorkholm, and S. Chu, "Observation of a single-beam gradient force optical trap for dielectric particles," *Opt. Lett.* 11(5), 288–290 (1986).

- [20] TriPleX is a trademark for the waveguide technology of LioniX International BV.
- [21] K. Wörhoff, R. G. Heideman, A. Leinse, and M. Hoekman, "TriPleX: a versatile dielectric photonic platform," *Adv. Opt. Technol.* 4(2), 189–207 (2015).
- [22] E. van der Pol, A. N. Böing, P. Harrison, A. Sturk, and R. Nieuwland, "Classification, functions, and clinical relevance of extracellular vesicles," *Pharmacol. Rev.* 64(3), 676–705 (2012).
- [23] W. Choi, C. Fang-Yen, K. Badizadegan, S. Oh, et al., "Tomographic phase microscopy," *Nat. Methods* 4(9), 717–719 (2007).
- [24] H. J. van Manen, P. Verkuijlen, P. Wittendorp, V. Subramaniam, et al., "Refractive index sensing of green fluorescent proteins in living cells using fluorescence lifetime imaging microscopy," *Biophys. J.* 94(8), L67–L69 (2008).
- [25] Lumerical FDTD Solutions, Inc., <http://www.lumerical.com/tcad-products/fdtd/> (accessed June 26, 2018).
- [26] The expression for the gradient force goes back to Eq. (2) of [16], the pioneering work of A. Ashkin. The difference with Eq. (2) in [16] involves typographic errors and our prefactor  $n$  instead of  $(1/2)$ . Further, our equation has no minus sign and gives the direction of the force vector. Finally, we use SI units.
- [27] P. Zemánek, A. Jonaš, L. Šrámek, and M. Liška, "Optical trapping of Rayleigh particles using a Gaussian standing wave," *Opt. Commun.* 151(4–6), 273–285 (1998).
- [28] M. Y. Wu, D. X. Ling, L. Ling, W. Li, and Y. Q. Li, "Stable optical trapping and sensitive characterization of nanostructures using standing-wave Raman tweezers," *Sci. Rep.* 7(18042), 42930 (2017).
- [29] M. M. van Leest, F. Bernal Arango, and J. Caro, "Optical forces and trapping potentials of a dual-waveguide trap based on multimode solid-core waveguides," *J. Eur. Opt. Soc.* 6, 11022 (2011).
- [30] J. Ježek, P. Zemánek, A. Jonáš, M. Šery, et al., "Behavior of nanoparticle and microparticle in the standing wave trap," *Proc. SPIE* 4356, 318–326 (2001).
- [31] P. M. Bendix and L. B. Oddershede, "Expanding the optical trapping range of lipid vesicles to the nanoscale," *Nano Lett.* 11(12), 5431–5437 (2011).
- [32] F. Schreuder, LioniX International BV, Hengelosestraat 500, 7521 AN Enschede, The Netherlands (personal communication, 2018).
- [33] A. Nanou, F. A. W. Coumans, G. van Dalum, L. L. Zeune, et al., "Circulating tumor cells, tumor-derived extracellular vesicles and plasma cytokeratins in castration-resistant prostate cancer patients," *Oncotarget* 9(27), 19283–19293 (2018).



# 3

## Multi-waveguide devices for optical trapping and Raman spectroscopy: design, fabrication & performance demonstration

*We realize integrated photonics multi-waveguide devices for optical trapping and Raman spectroscopy of particles in a fluid. Multiple beams directed towards the device center lead to local field enhancement and thus diminish the relative importance of the light concentration near the facets, a disadvantageous property of dual-waveguide traps. Thus, a region of preferential trapping is defined around the device center, where a single particle in a wide size range can be trapped and studied spectroscopically, free from surfaces. We report design (including simulations), fabrication and performance demonstration, using our  $\text{Si}_3\text{N}_4$  waveguiding platform as the basis. The 1000 nm wide and 100 nm thick ridge waveguides, optimized for trapping and Raman, emit narrow beams. Multiple waveguides arranged around the central microbath result from fanning out of a single input waveguide using Y-splitters. A second waveguiding layer, with 200 nm thick waveguides and maximum width of 13.5  $\mu\text{m}$ , is implemented for Raman detection. For reliable infilling of the device with sample fluid, microfluidic considerations lead to side channels of the microbath, to exploit capillary forces. According to design, interference of the multiple beams produces an array of hot spots around the bath center, each forming a local trap. This property is clearly confirmed in the experiments and is registered in added movies. We demonstrate the performance of a 2 waveguide and a 16 waveguide device, using 1  $\mu\text{m}$  and 3  $\mu\text{m}$  polystyrene beads. Study of the confined Brownian motion of trapped beads yields normalized trap stiffnesses for the in-plane directions. The stiffness values for the 16 waveguide device are comparable to those of tightly focused Gaussian beam traps and are confirmed by our own simulations. The Raman spectra of the beads, in this work measured via an objective, show clear peaks characteristic of polystyrene. For low wavenumbers the spectra have a background, that is generated in the  $\text{Si}_3\text{N}_4$  waveguides.*

---

As published in: G.B. Loozen, A. Karuna, M.M. Fanood, E. Schreuder and J. Caro, "Integrated photonics multi-waveguide devices for optical trapping and Raman spectroscopy: design, fabrication and performance demonstration," *Beilstein Journal of nanotechnology* **11**(1), 829-842 (2020).

### 3.1. Introduction

Photonic lab-on-a-chip (LOC) techniques strongly attract attention for the manipulation and measurement of bio-particles such as bacteria and various types of biological cells [1]. In this context LOC devices for optical trapping and Raman spectroscopy are very promising. Such devices are on-chip versions of a laser-tweezers Raman spectroscopy (LTRS) setup, a free space optics instrument. In LTRS, optical trapping and Raman spectroscopy of a particle are carried out using a focused laser beam, enabling label-free analysis of single cells in an aqueous suspension and away from surfaces [2]. For on-chip trapping and Raman spectroscopy, the dual-beam trap based on fibers or integrated photonics waveguides is studied extensively [3–6]. This trap comprises two excitation fibers or excitation waveguides, which emit counter-propagating beams into a fluidic environment, often a fluidic channel for particle delivery. The beams interfere and create a volume of highly concentrated light, suitable for optical trapping and Raman spectroscopy.

In [3], for example, a dual-fiber trap is used to trap tumor cells and blood cells, while Raman spectra are induced and collected by an external spectroscopy system. This work is extended in [4], using fibers for both trapping of single polystyrene beads and Raman excitation and collection for these beads. In our work [5], we use integrated photonics  $\text{Si}_3\text{N}_4$  waveguides of a box shape and demonstrate for polystyrene beads simultaneous optical trapping and Raman excitation using the same counter-propagating beams. The important advantage of using integrated photonics waveguides is in the high degree of control in fabrication, down to the nanometer-scale, and in mass producibility. In [6] we present a detailed simulation study of the trapping capabilities for extracellular vesicles (EVs) of the dual-waveguide trap we use in [5]. EVs are small cell derived particles (diameter ranging from 30 nm to 1000 nm) and are important as potential biomarkers for cancer. In [6] we find, due to divergence of the emitted beams, that larger facet separations ( $\geq 10 \mu\text{m}$ ) lead to a strong global hot region of the light field near the waveguide facets. These global hot regions define preferential trapping sites, which may lead to adherence of the particle to the facets and disturbance of its Raman spectrum due to particle-surface interaction, effects to be avoided. Here, we solve the problem of a global hot region near the facets by realizing multi-waveguide devices for trapping and Raman spectroscopy. Multiple  $\text{Si}_3\text{N}_4$  waveguides launch multiple beams towards the center of the device, leading to field enhancement in the central region and thus diminishing the relative importance of the light concentration near the facets. In this way a region of preferential trapping is realized around the device center, where a single particle of a size in a wide range can be studied free from surfaces, while being trapped in the aqueous medium. In figure 3.1 we present a schematic drawing of the device concept with multiple waveguides. These are arranged around a cylindrical fluidic microbath that can be infilled with a suspension of particles. The concept of light concentration in the device center was first proposed and realized in [7], but in that case fibers were used.

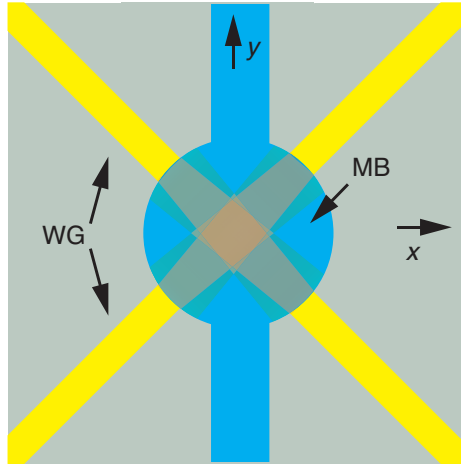


Figure 3.1: Schematic of the device concept with multiple waveguides, here with four waveguides. Beams emitted from the waveguides (WG) into the microbath (MB) overlap in the central region, where interference and field enhancement occur. The schematic defines the direction of the Cartesian coordinates  $x$  and  $y$ , with the origin placed in the microbath center.

This chapter is organized as follows. In the section on design of the multi-waveguide devices, we present the design of the excitation waveguides, the detection waveguides and the microbath. For the waveguides, we arrive at specific choices from the  $\text{Si}_3\text{N}_4$  waveguiding platform we have available. In the experimental section we present the fabrication process of the devices, and describe the experimental setup and preparation of the sample for the performance demonstration of our devices. In the results and discussion section we demonstrate the performance of the multi-waveguide devices, both for trapping and Raman spectroscopy. In the demonstration we compare a 2 waveguide device with a 16 waveguide device and use polystyrene beads as test particles. Finally, we present the conclusions of our study.

### 3.2. Design of the multi-waveguide devices for trapping and Raman spectroscopy

We carried out extensive design procedures for the multi-waveguide devices to arrive at optimum designs for their functional parts. These functional parts are described in the following (see figure 3.1).

1. The excitation waveguides and their circuitry

Here, we simulated the beam emitted by the waveguide as a function of the waveguide width, designed the connecting circuitry of the excitation waveguides, calculated the fiber-to-waveguide transmission, and finally, simulated the energy density in the microbath resulting from the multiple beams.

2. The detection waveguides and their circuitry

In this case, the main design approach was to optimize the collection efficiency of the detection waveguides, which is determined by the area of their input facets and the distance to the microbath center.

## 3. The microbath

The design of the microbath was guided by common microfluidic considerations, also making sure that the microbath is compatible with the geometry of the excitation waveguides.

### 3.2.1. The excitation waveguides, their circuitry and their arrangement around the microbath

The light beams emitted by the multiple excitation waveguides should lead to a strong light concentration in the central region of the microbath. This implies that the beams should be narrow and have a low divergence. To realize this, we chose the singlestripe waveguide of our TripleX waveguiding platform [9]. This is a rectangular  $\text{Si}_3\text{N}_4$  ridge waveguide embedded in  $\text{SiO}_2$  cladding. The TripleX platform offers high transparency across the wide wavelength range of 405–2350 nm, which includes our laser wavelength of 785 nm used for trapping and Raman spectroscopy. Single-stripe waveguides require considerably fewer fabrication steps than the box-shaped TripleX waveguides we used before [5, 6]. This is the reason for our choice, where we take into account that the present devices, apart from the excitation waveguides, also have detection waveguides located in a separate waveguiding layer.

#### Excitation waveguides

To determine the thickness of the excitation waveguides, we simulated the beam emitted from the facet into water (the typical medium in our experiments) for various waveguide thicknesses using the 3D finite-difference time-domain (FDTD) method with Lumerical's FDTD solutions [10]. We choose a waveguide width  $w_{\text{exc}}$  of  $1 \mu\text{m}$ , which is the minimum width for the contact lithography we use. We aim for single-mode operation of the waveguides at 785 nm for the transverse magnetic (TM) polarization. For TM polarization, the electric field vector  $\vec{E}$  of the waveguide mode is directed perpendicular to the plane of the waveguide (the  $x$ - $y$  plane, as indicated in figure 3.1). This polarization is conserved in the emitted beam. For a multiwaveguide configuration as shown in figure 3.1, the polarization of each beam then points in the same direction. For equal optical path lengths from the waveguide facets to the microbath center and for beams leaving the facets in phase, the light concentration in the center reaches the maximum obtainable value for the TM polarization, as a result of optimum constructive interference. For transverse electric (TE) polarization, for which the electric field vector  $\vec{E}$  of the beams is oriented in the  $x$ - $y$  plane, the resulting light concentration is lower.

In the simulations, the refractive index of silicon nitride, silicon oxide and water is chosen as  $n_{\text{Si}_3\text{N}_4} = 2.00$ ,  $n_{\text{SiO}_2} = 1.45$ , and  $n_{\text{H}_2\text{O}} = 1.33$ , respectively. To obtain the characteristics of the emitted beams, we follow the simulation approach of our previous work [6]. Figure 3.2 (a) shows the longitudinal profiles of the energy density  $U$  of the electric field (per watt of power delivered to the waveguide mode) of the beams emitted into water and for waveguide thicknesses  $t = 50, 100$  and  $150 \text{ nm}$ . The  $x$ -axis is the axis of the waveguide. While for  $t = 50 \text{ nm}$  the profile is flattest (and thus the least divergent), the profile for  $t = 100 \text{ nm}$  has the highest energy density in the  $x$ -range of  $1.5$ – $4.5 \mu\text{m}$ . The latter property is advantageous for multiple waveguides around a microbath with a radius of about  $3 \mu\text{m}$  (optimum for, say, 1

$\mu\text{m}$  diameter particles and smaller), since the strongest field enhancement can be realized using multiple beams for such a microbath size. A thickness of  $t = 100\text{ nm}$  is also appropriate for larger microbaths (more suitable for particles larger than  $1\ \mu\text{m}$ ), since larger particles require a lower concentration of light for trapping and Raman spectroscopy. We thus choose  $t = 100\text{ nm}$ . For this thickness, only a single TM mode can exist in the waveguide. In figure 3.2 (b) and figure 3.2 (c), we show the energy density of the beam emitted by the  $100\text{ nm}$  thick waveguide in the  $x$ - $y$  and the  $x$ - $z$  plane, respectively. The highest density occurs close to the facet, followed by a decay, which are features also seen in figure 3.2 (a). The beam in the  $x$ - $z$  plane shows less lateral spreading than in the  $x$ - $y$  plane, indicating that the width of  $1\ \mu\text{m}$  is not limiting here in obtaining a narrow beam.

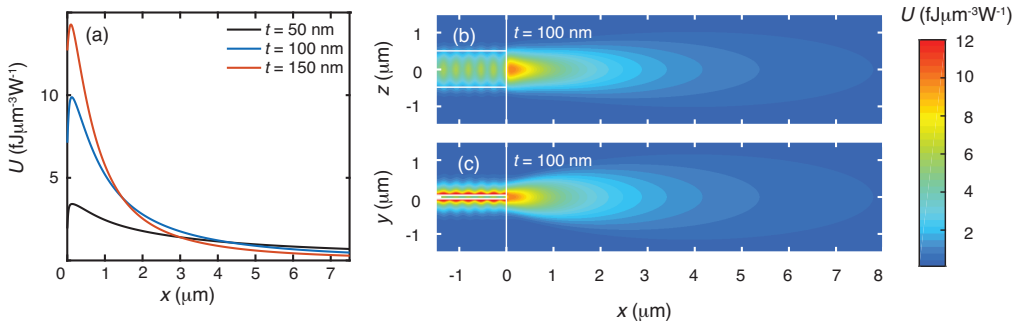


Figure 3.2: (a) Longitudinal profiles of the energy density  $U$  along the beam axis for waveguide thicknesses of 50, 100 and 150 nm, for 1 W of power delivered to the waveguide mode. The waveguide width is  $1\ \mu\text{m}$ . (b) and (c) show  $U$  of the beam emitted into water by the  $100\text{ nm}$  thick waveguide in the  $x$ - $z$  plane and the  $x$ - $y$  plane, respectively. Color bar calibrated for 1 W of power delivered to the waveguide mode. The white vertical lines indicate the facet position, while the white horizontal lines indicate the waveguide. The periodic pattern inside and outside the waveguide in (b) and (c) results from the interference of the forward propagating mode and the mode partially backreflected at the nitride–water interface.

### Connecting circuitry of the excitation waveguides

For introducing light into the multiple excitation waveguides, we have designed connecting circuitry comprising waveguides of the same dimensions as the excitation waveguides. Starting from the chip edge, a single input waveguide (to which a fiber can be coupled) fans out using 50/50 Y-splitters into multiple waveguides, which connect to the excitation waveguides of the specific device design. This multi-waveguide circuitry across the chip is designed with a script-based editor of Synopsys (OptoDesigner) for efficient waveguide routing, guided by the symmetry of the configuration of the excitation waveguides. In this we impose a minimum waveguide-bend radius of  $300\ \mu\text{m}$  to avoid bend losses exceeding  $-0.01\ \text{dBcm}^{-1}$ . The underlying relation of bend loss versus bend radius was obtained from simulations. The estimated scattering loss at each Y-splitter is  $-0.5\ \text{dB}$ . The intrinsic waveguide propagation loss for the chosen width and thickness is  $-0.5\ \text{dBcm}^{-1}$ . For the waveguide lengths used, the intrinsic waveguide propagation loss is negligible compared to the losses just mentioned. Figure 3.6 (d) below gives an impression of the connecting circuitry of a 16-waveguide device.

### Fiber-to-waveguide coupling

To optimize the light coupling from a single-mode polarization maintaining fiber (a Thorlabs PM780-HP fiber, mode-field diameter of  $5.3 \mu\text{m}$ ) to the input waveguide at the chip edge, we numerically calculate the fiber-to-waveguide power transmission as a function of waveguide width and thickness. For this we use the overlap-integral expression for the electric fields of the fiber mode and the waveguide mode. The results are plotted in figure 3.3. For  $w_{\text{exc}} = 1 \mu\text{m}$ , a thickness  $t$  between 35 and 40 nm yields optimum transmission of  $-0.5 \text{ dB}$  or 89 %. We further calculate the tolerance of the transmission against fabrication variability of the waveguide width and thickness, using thickness and width variations of  $\pm 5 \text{ nm}$  and  $\pm 200 \text{ nm}$ , respectively. This leads to the choice  $t = 35 \text{ nm}$  at the chip edge. To obtain a thickness of 35 nm for the input waveguide at the chip edge, the waveguide is tapered down towards the chip edge (see subsection on fabrication below).

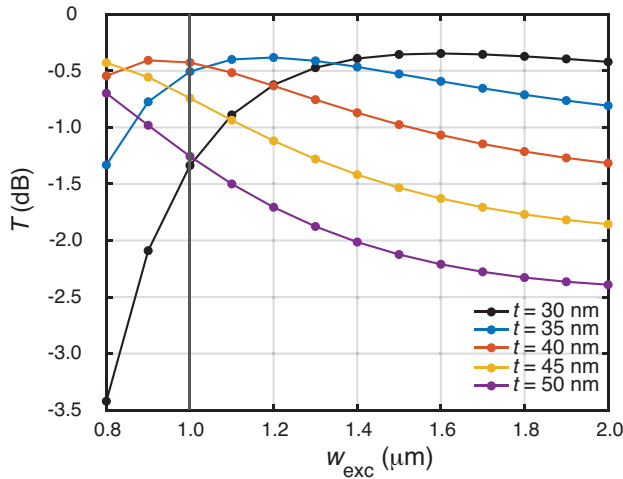


Figure 3.3: Fiber-to-chip transmission  $T$  as a function of the waveguide width  $w_{\text{exc}}$  for various thicknesses  $t$ . The vertical line indicates the chosen waveguide width.

### Energy density in the microbath

We have designed various multi-waveguide devices with excitation waveguides of the type chosen above, with the number of waveguides varying between 2 and 32. In this work, we focus on experiments with a 2-waveguide and a 16-waveguide device. The 2-waveguide device has a linear,  $15 \mu\text{m}$  wide fluidic channel with a rectangular cross section between the waveguides, while the 16-waveguide device has a cylindrical fluidic microbath with a diameter of  $15 \mu\text{m}$ . Using Lumerical's FDTD solutions, we obtain the energy density  $U$  in the central part of these devices, assuming the beams are emitted in phase. The results are presented in figure 3.4. The 2-waveguide device (figure 3.4 (a)) shows a characteristic periodic pattern for  $U$ , with high values near the facets (global hot region). This pattern results from the interference of the emitted counter-propagating beams. The distance between the interference maxima is  $785 \text{ nm}/(2n_{\text{H}_2\text{O}}) = 295 \text{ nm}$ . Each interference maximum (local hot spot) is clearly narrower in the  $x$ -direction than in the  $y$ -direction. Particles can be trapped at the local hot spots.

The global hot regions are preferential trapping regions. These may pose a problem for larger particles in view of possible adherence to the facet. For the 16-waveguide device, the interference pattern is completely different, as shown in figure 3.4 (b). In this case there is a global hot region in the center of the microbath, resulting from the interference of the 16 beams, as intended. This is the preferential trapping region of this device. The structure of the global hot region is magnified in the inset of figure 3.4 (b), showing that the hottest spot has two strong side lobes. Further outwards the lobes become increasingly weaker. The individual local hot spots at and near the center serve as local traps for small particles ( $\leq 295$  nm, the typical distance between maxima of  $U$ ), while larger particles are trapped as a result of the forces exerted by the multiple hot spots.

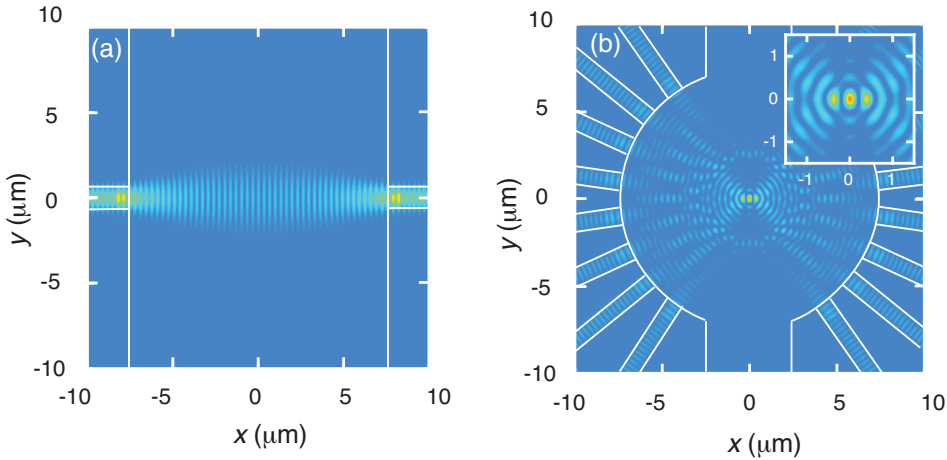


Figure 3.4: Energy density of the electric field in the multi-waveguide devices used in experimental demonstrations in this work. (a) 2-waveguide device with a  $15 \mu\text{m}$  wide fluidic channel. (b) 16-waveguide device with a  $15 \mu\text{m}$  diameter microbath and  $5 \mu\text{m}$  wide side channels. The waveguides and the walls of the fluidic structures are indicated by white lines. For (a) and (b) the color scale indicating the energy density is the same.

We note that real devices do not have in-phase beams due to unequal path lengths and phase errors accumulated by the guided modes. For the 2-waveguide device, this only gives a maximum shift of the interference pattern over a distance of half the period. For the 16-waveguide device, however, 16 random phases of arriving beams lead to a modified and weaker interference pattern with a random structure. This pattern of local hot spots will nevertheless lead to trapping effects similar to those for the ideal pattern resulting from in-phase beams.

### 3.2.2. Detection waveguides and their circuitry

The  $\text{Si}_3\text{N}_4$  detection waveguides are located in a separate wave-guiding layer and serve to collect light scattered by the trapped particle, whether it is Raman scattered light or light of another origin. In the design, we optimize the efficiency of the waveguides to collect scattered light. The input facets of the waveguides are located at the circumference of the microbath, so as to realize maximum coverage of the circum-

ference with multiple waveguides. We arrive at a maximum waveguide width  $w_{\text{det}}$  of  $13.5 \mu\text{m}$ , the actual width varying among the devices. For the different microbaths, the number of waveguides varies between two and ten. For the waveguide thickness we choose the maximum value of  $200 \text{ nm}$ , which is determined by the maximum tolerable film stress for the deposition process of  $\text{Si}_3\text{N}_4$ . The  $200 \text{ nm}$  thick waveguides are multimode.

Using a minimum bend radius of  $300 \mu\text{m}$  for low bend loss and minimizing overlap with the excitation waveguides for low cross talk, the waveguides are routed towards a chip edge, where these are merged into a single waveguide with a width of  $500 \mu\text{m}$ . The latter waveguide is tapered down to  $105 \mu\text{m}$  towards the chip edge for optimum coupling to a multimode fiber (a Thorlabs FG105UCA fiber, core diameter  $105 \mu\text{m}$ ). The fiber output can be coupled to a spectrometer.

In this work, we concentrate on optical trapping and Raman excitation using the excitation waveguides, while the Raman signals are collected with an objective (see the Experimental section). Actual use of the detection waveguides is left for future work. Their design is reported here for completeness.

### 3.2.3. The microbath

The microbath is a cylindrical volume (compare figure 3.4 (b)) to be filled with sample fluid. Among the devices, the diameter of the cylinder is in the range of  $5\text{--}60 \mu\text{m}$ . For the 2-waveguide device, the microbath is shaped as a linear channel with a rectangular cross section (figure 3.4 (a)). For the microbath we face two issues, namely the entrapment of air bubbles during filling and the quick evaporation of the small volume of sample fluid before use. The first issue is overcome by adding two side channels to the microbath, enabling filling from the end of one of these. For this purpose, one channel is designed wider near its end, using a funnel shape (see figure 3.6 (a) below). The wide side of the funnel measures  $250 \mu\text{m}$  across, a size that is suitable for the thin needle of a syringe. When a droplet is applied to the funnel, capillary forces induce rapid progress of the fluid/air interface towards the microbath. The pinning of the fluid/air interface at sharp edges [11] between the side channel and the microbath is avoided by designing smoothly curved walls at the transition. Thus, the microbath can be reliably filled completely, followed by filling of the other side arm. The filling process can be monitored with a microscope. The second issue is solved by building a macrobath on top of the microbath using an image spacer to enable a significant increase of the volume of sample fluid. See subsection on fabrication below.

## 3.3. Experimental

### 3.3.1. Fabrication of the multi-waveguide devices

The devices were fabricated based on the designs and the simulations described in the preceding section. In figure 3.5, we show the main fabrication steps, which are performed on a batch of  $100 \text{ mm}$  silicon wafers. The overall design comprises 30 chips of size  $11 \text{ mm} \times 11 \text{ mm}$ . 28 chips each have a single trapping/ Raman device, with up to 32 excitation and up to 10 detection waveguides. The remaining chips have control structures.

The first fabrication step is the wet thermal oxidation of Si at  $1150^\circ\text{C}$  to obtain an  $8 \mu\text{m}$  thick layer of  $\text{SiO}_2$  (figure 3.5 (a)). This layer serves as the bottom cladding for

the excitation waveguides. Its thickness is chosen such that the 785 nm light within the excitation waveguides is completely decoupled from the silicon substrate.

Then, a 100 nm thick layer of  $\text{Si}_3\text{N}_4$  is deposited using low pressure chemical vapor deposition (LPCVD, figure 3.5 (b)). This layer is patterned using optical lithography and reactive ion etching (RIE) in a fluorine-based plasma, which is followed by resist stripping (figure 3.5 (c)). The resulting 1  $\mu\text{m}$  wide excitation waveguides and the related circuitry have low propagation loss ( $\approx -0.5 \text{ dBcm}^{-1}$  for the straight sections). One waveguide (the input waveguide) starts at the chip edge and is split into  $N$  waveguides using  $(N - 1)$  50/50 Y-splitters. The  $N$  waveguides are routed to point radially towards the position that becomes the device center, similar to the example in figure 3.4 (b). For multiple waveguides ( $N > 2$ ), the overall waveguide circuitry resembles a flower as can be seen in figure 3.6 (d) below.

In this stage, the input waveguide is adiabatically tapered down along a length of 1000  $\mu\text{m}$  to a thickness of 35 nm at the chip edge for optimum fiber-to-waveguide coupling using a special tapering procedure. This step is illustrated in figure 3.5d. Here, the solid part of the waveguide is 35 nm thick, while the dashed part indicates its regular 100 nm thickness away from the edge.

In the next step, a 3  $\mu\text{m}$  thick layer of  $\text{SiO}_2$  is deposited using LPCVD (figure 3.5 (e)). This layer acts as an upper cladding of the excitation waveguides and separates these from the waveguiding layer that follows. For simplicity, we do not show the surface topography resulting after LPCVD due to waveguides already present.

Subsequently, 200 nm of  $\text{Si}_3\text{N}_4$  is deposited using the same LPCVD process as for the excitation waveguides (figure 3.5 (f)). Using lithography, RIE and resist stripping, we produce multiple detection waveguides in this layer fanning out from the central device region (figure 3.5 (g)). The detection waveguides are routed away from the center as a waveguide array and at the chip edge are merged into a multimode waveguide suitable for coupling to a multimode fiber. A thickness of 200 nm is appropriate for the  $\text{Si}_3\text{N}_4$  layer, since it is just below the critical thickness that results in layer cracking due to stress after deposition.

Then, a 3  $\mu\text{m}$  thick layer of  $\text{SiO}_2$  is deposited by LPCVD, which acts as the top cladding for the detection waveguides and as a protection layer (figure 3.5 (h)). The final in-line step is the etching of the cylindrical microbath centered at each chip (compare figure 3.4b) using deep reactive ion etching (DRIE). This is a critical step, since the etch goes 14.3  $\mu\text{m}$  deep down to the substrate, through all the device layers, including the waveguide circuitry at two levels. The etch is highly anisotropic and produces smooth walls of the microbath and thus smooth waveguide facets. For this step, we use a double layer resist (hard mask/photoresist) for good dimensional control and high etch resistance. For most devices, to facilitate filling, the microbath has side channels (see subsection on the microbath), which are etched simultaneously with the microbath. After dicing of the wafer, a millimeter-scale macrobath is created on each chip by placing a 100  $\mu\text{m}$  thick imaging spacer (Biolink Relink 1300) with a 4.0 mm hole. The adhesion strength of the top and bottom surface of the image spacer are different. The weaker adhesive is affixed to the chip to enable its residue-free removal, facilitating device reusability. The stronger adhesive is used to seal the macrobath, which serves as supply volume for the microbath. The sample fluid is then introduced such that after filling a convex meniscus bulges out above the macrobath.

Finally, the sample volume is sealed with a 150  $\mu\text{m}$  thick coverslip by pushing it onto the sticky imaging spacer, thus reaching the stage shown in figure 3.5 (i). Owing to the meniscus, fluid evaporation is not fast enough to cause air inclusion under the coverslip during sealing.

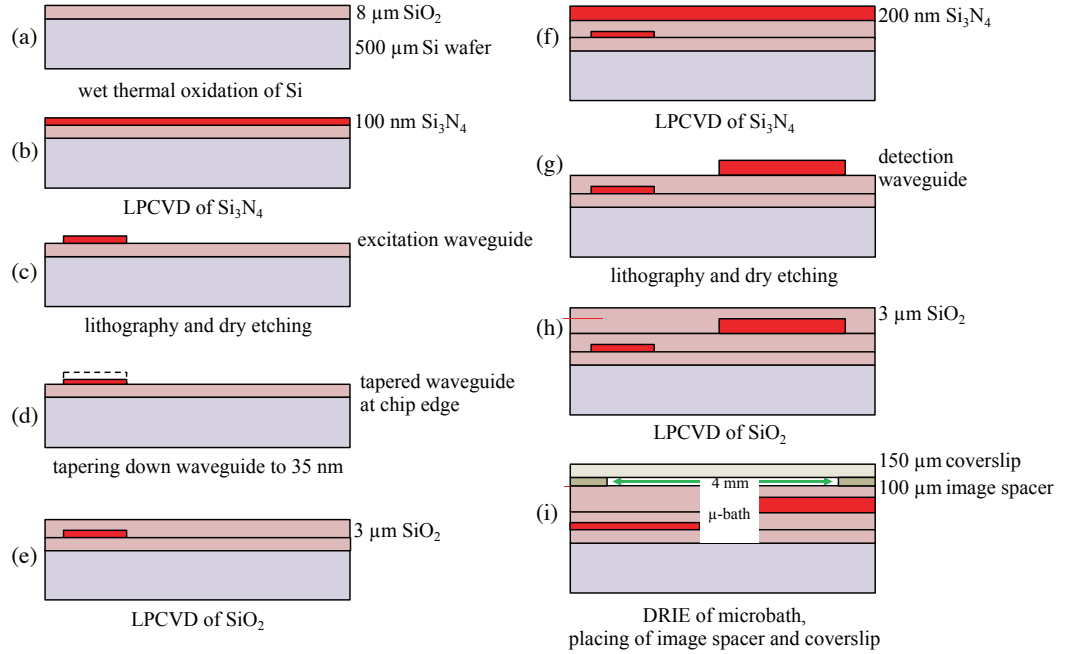


Figure 3.5: Main steps of the fabrication process of the multi-waveguide trapping and Raman devices based on  $\text{Si}_3\text{N}_4$  waveguides. Under each cross section the step is mentioned. The cross section of step d) is at the chip edge, where the waveguide reaches a thickness of 35 nm as a result of the tapering down. For reference, the original waveguide thickness of 100 nm is indicated in d) as well (dashed part). In step i), the side channels of the microbath, etched using the same deep reactive ion etching (DRIE) procedure, have been omitted. The thickness of the various layers does not reflect the real situation. The surface topography resulting from the conformal deposition on the etched structures has been omitted in the cross sections.

In figure 3.6, we give an impression of the final fabrication result for a 16-waveguide device. The device overview is presented in figure 3.6 (a), where the microbath, the side channels, the funnel and the four detection waveguides can be seen. Figure 3.6 (b) shows the magnified area indicated by dashed lines in figure 3.6 (a). Here, the 16 narrow excitation waveguides are also clearly discernible. The four detection waveguides occupy a maximum space along the sides of the microbath for optimum collection efficiency. The scanning electron microscope (SEM) image in figure 3.6 (c) shows the topography of the microbath and the side channels. The DRIE process of these structures is seen to be highly anisotropic, while giving smooth sidewalls. The facets of the excitation and detection waveguides are part of the cylindrical walls of the microbath and cannot be seen here. The surface adjacent to the microbath and the side chan-

nels is slightly angled. This feature occurs, because this device is made from a dummy wafer, for which we only used photoresist as the masking layer during the DRIE process. The actual devices used for the experiments do not have this feature, since in their fabrication, we applied the double layer resist described above. Figure 3.6 (d) is a camera image of the 16-waveguide device actuated by 785 nm laser light. As a result of light scattering, both the excitation and the detection waveguides light up. A further indication of the operation of the detection waveguide is the bright spot at the chip edge indicated with the number 5.

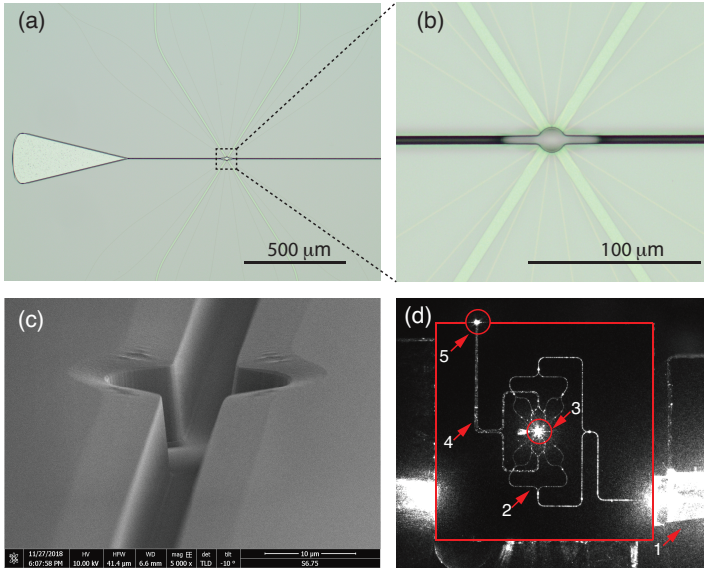


Figure 3.6: (a) Optical microscope image of a device with 16 excitation and 4 detection waveguides. (b) Magnification of the marked area in (a), clearly showing the 16 excitation waveguides and the 4 detection waveguides. (c) Scanning electron microscope image of the device, showing the 15  $\mu\text{m}$  diameter central microbath with the 5  $\mu\text{m}$  wide side channels. (d) Camera image of the 16-waveguide device actuated with light from the input fiber, which is embedded in a fiber array unit (FAU). The various structures light up as a result of light scattering, giving bright saturation of the camera. The red square indicates the chip edges. 1: FAU. The large saturation region results from scattering loss at the input waveguide. 2: Excitation-waveguide circuitry. 3: Microbath with the central trapping region. 4: Detection-waveguide circuitry. 5: Bright spot resulting from scattering of 785 nm light, coupled out from the multimode waveguide connected to the detection waveguides. The detection waveguides collect this light from the microbath at their facets, as a result of direct illumination and scattering.

### 3.3.2. Experimental setup and sample preparation

The experimental setup is based on a Sacher 785 nm laser (Sacher TEC-420). From the primary laser beam, two beams are formed using a 50/50 beam splitter. Each beam is coupled into a single-mode polarisation maintaining fiber. The first of these fibers is butt-coupled to the input waveguide of the chip using a fiber array unit (FAU) glued to its end. The chip is mounted on a sample holder. The FAU is aligned using manual translation stages for coarse alignment and piezoelectric stages for fine alignment. The polarization of the light coupled out by the fiber is perpendicular to the plane of the chip. We optimize the fiber-to-waveguide coupling by maximizing

the lighting up of the waveguide circuitry. This lighting up results from scattering of the propagating waveguide modes and can be monitored using an air objective and a camera mountable above the chip.

The light coupled out by the second fiber is collimated to a free space beam and expanded to properly overfill the objective (Olympus water immersion objective, 60×/1.2 NA) of a home- built LTRS setup. This objective can be placed just above the coverslip on the chip. Using the tweezers functionality of the LTRS, a particle (we use polystyrene beads; see below) can be grabbed from the fluidic volume, transported and then be handed over to a multi-waveguide trap. This transport is actually carried out by translating the main stage, on which the assembly with the sample holder and the small stages are mounted, while the LTRS-trapped particle remains in position. This procedure is very effective in supplying a multi-waveguide trap with a particle. The Raman branch of the LTRS is used for measuring the Raman spectrum of the particle trapped by a multi-waveguide trap. The Raman spectrum is generated by the same on-chip beams that induce the trapping of the bead. Using shutters, we can quickly switch between the tweezers functionality and the chip functionality.

The particles we use for trapping and Raman spectroscopy are polystyrene beads (Nanosphere, ThermoFisher) with diameters of 1 and 3  $\mu\text{m}$ . We prepare bead suspensions with a concentration of about  $10^6 \text{ mL}^{-1}$ . The suspensions are sonicated to obtain a homogeneous bead distribution. The chip is then filled with the sample fluid, as described above in relation to figure 3.5 (i), and is then closed with a coverslip.

### 3.4. Results and Discussion

#### 3.4.1. Optical trapping with a 2-waveguide trap and a 16-waveguide trap

After transporting a bead with the LTRS to a position near the center of a multi-waveguide device, we release the bead and simultaneously actuate the multi-waveguide device. The bead then almost immediately snaps into a near trapping site in the microbath. When the power offered by the fiber,  $P_{\text{fib}}$ , to the chip's input waveguide is high enough, the bead can remain stably trapped in the local trap for tens of minutes. For a 3  $\mu\text{m}$  bead in the 16-waveguide device, this snapping into a local trap is demonstrated in the video of Supporting Information File 1 of [12]. In both the 2-waveguide and 16-waveguide device, there are multiple local traps where a bead can be stably trapped, as demonstrated for a 3  $\mu\text{m}$  bead in the 2-waveguide device in Supporting Information File 2 of [12]. Even more, multiple beads can be stably trapped simultaneously in different local traps, as demonstrated for two 1  $\mu\text{m}$  beads in the 16-waveguide device in Supporting Information File 3 of [12]. We observe trapping events of a 1  $\mu\text{m}$  bead in the 2-waveguide device for  $P_{\text{fib}} = 8 \text{ mW}$ , while in the 16-waveguide device, we already observe trapping for  $P_{\text{fib}} = 1 \text{ mW}$ . For such low powers the bead can hop between local traps. This hopping is visible by eye in the camera image and can be seen for a 3  $\mu\text{m}$  bead in the 2-waveguide device in Supporting Information File 4 of [12]. With increasing  $P_{\text{fib}}$  the local traps becomes stronger, resulting in stronger confinement of the Brownian motion of a bead in the local trapping potential.

For the quantitative characterization of the 2- and 16-waveguide traps, we study the confined Brownian motion of single trapped beads by recording videos, using a high-speed CMOS camera (AV Mako U029, pixel size 4.8  $\mu\text{m}$ ) and by tracking the bead

position as a function of the time in these videos. Each video typically contains about 9000 frames, taken at a frame rate of 541 fps and an exposure time of 1 ms. The videos are recorded for ten values of  $P_{\text{fib}}$ . We track the bead positions using a template matching algorithm [13]. Briefly, we calculate the 2D cross-correlation between an example image of only the bead (taken from one of the frames) and each frame of the video. The maximum in the respective correlation maps indicates the position of the bead. We find the position of the maxima with a resolution of a few nanometers by fitting a 2D parabola to the correlation maps in a limited range near the maximum.

In figure 3.7, examples of 2D histograms of the position of a  $1 \mu\text{m}$  bead obtained from template matching are presented for the 2-waveguide trap (upper row) and the 16-waveguide trap (lower row) and for various values of  $P_{\text{fib}}$ . The left side of the figure shows microscope images of the central part of each device, with the region indicated where the position tracking has been performed. For both traps, the bead is delivered by the laser tweezers close to the central trapping site of the chip.

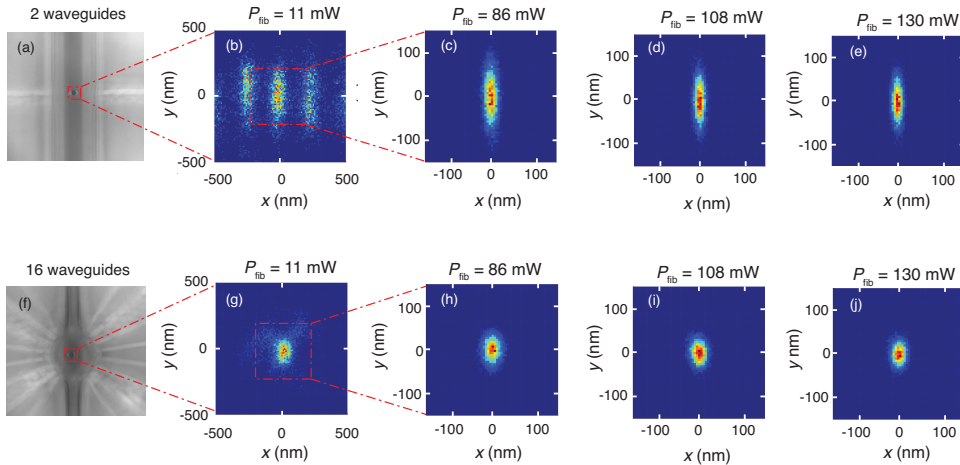


Figure 3.7: (a) and (f) are optical microscope images of the 2-waveguide and 16-waveguide trap, respectively, with a trapped  $1 \mu\text{m}$  polystyrene bead in the center. Further images in the upper (lower) row are histograms of the position of the  $1 \mu\text{m}$  bead in the 2 (16)-waveguide trap, for increasing values of  $P_{\text{fib}}$ .

For the 2-waveguide trap and  $P_{\text{fib}} = 11 \text{ mW}$ , the histogram closely resembles part of the interference pattern of figure 3.4 (a). Thus, the bead is not localized in a single local trap, but hops by thermal stimulation between adjacent local traps. With increasing optical power, the motion of the bead becomes confined to the central local trap, while the excursions from its center become smaller, as seen in figure 3.7 (c–e). This indicates that the trap becomes stronger. The excursions in the  $y$ -direction exceed those in the  $x$ -direction. This corresponds with the shape of the hot spots of the energy density in the 2-waveguide trap shown in figure 3.4 (a). For the 16-waveguide trap, the histograms indicate stable trapping in the central local trap. Again, the bead excursions decrease with increasing power. Also in this case, the bead excursions in the  $y$ -direction exceed those in the  $x$ -direction, but the difference is smaller than for the 2-waveguide trap, in agreement with the shape of the central hot spot shown in

figure 3.4 (b).

Assuming that the traps are harmonic and using the equipartition theorem [13], we may write  $k_B T = k_{x(y)} \sigma_{\Delta x(\Delta y)}^2$ . Here  $k_{x(y)}$  is the trap stiffness for the in-plane directions,  $\sigma_{\Delta x(\Delta y)}$  is the standard deviation of the Gaussian curve describing the 1D histogram reflecting the bead position for these directions,  $k_B$  is the Boltzmann constant and  $T = 293$  K is the temperature. Generally, the proportionalities  $k_{x(y)} \propto P_{\text{trap}}$  and  $\sigma_{\Delta x(\Delta y)}^2 \propto P_{\text{trap}}^{-1}$  are found to hold ( $P_{\text{trap}}$  is the power offered to the trap by the waveguides), in agreement with the above relation. By fitting 2D Gaussian functions to the 2D histograms, we obtain  $\sigma_{\Delta x(\Delta y)}$  and, thus,  $k_{x(y)}$  as a function of  $P_{\text{fib}}$ . In this procedure it is not needed to take into account the small correction of  $\sigma_{\Delta x(\Delta y)}$  due to motion blurring [14], in view of the short integration time of the camera compared to the trap relaxation time.

To obtain plots of  $k_{x(y)}$  as a function of  $P_{\text{trap}}$ , we need to convert  $P_{\text{fib}}$  to  $P_{\text{trap}}$ . For the conversion we use the following approach, taking into account that the 2-waveguide trap has one splitter and the 16-waveguide trap has 15 splitters, arranged in four stages. For the same  $P_{\text{fib}}$  offered to the input waveguide, the expected fiber-to-waveguide loss of  $-0.5$  dB and the loss at each Y-splitter of  $-0.5$  dB (see subsection on fabrication) lead to an estimated ratio of the power offered to the 16-waveguide and the 2-waveguide trap of  $P_{\text{trap},16}/P_{\text{trap},2} \approx 0.7$ . From measurements of the power coupled out vertically from the microbath of either trap due to light scattering in the absence of beads, a power expected to be proportional to  $P_{\text{trap}}$ , we obtain about 0.4 for this ratio. With some bias, we attribute the factor of about 0.6 between the estimated and the measured ratio to the suboptimal fiber-to-chip coupling and other additional losses for the 16-waveguide trap. Thus, we know all transmission factors needed for the conversion of  $P_{\text{fib}}$  to  $P_{\text{trap},2}$  and  $P_{\text{trap},16}$  and can obtain the plots of  $k_{x(y)}$  versus  $P_{\text{trap}}$ , as shown in figure 3.8.

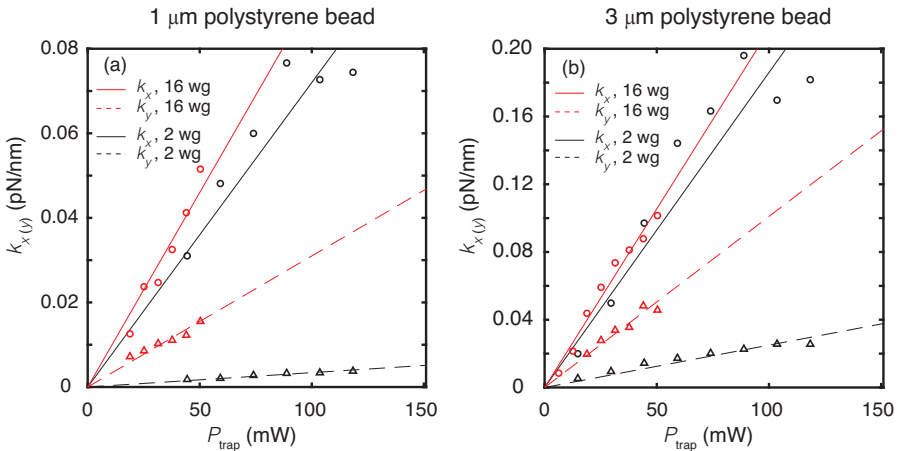


Figure 3.8: Trap stiffnesses  $k_{x(y)}$  as a function of the power  $P_{\text{trap}}$ , represented by empty circles (triangles) and solid (dashed) lines, for the 2-waveguide (black) and 16-waveguide (red) traps, for trapped polystyrene beads of 1 and 3  $\mu\text{m}$  diameter. The lines are linear fits to the data points.

We have limited the number of data points to those  $P_{\text{trap}}$  values for which the bead is

stably trapped in the central local trap of the 2-waveguide trap, i.e., for which hopping between local traps does not occur. Further, in the plots, the maximum value of  $P_{\text{trap},16}$  is lower than the maximum value of  $P_{\text{trap},2}$  as a result of the different conversion factors between  $P_{\text{fib}}$  and  $P_{\text{trap}}$  of the traps. The plots also show linear fits to the data points. On average, the fits describe the data points rather well, although for the 2-waveguide trap, the scatter of the data points  $k_x(P_{\text{trap}})$  is stronger than for the other data points. The finding of linearity agrees with the proportionality  $k_{x(y)} \propto P_{\text{trap}}$ .

The slope of the fits in figure 3.8 yields the normalized experimental trap stiffness  $k_{x(y),\text{exp},n}$  (unit:  $\text{pNnm}^{-1}\text{W}^{-1}$ ), a quantity suitable for comparison. The resulting values of  $k_{x(y),\text{exp},n}$  are compiled in Table 3.1, along with the values of  $k_{x(y),\text{sim},n}$  obtained from the force–distance relations derived from the FDTD simulations of the type we report in [6].

Table 3.1: Normalized experimental and simulated values of the trap stiffness,  $k_{x(y),\text{exp},n}$  and  $k_{x(y),\text{sim},n}$ , respectively, for the 2-waveguide and 16-waveguide trap and for trapped 1 and 3  $\mu\text{m}$  polystyrene beads. All stiffness values are expressed in units of  $\text{pNnm}^{-1}\text{W}^{-1}$ .

Number of waveguides	Bead diameter ( $\mu\text{m}$ )	$k_{x,\text{exp},n}$	$k_{x,\text{sim},n}$	$k_{y,\text{exp},n}$	$k_{y,\text{sim},n}$
2	1	0.72	0.50	0.034	0.024
	3	1.86	1.65	0.25	0.58
16	1	0.92	1.79	0.31	0.17
	3	2.11	2.31	1.01	1.32

The experimental stiffness values in Table 3.1 confirm that the 2-waveguide trap is stiffer in the  $x$ -direction than in the  $y$ -direction. The same holds for the 16-waveguide trap, but the effect is smaller, as already observed visually from the histograms in figure 3.7. Moreover, the experimental stiffness values of the 16-waveguide trap systematically exceed the corresponding values of the 2-waveguide trap, convincingly confirming stronger light concentration in the former case as result of the interference of the 16 beams. The stiffness values for the 3  $\mu\text{m}$  bead exceed the corresponding ones of the 1  $\mu\text{m}$  bead, since a larger volume is subject to the energy density of the optical field, leading to a higher force.

In more detail, defining  $k_{x(y),\text{exp},n}^{16(2)}$  as the normalized experimental stiffness of the 16(2)-waveguide trap, it follows from Table 3.1 that the ratios  $k_{x,\text{exp},n}^{16}/k_{x,\text{exp},n}^2$  and  $k_{y,\text{exp},n}^{16}/k_{y,\text{exp},n}^2$  for the 3  $\mu\text{m}$  bead are smaller than these ratios for the 1  $\mu\text{m}$  bead. This difference of the ratios results from the different character of the energy-density distributions of the 2- and 16-waveguide trap probed by the beads trapped in the center of these traps. The energy-density distributions are characterized by hot stripes (2-waveguide trap) and hot spots and hot partial rings (16-waveguide trap), all typically 295 nm apart (see figure 3.4). Going from 1  $\mu\text{m}$  to the 3  $\mu\text{m}$  bead size in the 2-waveguide trap, the bead probes more hot stripes of equal intensity (see figure 3.4). For the 16-waveguide trap, on the contrary, the bead-size increase leads to probing of more hot partial rings of lower intensity than that of the three central hot spots (see figure 3.4). This results in a smaller increase of the optical force than for the 2-waveguide trap. The simulated stiffness values are close to the experimental

ones, with the average of the ratio  $k_{x(y),\text{exp},n}/k_{x(y),\text{sim},n}$  being 1.05, while the minimum and the maximum of this ratio are 0.43 and 1.82, respectively. We consider this to be in good agreement. Upon bead-size increase, the ratios  $k_{x,\text{sim},n}^{16}/k_{x,\text{sim},n}^2$  and  $k_{y,\text{sim},n}^{16}/k_{y,\text{sim},n}^2$  show similar behavior as the above experimental counterparts, emphasizing agreement of the experimental and simulated results.

The above results for polystyrene beads are promising for extending the experiments to biological particles, which have a lower refractive index contrast with respect to water than polystyrene and are thus harder to trap. Trapping of polystyrene beads already starts for powers of several milliwatts. Thus, we have quite some power left for making the transition to stable trapping of, for example, bacteria, human cells or extracellular vesicles. The 16-waveguide device is the better choice in this respect, since Table 3.1 indicates that it clearly has a higher trap stiffness. Finally, the stiffness values of the 16-waveguide device are similar to those of tightly focused Gaussian beam traps, which are also used for trapping of polystyrene beads. See for example [15]. Since such Gaussian beam traps have also been used for trapping of a wide range of biological particles [2], this is a further indication that the 16-waveguide device can be used for this purpose as well.

### 3.4.2. Raman spectroscopy with the 2-waveguide trap and the 16-waveguide trap

We recorded Raman spectra of trapped polystyrene beads, induced by the beams from the waveguides and collected from the top by the objective of the LTRS. Examples of smoothed Raman spectra (three point moving average) of single 1 and 3  $\mu\text{m}$  beads for the two traps are shown in figure 3.9.

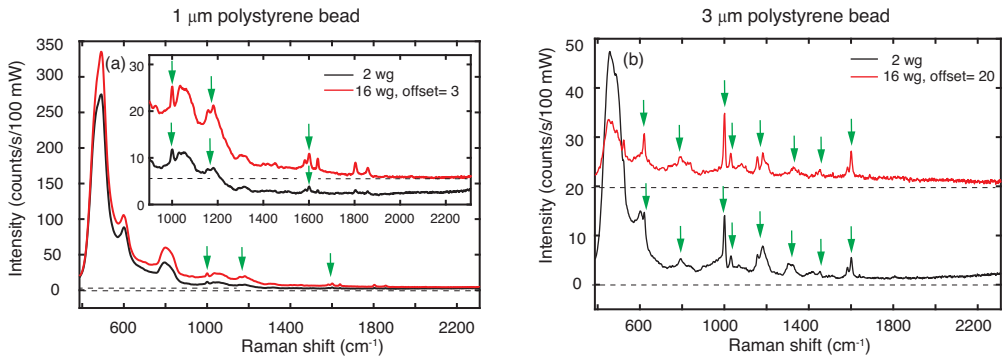


Figure 3.9: Raman spectra obtained with the 2-waveguide (black line) and the 16-waveguide (red line) trap for polystyrene beads with diameters of 1 and 3  $\mu\text{m}$ . For the spectra obtained with the 16-waveguide trap, vertical offsets were applied as indicated in the legend. Each spectrum has its own horizontal axis drawn as a dashed black line. Identified characteristic Raman peaks of polystyrene are denoted by arrows. In (a) the inset is a magnification of a part of the main plot.

To enable a direct comparison of the peak heights, the spectra are normalized to the integration time of 60 s and to  $P_{\text{trap},2}$  and  $P_{\text{trap},16}$  obtained from  $P_{\text{fib}} = 157$  mW. For the conversion of  $P_{\text{fib}}$  to  $P_{\text{trap},2}$ , we had to use a different factor than discussed previously, since in preparing for these Raman experiments, we deduced  $P_{\text{trap},16}/P_{\text{trap},2} \approx 1$  from

the powers coupled out vertically. We attribute the different conversion factor to a lower fiber-to-chip coupling for the 2-waveguide trap.

For either trap, the spectra for both bead sizes show distinct polystyrene Raman peaks [16] (in the figure indicated by arrows), although the spectra for the 3  $\mu\text{m}$  bead are clearly richer. The Raman signals from the 16-waveguide trap are stronger than from the 2-waveguide trap, for both bead sizes. For example, the  $1001\text{ cm}^{-1}$  peak for the 16-waveguide trap for the 1 and 3  $\mu\text{m}$  bead has 76% and 22% more counts, respectively, than for the 2-waveguide trap. The higher percentage for the 1  $\mu\text{m}$  bead than for the 3  $\mu\text{m}$  bead also here results from the different character of the energy-density distributions probed by these beads in the center of the 2- and 16-waveguide trap, as discussed above in relation to the ratio of trap stiffness for the 2- and 16-waveguide trap.

For low wavenumbers, up to about  $900\text{ cm}^{-1}$ , the spectra show a strong background with peaks at 450, 590 and  $800\text{ cm}^{-1}$ . We find that the background also occurs for the empty trap, but then it is much weaker. This indicates that its strength results from scattering of light at the trapped particle towards the objective. Thus, the light leaving the waveguides is the source of the background, implying that the background is generated in the waveguide circuitry. The background is much higher for the 1  $\mu\text{m}$  bead than for the 3  $\mu\text{m}$  bead. We explain this in relation to the Raman collection volume, which has an in-plane diameter of 1  $\mu\text{m}$ , as determined by the 40  $\mu\text{m}$  diameter confocal pinhole. For the 3  $\mu\text{m}$  bead, the Raman collection volume is mainly inside the bead. Therefore, most of the light scattered at the bead surface is not collected by the objective. For the 1  $\mu\text{m}$  bead, the Raman collection volume includes the bead surface, thus leading to a higher contribution to the background. In our future work, we will develop a background-subtraction procedure to recover the Raman signals that are obscured now by the background. We note that background signals of various shapes generated in  $\text{Si}_3\text{N}_4$  waveguides are also observed by other groups in waveguide Raman spectroscopy [17, 18].

### 3.5. Conclusion

We have presented the design, fabrication and performance demonstration of multi-waveguide devices for on-chip optical trapping and Raman spectroscopy of particles in a fluidic environment. The new concept we implement in these integrated photonics devices is that launching of multiple beams ( $>2$ ) from various directions towards the center of the microbath leads to a strong field enhancement in the center and considerably counteracts the unwanted effect of light concentration near the waveguide facets. Thus, a region of preferential trapping is realized around the device center, where several hot spots resulting from interference act as traps for particles in the suspension. Guided by FDTD simulations, we arrive at the proper nanometer-scale thickness for the  $\text{Si}_3\text{N}_4$  excitation waveguides to serve for trapping and Raman generation. FDTD simulations also lead to optimum arrangements of the waveguides around the microbath. Important realized features of these waveguides are optimum thickness for obtaining narrow and weakly diverging beams, small propagation losses, and optimum fiber-to-waveguide coupling for introducing light into the device by tapering down the thickness of the input waveguide near the chip edge. Microfluidic considerations lead to the design of a microbath with side channels for filling with a sample

suspension, a process aided by capillary forces.

Experiments with two example devices, with 2 and 16 excitation waveguides, show clear trapping events for polystyrene beads of 1 and 3  $\mu\text{m}$  diameter and confirm the existence of a configuration of hot spots for preferential trapping near the center of the 15  $\mu\text{m}$  diameter microbath of the 16-waveguide device. Further features are hopping of the bead between adjacent local traps at low optical power and confined Brownian motion at higher power. A detailed study of the confined Brownian motion by tracking the position of the trapped beads in time yields the normalized trap stiffness. In particular, for the 16-waveguide device, the stiffness value is comparable to the values known for tightly focused Gaussian beam traps, which have been used already for trapping of biological microparticles. The experimental values of the normalized stiffness of the 16-waveguide trap are clearly higher than for the 2-waveguide trap.

Raman spectra of the trapped beads, induced by the multiple beams also used for trapping, show clear Raman peaks of polystyrene in spite of a pronounced background present in the low wavenumber range. We argue that the background is already present in the beams emitted by the waveguides and is thus generated in the waveguide material. The different strength of the background found for the two bead sizes suggests that the strength of the measured background results from the interplay of the particle size and the degree of confocal filtering.

The successful optical trapping of polystyrene microparticles and the Raman spectra are promising results, opening up possibilities for on-chip trapping and Raman spectroscopy of biological particles such as bacteria. Making this transition can be challenging, due to the lower refractive index contrast of biological particles with respect to water (thus making these particles harder to trap) and the lower concentration of molecules contributing to Raman peaks.

### 3.6. Acknowledgements

The authors thank H. Heydarian, R.O. Thorson and L. van der Graaf for stimulating discussions and M. Gely for making the SEM images. A.G.J.M. van Leeuwen and G. Wubbels are acknowledged for emphasizing the potential of our multi-waveguide trapping and Raman devices for health and medicine research and water technology.

### 3.7. Funding

The authors acknowledge the Dutch Organization for Scientific Research (NWO) (14197) for funding and NWO Physical Sciences (15316) for making available Supercomputer Cartesius for simulations.

## References

- [1] J.E. Baker, R.P. Badman, and M. D. Wang, "Nanophotonic trapping: precise manipulation and measurement of biomolecular arrays," *Wiley Interdisciplinary Reviews: Nanomedicine and Nanobiotechnology* 10(1): e1477 (2018).
- [2] J. W. Chan, "Recent advances in laser tweezers Raman spectroscopy (LTRS) for label-free analysis of single cells," *J. Biophotonics* 6(1), 36–48 (2013).
- [3] S. Dochow, C. Kraft, U. Neugebauer, T. Bocklitz, et al., "Tumour cell identification

- by means of Raman spectroscopy in combination with optical traps and microfluidic environments," *Lab on a Chip* 11(8): 1484-1490 (2011).
- [4] S. Dochow, M. Becker, R. Spittel, C. Beleites, et al., "Raman-on-chip device and detection fibres with fibre Bragg grating for analysis of solutions and particles," *Lab Chip* 13(6), 1109–1113 (2013).
- [5] M.Boerkamp, T. van Leest, J. Heldens, A. Leinse, et al. , "On-chip optical trapping and Raman spectroscopy using a TripleX dual-waveguide trap," *Opt. Express* 22, 30528-30537 (2014).
- [6] G.B. Loozen, and J. Caro, "On-chip optical trapping of extracellular vesicles using box-shaped composite  $\text{SiO}_2 - \text{Si}_3\text{N}_4$  waveguides," *Opt. Express* 26, 26985-27000 (2018).
- [7] D. Yan, C. Domes, R. Domes, T. Frosch, et al., "Fiber enhanced Raman spectroscopic analysis as a novel method for diagnosis and monitoring of diseases related to hyperbilirubinemia and hyperbiliverdinemia. *Analyst*, 141(21), 6104-6115 (2016).
- [8] S. D. Collins, R. J. Baskin, and D. G. Howitt, "Microinstrument gradient-force optical trap," *Appl. Opt.* 38, 6068-6074 (1999).
- [9] C. G. Roeloffzen, M. Hoekman, E. J. Klein, L. S. Wevers, et al. , "Low-loss  $\text{Si}_3\text{N}_4$  TriPleX optical waveguides: Technology and applications overview," *IEEE journal of selected topics in quantum electronics*, 24(4), 1-21(2018).
- [10] FDTD Solutions; Lumerical Inc.: Vancouver, BC, 2003.
- [11] P. Vulto, S. Podszun, P. Meyer, C. Hermann, et al., "Phaseguides: a paradigm shift in microfluidic priming and emptying," *Lab on a Chip*, 11(9), 1596-1602 (2011).
- [12] G.B. Loozen, A. Karuna, M. M. Fanood, E. Schreuder, et al., "Integrated photonics multi-waveguide devices for optical trapping and Raman spectroscopy: design, fabrication and performance demonstration," *Beilstein journal of nanotechnology*, 11(1), 829-842 (2020).
- [13] I. T. Young, R. Ligteringen, *Stochastic Signal Processing – An Introductory Textbook*(2019).
- [14] W. P. Wong, and K. Halvorsen, "The effect of integration time on fluctuation measurements: calibrating an optical trap in the presence of motion blur," *Opt. Express* 14, 12517-12531 (2006).
- [15] A. C. Richardson, N. Reihani, and L. B. Oddershede, "Combining confocal microscopy with precise force-scope optical tweezers," In *Optical Trapping and Optical Micromanipulation III* (Vol. 6326, p. 632628), International Society for Optics and Photonics (2006, September).
- [16] B. Jasse, R. S. Chao, and J. L. Koenig, "Laser Raman scattering in uniaxially oriented atactic polystyrene," *Journal of Polymer Science: Polymer Physics Edition*, 16(12), 2157-2169 (1978).

- [17] A. Dhakal, P. Wuytens, A. Raza, N. Le Thomas, and R. Baets, "Silicon nitride background in nanophotonic waveguide enhanced Raman spectroscopy," *Materials*, 10(2), 140 (2017).
- [18] N. F. Tyndall, T. H. Stievater, D. A. Kozak, K. Koo, et al., "Waveguide-enhanced Raman spectroscopy of trace chemical warfare agent simulants," *Opt. Lett.* 43, 4803-4806 (2018).

# 4

## Trapping study of *Bacillus subtilis* spores in a 16 waveguide optical trap

*On-chip optical trapping using a dual-waveguide trap has so far been limited to synthetic particles and biological particles, typically larger than 1  $\mu\text{m}$ . For waveguide traps employing more than two waveguides trapping has been demonstrated for synthetic particles only. Here, we take the next step and employ our multi-waveguide trap with 16 waveguides for realizing and characterizing optical trapping of 1  $\mu\text{m}$  sized *Bacillus subtilis* spores. To our knowledge this is the first time optical trapping of biological particles has been demonstrated and extensively studied in a micro-fabricated device employing more than two waveguides. The quality of the optical trap was studied using data from 11 spores at 6 optical powers of light injected into the trap with 30 mW as lowest power values. The confined Brownian motion of the spores at each power value was recorded and analyzed using a particle tracking algorithm based on template matching. The spore-to-spore variations in the extracted experimental trap stiffness values were subsequently correlated to the spore size, and compared to simulated trap stiffness values derived from Finite Difference Time Domain (FDTD) simulations of a core-shell sphere model for the spore refractive index distribution. The influence of random phase deviations between the beams exiting the waveguides was analyzed as well with this simulation approach. The agreement between the measured and simulated trap stiffnesses serve as a verification and validation of the simulation model and point to a generic method for designing multi-waveguide optical traps. Finally, the results from this study show promise for the application of multi-waveguide designs for on-chip optical trapping of biological particles as small as extracellular vesicles.*

### 4.1. Introduction

Integrated photonics based lab-on-a-chip (LOC) techniques attract attention for the development of potent but still easy-to-use and cost-effective diagnostic tools for health-care applications[1][2]. One such application is the manipulation and characterisation of single biological particles identified as potential biomarkers for disease diagnosis, such as extracellular vesicles (EVs) [3]. LOC based optical trapping devices offer novel diagnostic potential by incorporating the strength and control of optical trapping for EV manipulation[4] into a chip building block which can be combined with microfluidic channels for transport and combined with other analytical optical techniques, e.g. Raman spectroscopy, for on-chip EV characterisation.

In previous chapters we have presented the development of our multi-waveguide on-chip optical trap comprising multiple micro-fabricated SiN waveguides which emit coherent counter-propagating beams towards the center of a microfluidic bath. Through constructive interference these result in a highly confined region of optical fields for strong optical trapping. In the first chapter, we developed an extensive simulation model to determine the feasibility and extent of on-chip optical trapping of EVs within a dual-waveguide trap. In the second chapter we demonstrated optical trapping with a micro-fabricated multi-waveguide comprising 16 waveguides which proved to be a stronger optical trap than the dual-waveguide trap. In addition we have demonstrated the feasibility of combined on-chip optical trapping and detectable Raman signal generation within our on-chip traps with polystyrene beads as small as  $1\ \mu\text{m}$ .

In this chapter we take one step forward and demonstrate for the first time on-chip optical trapping of biological particles as small as  $1\ \mu\text{m}$  with our multi-waveguide trap. In this demonstration we employ the 16 waveguide optical trap used in chapter 3 to trap 11 *B. subtilis* bacterial spores with 6 different optical powers. We subsequently followed and recorded their confined Brownian motion in the image plane to then extract experimental trap stiffness values in both the  $x$ -direction and  $y$ -direction. In addition, we carry-out FDTD simulations to numerically study optical trapping of the spores using a core-shell refractive index structure to model the spores. We simulate the fields and forces to then extract simulated trap stiffness values in the  $x$ -direction and  $y$ -direction. In particular, we carry-out a simulation study on the effect of phase errors, accumulated during mode propagation within the waveguide, on optical trap quality. We generate 180 random optical fields within the trap for each of 31 Gaussian distributed random phase distributions with increasing standard deviation value. This enables us to fully determine the correlation between trap quality and phase error magnitude, expressed in terms of spread in optical trapping location and average decrease in optical field energy density and thus trap stiffness. The agreement between trap stiffness values from the simulations and experiments provide immediate verification and validation of the simulation model for predicting and designing optical trapping of both synthetic and biological particles with multi-waveguide traps. It follows that the multi-waveguide shows promise for on-chip trapping of optical trapping for biological particles as small as EVs.

## 4.2. Materials and methods

### 4.2.1. Experimental setup and sample preparation

In this chapter, we use the 16 waveguide device described in chapter 3 to characterize trapping of *B.Subtilis* spores with a multi-waveguide trap. The 16 waveguides employed for optical trapping arise from a single input waveguide which is fanned out with 50/50 Y-splitters in four stages. The waveguides then radially converge towards the center of a cylindrical micro-hole (diameter  $15\ \mu\text{m}$ , depth  $14\ \mu\text{m}$ ) where they end at its walls. The experimental setup used both in this chapter and the previous one is constructed on an optical table and illustrated schematically in figure 4.1.

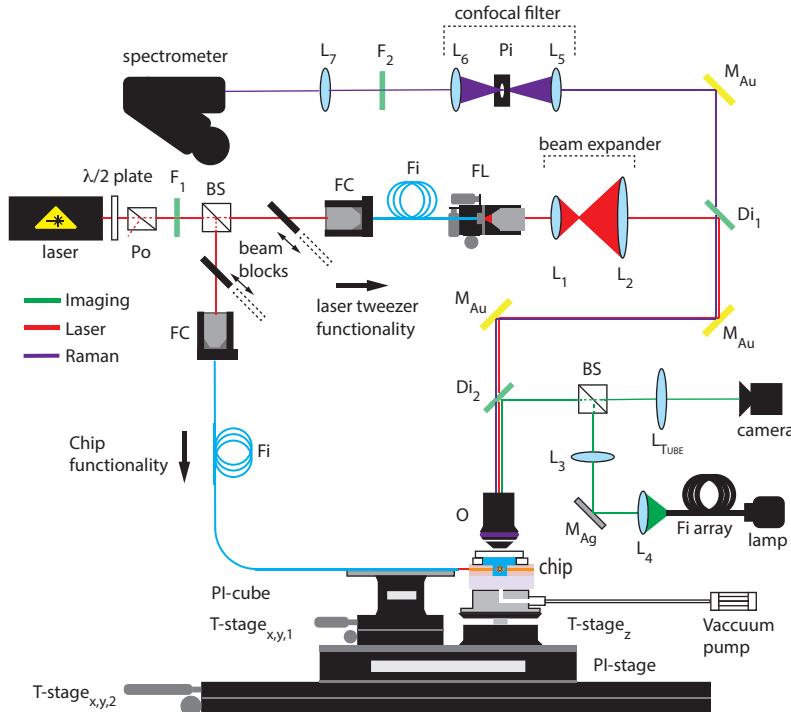


Figure 4.1: The experimental setup with laser branches (red), imaging branch (green) and Raman branch (purple). Components: laser- Sacher TEC-420;  $\lambda/2$  plate; Po- Glan-Taylor polarizer GT10-B; BS- 50:50 beam splitter;  $F_1$ - Clean-up filter Semrock LD01-785/10-12.5; FC- Newport 9131-M fibre coupler; Fi- Polarisation maintaining fiber Thorlabs 780PM-FC; FL- Fiber launcher Thorlabs ;  $L_{1-7}$ - Lenses Thorlabs;  $Di_1$ - Dichroic mirror Semrock LPD02-785Ru;  $M_{Au}$ - Gold mirror Thorlabs PF10-03-M03;  $Di_2$ - Dichroic mirror Semrock Di02-R594; O- objective Olympus UPLSAPO 60XW; PI cube- Piezo cube PI P-611.3 NanoCube XYZ; PI stage- Piezo stage P-561.3CD PI PIMars XYZ Piezo System; T - stage $_{x,y,1}$ - Thorlabs X and Y translation stages; T - stage $_{x,y,2}$ - Translation stage MCL Manual MicroStage XY; T - stage $_z$ - Translation stage Melles Griot Z;  $M_{Ag}$ - Silver mirror Thorlabs PF10-03-P01; Fi array- Fiber array; Lamp- Halogen lamp;  $L_{Tube}$ - Tube lens Olympus SWTLU-C; Camera- AV Mako U029; Pi- Pinhole  $\phi = 40\ \mu\text{m}$ ;  $F_2$ - Filter Semrock LP02-785Re; spectrometer- Acton LS 785; The lens set  $L_{1-2}$  form a beam expander and  $L_5$ , Pi,  $L_6$  form a confocal filter. The beam blocks are mounted in flip mounts, allowing for toggling between chip and laser tweezers functionality.

The setup combines two laser branches for trapping (red) with an imaging branch

(green), and a Raman detection branch (purple). The trapping laser (wavelength  $\lambda = 785 \text{ nm}$ ) is split by a 50:50 beam splitter into a branch for on-chip trapping and a branch for conventional lens-based trapping, the Laser Tweezer (LT)-functionality. Beam blocks are mounted in flip mounts, allowing for toggling between the two trapping modes. The laser light polarization is controlled using a combination of a  $\lambda/2$ -plate and a Glan-Taylor polarizer. A clean-up filter is used for removing residual emission with  $\lambda > 785 \text{ nm}$ . In the LT functionality, the laser light passes through a fiber based spatial filter, a beam expander, two gold mirrors and two dichroic mirrors, and is subsequently focused by the objective lens. The LT functionality is mainly used for initial trapping of the *B.subtillis* spores, which are then transported and transferred to the multi-waveguide trap by translating the chip using translation stages while the objective lens remains fixed. In the chip trapping functionality the laser light is coupled into a single mode polarization maintaining fiber using a laser to fiber coupler. At the other end the fiber is mounted in a fiber array unit (FAU) and butt-coupled to the input waveguide using translation stages in combination with a high resolution  $xyz$  piezo cube, enabling optimum coupling to the fundamental TM mode of the waveguide. The chip is mounted and held in place on a custom made chip holder which also functions as a vacuum chuck.

In the imaging path, Köhler illumination within the region of interest of the object plane is achieved using a halogen lamp, fiber array, mirror and a relay lens-set. The imaging branch is split off from the LT and Raman branches using a dichroic mirror. Raman scattered photons collected by the objective either with on-chip trapping or with the LT mode are guided to the spectrometer via a pair of dichroic mirrors, gold mirrors, a confocal filter, focussing lens and clean-up filter for blocking laser light emitted at wavelengths overlapping with the Raman spectral range. The experiments described in this chapter are focused solely on characterizing optical trapping of *B.Subtillis* spores with the 16 waveguide trap.

The solutions of *B. subtilis* spores (DSM-10-DSMZ) used in the trapping study are prepared first by scraping the spores from a starved culture into demi-water leading to a stock concentration of about  $10^{10}/\text{mL}$ . Then a sample is taken from the stock, diluted to a ratio of 1:1000 and sonicated to obtain a homogeneous spore distribution of about  $10^7/\text{mL}$ . The chip is prepared and infilled with the sample fluid, as described in chapter 3, and is finally sealed with a coverslip.

#### 4.2.2. Trap stiffness measurement

The trapping capabilities of the 16 waveguide device for *B.Subtillis* spores are quantified with trap stiffnesses determined from recorded videos of the confined Brownian motion of single trapped spores, in the same way as for the polystyrene beads in chapter 3. To obtain the trap stiffnesses from the videos, we carry out the data analysis process flow presented in figure 4.2.

The spore and micro-bath positions in each video frame are estimated using the template matching algorithm described in appendix A, taking an image of the spore and micro-bath, respectively, from one of the frames as template. The template matching results in time traces for spore and micro-bath displacement in both  $(x, y)$  image coordinates. Drift and vibrations are accounted for by first subtracting the micro-bath time traces from the corresponding spore time traces. Residual fluctuations in the spore

time trace after subtraction are filtered out using band rejection filters. As observed in chapter 3, the 16 waveguide trap is harmonic, and according to the equipartition theorem, the trap stiffness along the  $x(y)$ -direction follows as  $k_{x(y),\text{exp}} = k_B T / \sigma_{x(y),\text{exp}}^2$ , where  $k_B$  is the Boltzmann constant,  $T = 293 \text{ K}$  is the temperature and  $\sigma_{x(y),\text{exp}}$  is the standard deviation of the spore's confined Brownian motion. The  $x$  and  $y$ -directions are as indicated in figure 3.1. The distribution of spore displacements are represented in 1D histograms using the spore time traces after drift correction and band rejection filtering, each histogram is fit by a Gaussian to determine the standard deviation of the confined Brownian motion  $\sigma_{x(y),\text{exp}}$ .

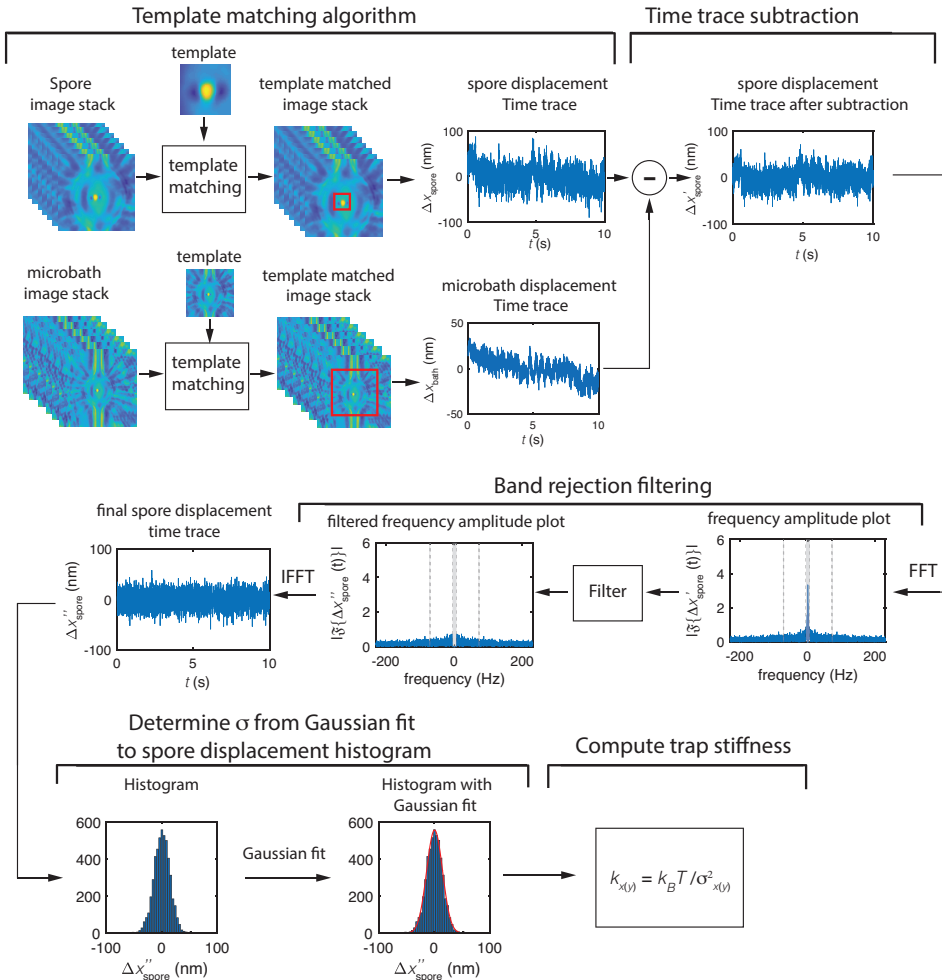


Figure 4.2: Schematic illustration of the data analysis process flow to extract the trap stiffness  $k_{x(y),\text{exp}}$  along the  $x(y)$ -direction from the recorded videos of the confined Brownian motion of the spores. The algorithm includes the template matching procedure, time trace subtraction, band rejection filtering, Gaussian fit to histograms reflecting the spore displacement and computation of  $k_{x(y),\text{exp}}$  using the corresponding values for the standard deviation in the spore Brownian motion,  $\sigma_{x(y),\text{exp}}$ .

The values for the trap stiffnesses  $k_{x(y),\text{exp}}$  are expected to be directly proportional to the combined optical power emitted by the waveguides in the trap,  $P_{\text{trap}}$ , with the constant of proportionality being the normalised trap stiffnesses,  $\bar{k}_{x(y),\text{exp}}$ . To obtain these normalised trap stiffness values, the non-normalised values are first determined for six optical powers offered by the fiber to the input waveguide,  $P_{\text{fib}}$ , and the  $P_{\text{fib}}$  are then converted to  $P_{\text{trap}}$  by taking into account the expected fiber-to-waveguide loss of -0.5 dB and the -0.5 dB loss at each of the four Y-splitter stages in the waveguide circuit. The value for  $\bar{k}_{x(y),\text{exp}}$  is then computed through linear regression between  $k_{x(y),\text{exp}}$  and  $P_{\text{trap}}$ .

#### 4.2.3. Data analysis and simulation

Two factors that may impact the distribution of trap stiffnesses are investigated in detail. These are the heterogeneity of size and shape in the spore sample, and random phase errors between the 16 waveguides of the photonic trap. The first factor is addressed by image analysis of microscopy images acquired with the imaging branch, the second factor by comparison with a simulation study.

The *B. Subtillis* spore sample is not mono-disperse, i.e. there are variations in particle size and shape. The trap stiffnesses are expected to increase with the volume of the spores, as observed with the polystyrene beads in chapter 3. This is investigated by computing the Pearson correlation coefficient between the measured trap stiffnesses and the effective spore sizes for 11 measured spores. The effective spore size is estimated from the microscope images by segmentation using an intensity threshold at an empirical value of 23 % of the maximum image intensity to create a binary image of the spore. The intensity threshold value was determined with the aid of a 1  $\mu\text{m}$  polystyrene bead image, where the intensity threshold of 23 % leads to a correctly sized segmentation of the bead. The image threshold is applied to the microscope image after subtraction of the image baseline and subsequent re-scaling of the image with the maximum image intensity. The spore area is then measured from the binary spore image and finally converted to an effective spore radius  $R_{\text{spore}}$ . In addition, the mean and standard deviation of the measured trap stiffnesses are computed to further assess the stiffness of a typical spore and the heterogeneity of spore shapes within the spore sample.

Finite Difference Time Domain (FDTD) simulations of the electromagnetic fields within the 16 waveguide trap are carried out using the Lumerical FDTD solutions package. The goal of the simulations is to compute the expected normalised trap stiffness of *B. Subtillis* spores for comparison with the experimental values.

The simulation model for the 16 waveguide trap is similar to the model used in chapter 3 and is shown in figure 4.3 together with a bright field image of the actual device. The waveguide thickness and width are 50 nm and 1  $\mu\text{m}$ , respectively, and the refractive indices of silicon nitride, silicon oxide, and water are taken to be  $n_{\text{Si}_3\text{N}_4} = 2.00$ ,  $n_{\text{SiO}_2} = 1.45$  and  $n_{\text{H}_2\text{O}} = 1.33$ , respectively. The microbath is 14  $\mu\text{m}$  deep and has a circular cross-section with a diameter of 15  $\mu\text{m}$ . The fundamental TM mode, with polarisation along the  $z$ -axis, is excited in each waveguide with wavelength  $\lambda = 785$  nm. In the following it is assumed that the polarization in the trapping region is uniform along the  $z$ -axis, so that a scalar approach to computing the electromagnetic energy density inside the trap can be used.

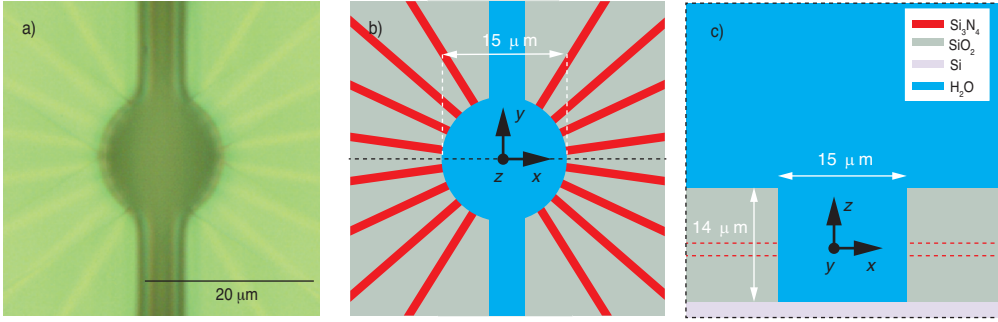


Figure 4.3: (a) Optical microscope image of the 16 waveguide device. The schematic representation of the 16 waveguide trap simulation model seen from (b) the top and (c) the side.

The B.Subtilis spore is a near-spherical biological particle and its refractive index distribution is well known [6–8]. In the simulations the spore is modeled as a core-shell particle, similar to the EVs in chapter 2, with an effective radius  $R_{\text{spore}}$  and a shell thickness  $t_{\text{shell}} = 75\text{nm}$  [8]. The core refractive index is taken to be  $n_{\text{core}} = 1.51$ , and the shell refractive index  $n_{\text{shell}} = 1.39$ . Multiple simulations are carried out in which  $R_{\text{spore}}$  is varied between  $0.40\ \mu\text{m}$  and  $0.65\ \mu\text{m}$  to determine the expected relationship between  $R_{\text{spore}}$  and the simulated normalized trap stiffness  $\bar{k}_{x(y),\text{sim}}$ . This range is chosen to be close to the expected effective spore radius of  $0.50\ \mu\text{m}$ . The normalized trap stiffness values  $\bar{k}_{x(y),\text{sim}}$  are derived from the time averaged normalized optical force,  $\langle \bar{F}_{x(y)} \rangle$ , through the following relationship:

$$\bar{k}_{x(y),\text{sim}} = -\frac{\langle \bar{F}_{x(y)} \rangle}{\Delta x(y)} \quad (4.1)$$

where  $\Delta x(y) = 33\ \text{nm}$  is a small displacement from the trap center along the  $x(y)$ -direction, and  $F_{x(y)}$  is computed using the simulated electromagnetic fields as described in chapter 2. The trapping potential well is at least the size of the spore, around  $0.5\ \mu\text{m}$ , as the spatial variations in the electromagnetic trapping energy landscape are convolved with the spore refractive index profile. For that reason the choice  $\Delta x(y) = 33\ \text{nm}$  is sufficiently small to make the finite difference approximation for the derivative valid. From this point  $\bar{k}_{x(y),\text{sim}}$  is denoted as  $k_{x(y),\text{sim}}$  for simplicity of notation.

In the above described simulations, the 16 beams generating the electromagnetic fields in the trap are all in phase. In the real devices, however, the beams are not expected to be in-phase due to random path length differences between the 16 waveguide branches and phase errors accumulated by the guided modes at e.g. the Y-splitters. The optical force and thus the trap stiffness is directly proportional to the electric field energy within the trap. The impact of phase errors on the trap stiffness is characterized by the global maximum of the electromagnetic field energy in the simulated fields with phase errors,  $U_{\text{PE}}(\mathbf{x})$ , in the trap without spore.

The approach for simulating the fields resulting from phase errors is as follows. First the complex fields arising from the beams emitted by the single waveguides are simulated separately, resulting in 16 complex wave fields  $\vec{E}_j(\mathbf{x})$ , with  $j = 1, 2, \dots, 16$ . These fields are then added with random phase errors  $\phi_j$ , giving a total field,  $\vec{E}_{\text{PE}}(\mathbf{x})$ :

$$\tilde{E}_{\text{PE}}(\mathbf{x}) = \sum_{i=1}^{16} \tilde{E}_i(\mathbf{x}) e^{-i\phi_i} \quad (4.2)$$

The energy density  $U_{E,\text{PE}}(\mathbf{x})$  is computed from  $\tilde{E}_{\text{PE}}(\mathbf{x})$  using:

$$U_{E,\text{PE}}(\mathbf{x}) = \frac{\epsilon_0 n(\mathbf{x})^2 |\tilde{E}_{\text{PE}}(\mathbf{x})|^2}{2} \quad (4.3)$$

where  $\epsilon_0$  is the vacuum permittivity and  $n(\mathbf{x})$  is the refractive index distribution inside the trapping region. To reduce memory requirements,  $U_{\text{PE}}(\mathbf{x})$  is recorded in the  $xy$ -plane,  $xz$ -plane and the  $yz$ -plane as is shown in figure 4.4 for the energy density without phase error,  $U(\mathbf{x})$ , in the central region of the 16 waveguide trap excluding spore (taking  $n(\mathbf{x}) = n_{\text{H}_2\text{O}}$ ).

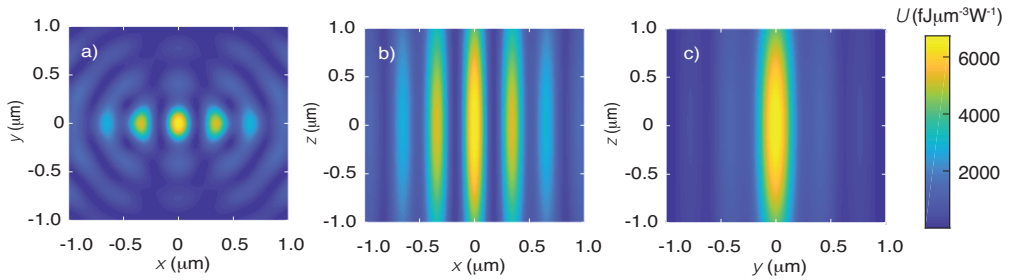


Figure 4.4: The electric field energy density in the 16 waveguide trap excluding spore and without phase errors in the (a)  $xy$ -plane, (b)  $xz$ -plane and (c)  $yz$ -plane. The colors indicate the strength of electric field energy density.

Multiple hot spots are generated as a result of the interference of the beams emitted by the 16 waveguides with random exit phase. In the  $x$ - and  $y$ -directions the characteristic hot spot dimensions are on the order of  $\lambda/(2n_{\text{H}_2\text{O}}) = 295 \text{ nm}$ , while in the  $z$ -direction the hot spot elongation is on the order of a few  $\mu\text{m}$ .

The trap stiffness for a spore with radius  $R_{\text{spore}} = R_{\text{core}} + t_{\text{shell}}$  is proportional to the average of the energy density over the volume of the spore, weighted by the square of the refractive index distribution. For a  $1 \mu\text{m}$  spore, the trap stiffness as a result of the energy density with phase errors is estimated in the  $xy$ -plane ( $z=0$ ) using the energy density in the  $xy$ -plane while assuming a constant field energy density in the  $z$ -direction. This is justified as the size of the spores is typically smaller than the axial elongation of the hot spots. Accordingly, the spore is modeled as a disk with refractive index,  $n_{\text{spore}}(r = \sqrt{x^2 + y^2})$ , averaged along the  $z$ -direction and expressed in polar coordinates as follows:

$$n_{\text{spore}}^2(r) = \begin{cases} n_{\text{core}} \frac{R_{\text{core}} \sqrt{1 - \frac{r^2}{R_{\text{core}}^2}}}{R_{\text{spore}} \sqrt{1 - \frac{r^2}{R_{\text{spore}}^2}}} + n_{\text{shell}} \left( 1 - \frac{R_{\text{core}} \sqrt{1 - \frac{r^2}{R_{\text{core}}^2}}}{R_{\text{spore}} \sqrt{1 - \frac{r^2}{R_{\text{spore}}^2}}} \right) & r \leq R_{\text{core}} \\ n_{\text{shell}} & R_{\text{core}} < r \leq R_{\text{spore}} \end{cases} \quad (4.4)$$

Ultimately, the approximated spore averaged energy density with phase errors,  $U_{E,\text{PE,av}}(x, y)$ , as a function of spore position  $(x, y)$ , is expressed as follows:

$$U_{E,\text{PE,av}}(x, y) = \int_{A_{\text{spore}}} dx dy \frac{1}{2} \epsilon_0 (n_{\text{spore}}^2(x - x', y - y') - n_0^2) |\tilde{E}_{\text{PE}}(x, y)|^2 \quad (4.5)$$

with  $n_{\text{H}_2\text{O}} = 1.33$  the refractive index of water, the fluid in which the spore is immersed. The integral is taken over the projected area of the spore  $A_{\text{spore}} (x^2 + y^2 \leq R_{\text{spore}}^2)$ , and is approximated by a summation over the simulation grid points.  $U_{E,\text{PE,av}}(x, y)$ , denoted as  $U_{\text{PE}}(x, y)$  from now on, is computed for 180 realisations of the random phase errors  $\phi_j$ , sampled from a normal distribution with standard deviation  $\sigma_\phi$ . This computation is executed for  $\sigma_\phi$  from  $\pi/8$  to  $\pi$  with steps of  $\pi/8$ . For each of the 180 computed  $U_{\text{PE}}(x, y)$  and every  $\sigma_\phi$ , we compute the global maximum value of the field energy density  $\text{Max}(U_{\text{PE}}(x, y)) = U_{\text{PE}}(x_{\text{max}}, y_{\text{max}})$  and the corresponding location  $(x_{\text{max}}, y_{\text{max}})$ . With the resulting distribution in  $(x_{\text{max}}, y_{\text{max}})$  we map a region where the spores are most likely to be trapped since the global maximum in the field energy density, corresponding to a minimum in trap potential energy, is the location of the strongest trap, as demonstrated in chapters 2 and 3. In addition, the trap stiffness is directly proportional to  $U_{\text{PE}}(x_{\text{max}}, y_{\text{max}})$ , by the conservative nature of the trapping forces in a trap with counter propagating beams 2 and by virtue of equation 4.1. Assuming that the size/width of the energy density hot spots in the presence of phase errors are comparable in size/width of the hot spot at the trap origin in the absence of phase errors (see figure 4.4), we obtain an estimate of the trap stiffness in the presence of phase errors,  $k_{x(y),\text{sim,PE}}$ , by scaling  $k_{x(y),\text{sim}}$  by  $U_{\text{PE}}(x_{\text{max}}, y_{\text{max}})/U(x_{\text{max}}, y_{\text{max}})$  with  $U(x_{\text{max}}, y_{\text{max}})$  the global maximum in the energy density in the absence of phase errors. The  $k_{x(y),\text{sim}}$  and  $k_{x(y),\text{sim,PE}}$  are then compared with  $k_{x(y),\text{exp}}$  to verify predictability of the trapping behaviour using the simulation models.

### 4.3. Results and discussion

Using the LT functionality, the spores are transported and released at a location near the center of the micro-bath. The chip trap is then actuated and single spores immediately snap into nearby local traps. Single spores are trapped in a local trap for tens of minutes with  $P_{\text{fib}}$  values as low as 26 mW. A time trace for spore confined Brownian motion along  $x$ ,  $\Delta x_{\text{spore}}$ , obtained from template matching is shown in figure 4.5 (a). The time trace exhibits rapid random fluctuations superimposed with a pronounced slow fluctuating component. The corresponding frequency spectrum in figure 4.5 (b) exhibits a major low frequency peak and is flat at higher frequencies, combined with pronounced peaks at 72 Hz. Confined Brownian motion is a Gaussian process and the

corresponding frequency spectrum is expected to be flat with all frequency components containing equal energy [9]. The central peak in figure 4.5 (b) corresponds to the slow fluctuations in the time trace and arise from environmental vibrations which are not damped by the optical table and lead to movement of the chip relative to the objective. The exact origin of the peaks at 72 Hz is unknown but the peaks are attributed to vibrations which are induced by the vacuum pump and coupled to the chip holder through the vacuum tubing. The above mentioned artifacts are present in all spore time traces and lead to broader tails in the histogram of  $\Delta x_{\text{spore}}$ , as shown in figure 4.5 (c), and result in an overestimation of  $\sigma_{x(y),\text{exp}}$  obtained from the Gaussian fit to the histogram, and thus finally to an underestimation of the stiffness  $k_{x(y),\text{exp}}$ .

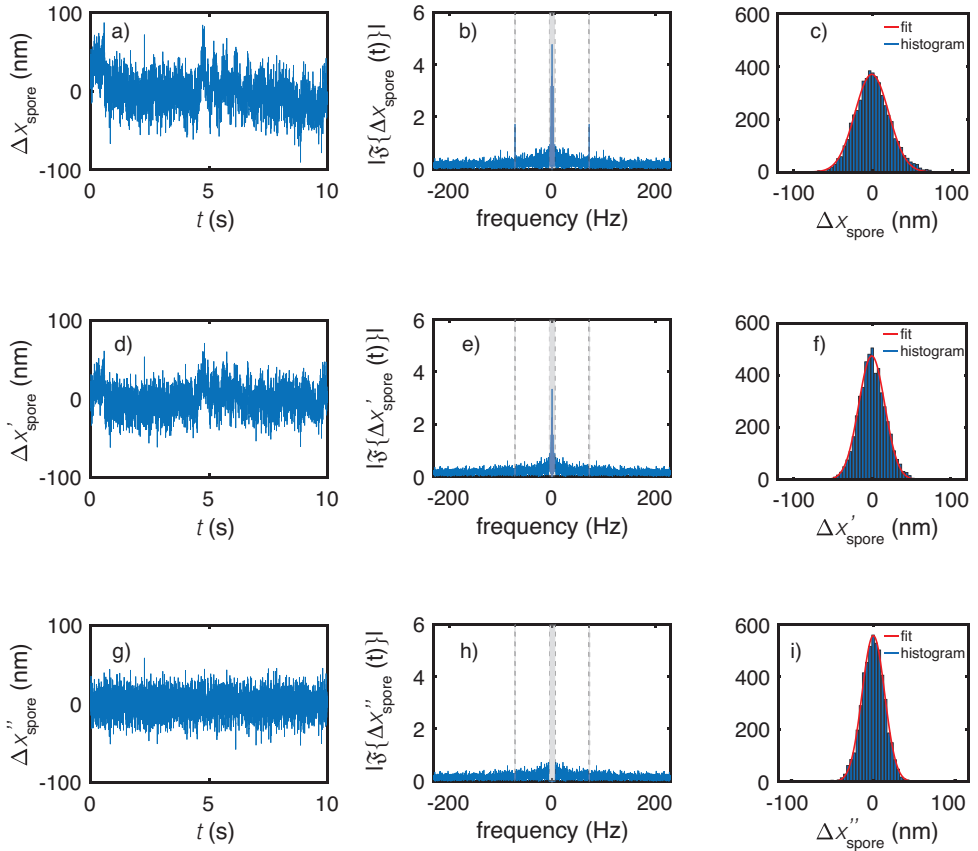


Figure 4.5: (a) Time trace for relative displacement of the spore in the  $x$ -direction,  $\Delta x_{\text{spore}}$ , (b) the corresponding frequency amplitude plot and (c) the histogram of  $\Delta x_{\text{spore}}$ . (d) The time trace after subtraction of the time trace for relative displacement of the microbath in the  $x$ -direction,  $\Delta x'_{\text{spore}}$ , (e) the corresponding frequency amplitude plot and (f) the histogram in  $\Delta x'_{\text{spore}}$ . (g) The time trace for displacement in the  $x$ -direction,  $\Delta x''_{\text{spore}}$  as a result of band-rejection filtering of the grey shaded areas in the frequency amplitude plots, (h) the corresponding frequency amplitude plot and (i) the histogram in the  $x$ -direction,  $\Delta x''_{\text{spore}}$ .

The slow fluctuating component is less pronounced in the time trace  $\Delta x'_{\text{spore}}$  (see figure 4.5 (d) after subtraction with the time trace obtained for the micro-bath movement along  $x$ , as explained in the previous section. Accordingly, the peak height of the 0 Hz peak in the corresponding frequency spectrum (see figure 4.5 (e) is 30 % smaller in amplitude while the peaks at 72 Hz are no longer present. The resulting histogram (see figure 4.5 (f)) has a smaller width than the original  $\Delta x_{\text{spore}}$  histogram (around 21 % smaller full width half maximum (FWHM)). The remaining peak around 0 Hz 4.5 (e)) is filtered out with a band rejection filter and the resulting frequency spectrum shown in figure 4.5 (h) is inverse Fourier transformed to obtain the final time trace for the confined Brownian motion of the spore along  $x$ ,  $\Delta x''_{\text{spore}}$  shown in figure 4.5 (g)). The time trace exhibits random fluctuations around a single equilibrium position, as expected for confined Brownian motion. The histogram corresponding to  $\Delta x''_{\text{spore}}$  has a FWHM that is 29 % smaller than the histogram for  $\Delta x'_{\text{spore}}$ .

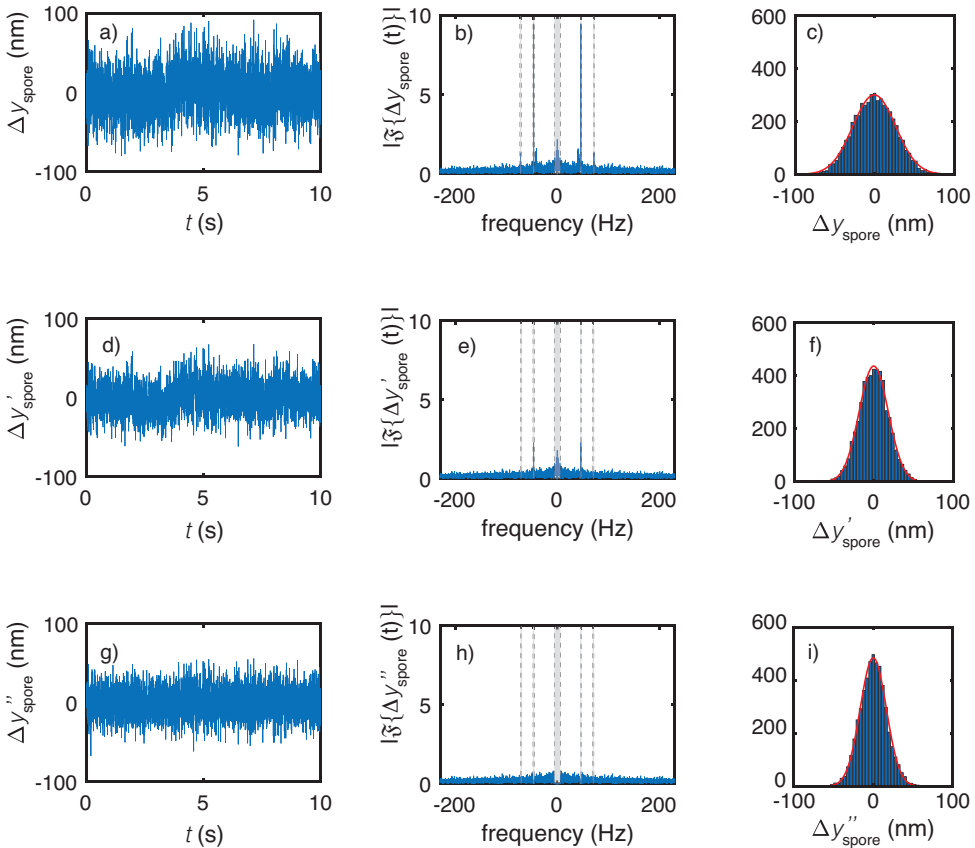


Figure 4.6: (a) Time trace for relative displacement of the spore in the  $y$ -direction,  $\Delta y_{\text{spore}}$ , (b) the corresponding frequency amplitude plot and (c) the histogram of  $\Delta y_{\text{spore}}$ . (d) The time trace after subtraction of the time trace for relative displacement of the microbath in the  $y$ -direction,  $\Delta y'_{\text{spore}}$ , (e) the corresponding frequency amplitude plot and (f) the histogram in  $\Delta y'_{\text{spore}}$ . (g) The time trace for displacement in the  $y$ -direction,  $\Delta y''_{\text{spore}}$  as a result of band-rejection filtering of the grey shaded areas in the frequency amplitude plots, (h) the corresponding frequency amplitude plot and (i) the histogram in the  $y$ -direction,  $\Delta y''_{\text{spore}}$ .

The same procedure is carried out on the time traces of the confined Brownian motion of the spore along  $y$ ,  $\Delta y_{\text{spore}}$  (see example in figure 4.6). The time trace for  $\Delta y_{\text{spore}}$  and its Fourier spectrum shows the same qualitative behaviour as for the  $x$ -direction, but now it appears there are additional rapid fluctuations with a frequency peak at 46 Hz (see figure 4.6 (b)). These peaks are attributed to the overall movement of the micro-bath due to vibrations induced on the chip. Subtracting the time trace for micro-bath movement along  $y$  from the  $\Delta y_{\text{spore}}$  time trace mainly causes a decrease in amplitude of the rapid fluctuations as seen in the  $\Delta y'_{\text{spore}}$  time trace (figure 4.6 (d)). In the corresponding frequency spectrum of  $\Delta y'_{\text{spore}}$  (figure 4.6 (e)) the peaks at 46 Hz are 75 % smaller than the corresponding peaks in the  $\Delta y_{\text{spore}}$  spectra. In addition, the peak height of the 0 Hz peak is reduced by 17 % while the peaks at 72 Hz are completely removed. The  $\Delta y'_{\text{spore}}$  histogram (see figure 4.6 (f)) has a smaller width than the  $\Delta y_{\text{spore}}$  histogram (FWHM reduced with 32 %). The remaining peaks at 0 Hz and 46 Hz are filtered out and the resulting frequency spectrum (see figure 4.6 (h)) is inverse Fourier transformed to obtain the final time trace for the confined Brownian motion of the spore along  $y$ ,  $\Delta y''_{\text{spore}}$  (see figure 4.6 (g)). This time trace consists of random fluctuations centered around a single equilibrium position, as expected of confined Brownian motion. The corresponding  $\Delta y''_{\text{spore}}$  histogram has a 10 % smaller FWHM than the  $\Delta y'_{\text{spore}}$  histogram.

The above time traces, Fourier spectra and histograms serve as examples to illustrate the steps involved in the post-processing chain of the raw time traces obtained from the particle tracking algorithm. These same post-processing steps have been carried out on all spore time traces, which contain similar the noise artifacts as explained above. Full data on all spores are available at [10]

The  $\sigma_{x(y),\text{exp}}$  are determined from Gaussian fits to the  $\Delta x(y)''_{\text{spore}}$  histograms (see red curves in figures 4.5 (i) and 4.6 (i)) for 11 spores and six  $P_{\text{trap}}$  values per spore. The  $k_{x(y),\text{exp}}$  values as function of  $P_{\text{trap}}$  are shown for all spores in figure 4.7 (a-k). These figures indicate the expected linear relationship between  $k_{x(y),\text{exp}}$  and  $P_{\text{trap}}$ . The  $k_{x(y),\text{exp}}$  are obtained from the slopes of linear fits to the  $k_{x(y),\text{exp}}$  data points, and are shown with the bar plot in figure 4.7 (m). The error bars in the  $k_{x(y),\text{exp}}$  bar plots represent the 95 % confidence interval of the linear fits to the data points. The mean and standard error in  $k_{x(y),\text{exp}}$  for 11 spores are shown in figure 4.7 (l). It appears that the  $k_{x,\text{exp}}$  are on average larger than the  $k_{y,\text{exp}}$ , with mean values of 0.71 pN/nm/W and 0.56 pN/nm/W, respectively. This is expected since the multi-beam interference along  $x$  is stronger as discussed in chapter 3, thus leading to a stronger field confinement along  $x$  and larger optical forces. On the other hand, the  $k_{x,\text{exp}}$  vary strongly from spore to spore compared to the  $k_{y,\text{exp}}$ , with 2.6 times larger standard deviation on average.

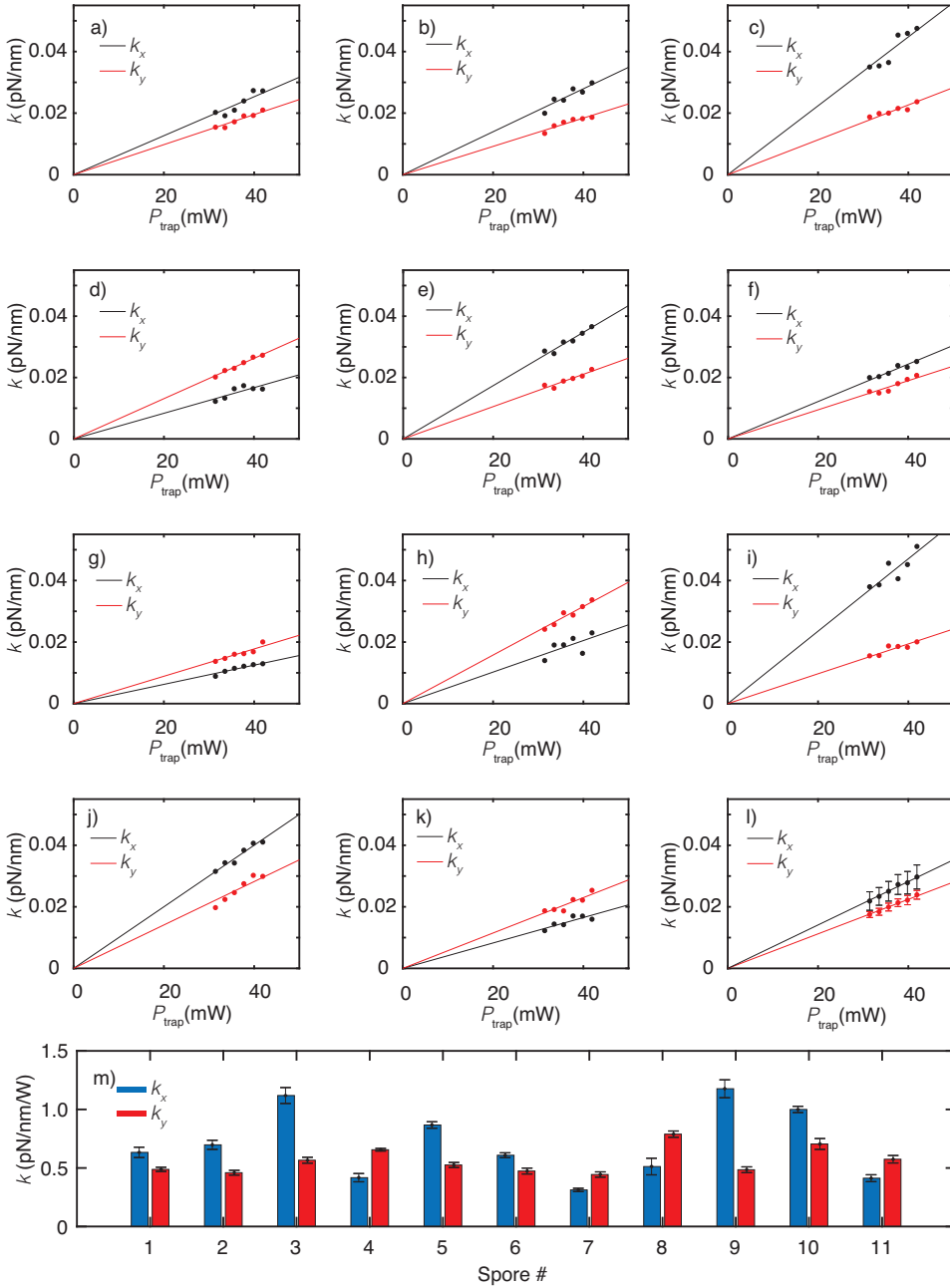


Figure 4.7: Experimentally determined trap stiffnesses along the  $x(y)$ -direction  $k_{x(y),\text{exp}}$  as a function of  $P_{\text{trap}}$ , for the 16 waveguide trap and for trapped *B.Subtilis* spore (a-k) 1 to 11.(l) The mean taken over the 11  $k_{x(y),\text{exp}}$  along with the standard error in the means (represented by the error bars) as a function of  $P_{\text{trap}}$ . The lines in (a-k) are linear fits to the data points and provide (m) the normalised trap stiffnesses  $k_{x(y),\text{exp}}$  represented by the blue(red) bars for the 11 *B.Subtilis* spores along with the 95 % confidence interval of the fit (represented by the error bars)

The observed spore-to-spore variations of  $k_{x(y),\text{exp}}$  are expected to correlate with the spore size. The spore size is estimated in each image by segmenting the bright central spot (as described in the previous section), computing the area of the segmented spot (see results for four of the spore images in figure 4.8 (b-e)), and converting the area to an effective spore radius  $R_{\text{spore}}$ . The  $R_{\text{spore}}$  of each spore is an average computed over 1000 microscope images. The same is done for the 1  $\mu\text{m}$  polystyrene bead, shown in figure 4.8 (a), to determine a conversion factor between the effective radius estimate from the microscope images and the true bead radius,  $R_{\text{bead}}$ . The estimated  $R_{\text{spore}}$  are then scaled with this conversion factor for a more accurate estimate of the  $R_{\text{spore}}$  values, shown in the bar plot of figure 4.8 (f). The effective spore radius values  $R_{\text{spore}}$  obtained in this way fluctuate around 0.49  $\mu\text{m}$  with a standard deviation 0.03  $\mu\text{m}$ . These values agree well with the literature value of  $R_{\text{spore}} \approx 0.5\mu\text{m}$ [6].

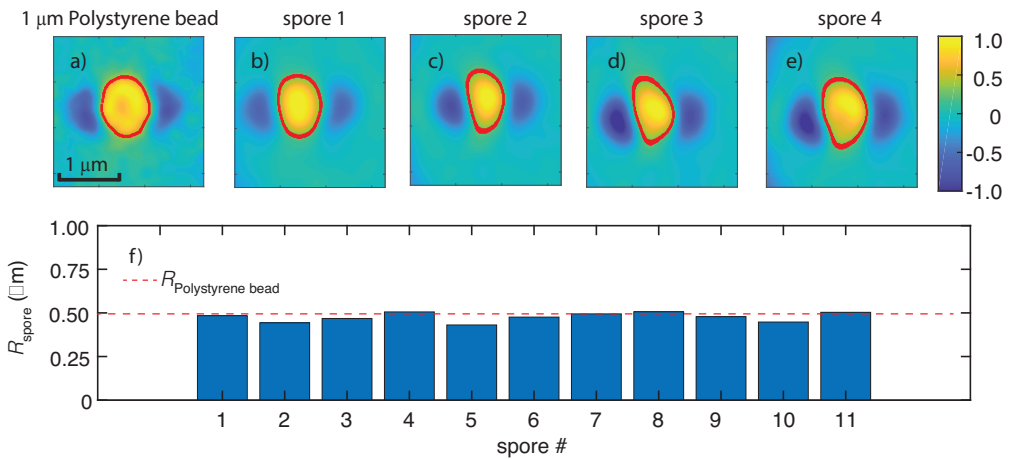


Figure 4.8: Bright field image of (a) a 1  $\mu\text{m}$  polystyrene bead and (b-e) four of the 11 *B.Subtilis* spores trapped within the 16 waveguide trap. An estimated of the bead or spore area is determined from the spore image, indicated by the red contour, is segmented using thresholding. f) Bar plot indicating the estimated effective spore radius  $R_{\text{spore}}$  determined from the segmented area for 11 *B.Subtilis* spores.

The polystyrene bead image and all spore images (figure 4.8) are elliptical and consist of a bright central spot and two dark side lobes, instead of a rotationally symmetric shape consisting of a central spot with outer rings, as expected from normal microscope images. The following tests were carried out on a polystyrene bead in an attempt to clarify the non-symmetric intensity profile of the bead image:

- To exclude imaging aberrations, most importantly astigmatism, a through focus image stack was taken of a trapped polystyrene bead. This was carried out by holding the polystyrene bead in place with the 16 waveguide trap while moving the objective lens along the  $z$ -axis as is illustrated schematically in figure 4.9(a).
- To exclude polarisation dependent effects, a Glan-Taylor polariser was inserted in the imaging branch (see figure 4.1) between the beam-splitter (BS) and tube lens ( $L_{\text{tube}}$ ) and two perpendicularly polarized images were taken of the polystyrene bead trapped with the 16 waveguide trap, as illustrated schematically in figure 4.9(b).

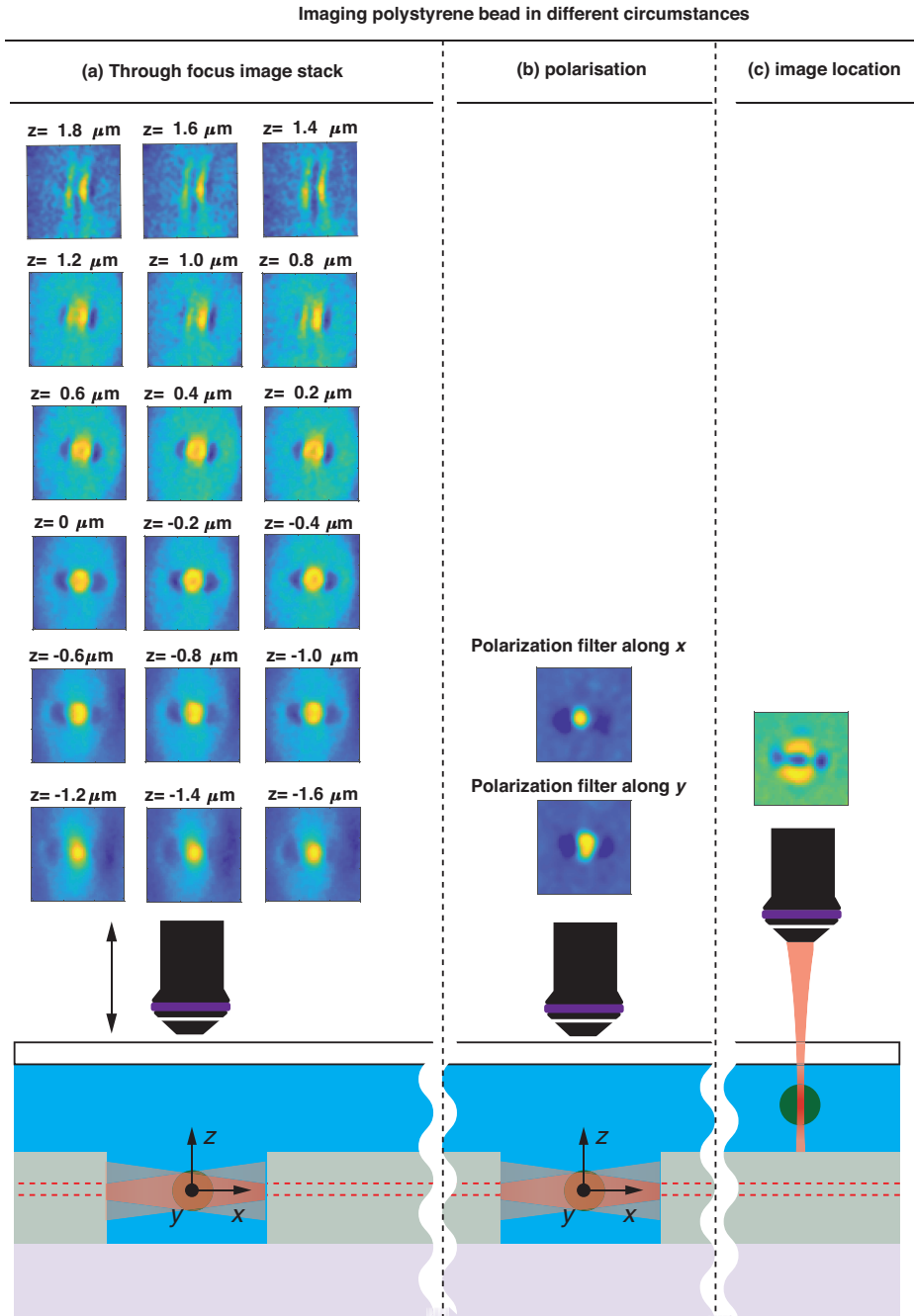


Figure 4.9: Schematic overview of imaging tests carried out with a  $1 \mu\text{m}$  polystyrene bead including (a) A through focus image stack test, (b) polarisation test, (c) imaging location test. The resulting images for each test is shown alongside the schematic overview.

- To exclude contributions caused by secondary reflections from the trap walls, the polystyrene bead is imaged outside the 16 waveguide trap while being held in place with the LTRS, as is shown in figure 4.9(c).

The through focus image stack includes bead images from  $-1.6 \mu\text{m}$  to  $1.8 \mu\text{m}$  along the  $z$ -direction in steps of  $0.2 \mu\text{m}$ , with the focal point at the origin. The results show no indication of astigmatism as the bead image remains elongated along the vertical image direction, instead of flipping to a horizontal elongation on the opposite side of the focal plane. In addition, the image background is correlated to the imaging location along the  $z$ -direction, indicating an influence of the microbath in the bead illumination and thus image formation. This is further confirmed with the bead image taken outside the microbath in figure 4.9(c) in which the bead image intensity values are inverted compared to the images taken within the microbath, as seen in figure 4.9(a). As for the polarisation tests, the two images (see figure 4.9(b)) recorded with perpendicular polarisation configurations of the Glen-Thomson polariser are practically the same, thus implying no correlation between image formation and polarisation. All in all, none of the above described imaging tests provide a clear explanation of the non-symmetric intensity profile in the bead image, which should be further investigated in a follow-up study.

The experimental stiffnesses,  $\bar{k}_{x(y),\text{exp}}$  are shown as a function of  $R_{\text{spore}}$  in figure 4.10. These are compared with the simulated trap stiffnesses with and without the contribution of phase errors,  $k_{x(y),\text{sim}}$  and  $k_{x(y),\text{sim,PE}}$ , respectively.

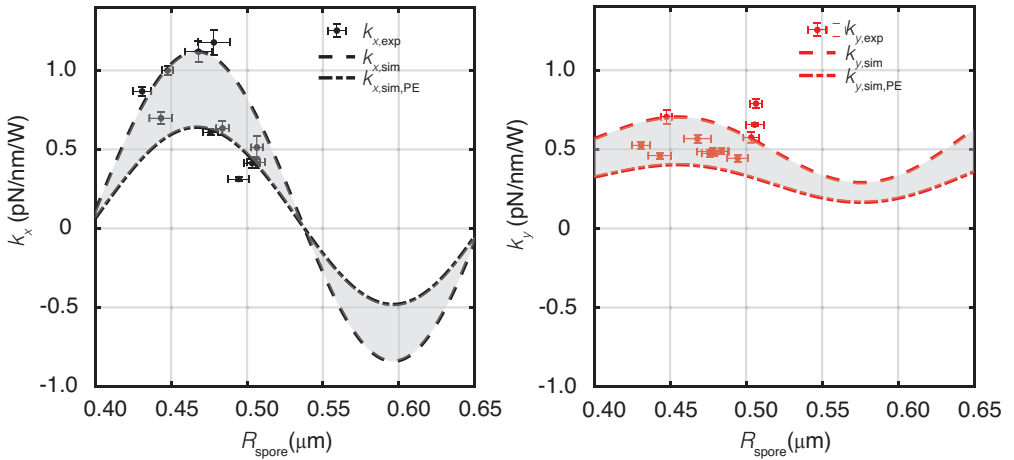


Figure 4.10: The normalised trap stiffness determined from simulations with and without phases error correction obtained from below results,  $k_{x(y),\text{sim}}$  and  $k_{x(y),\text{sim,PE}}$  respectively, and normalised trap stiffness from experiments,  $k_{x(y),\text{exp}}$ , along (a) the  $x$ -direction and (b) the  $y$ -direction as a function of  $R_{\text{spore}}$ . The error bars indicate the standard error in the mean in both the  $k_{x(y),\text{exp}}$  and the  $R_{\text{spore}}$ . The grey shaded area between the  $k_{x(y),\text{sim}}$  and  $k_{x(y),\text{sim,PE}}$  curves indicate the range of expected trap stiffness values.

The  $k_{x,\text{exp(sim)}}$  are correlated with  $R_{\text{spore}}$ . This is expected as the electric field energy density oscillates rapidly compared to the bead size along the  $x$ -direction (see figure 4.4), since the interference is markedly stronger along the  $x$ -direction. As observed

from the simulations, the  $\bar{k}_{x,\text{sim}}$  (and thus  $\bar{F}_x$ ) vs  $R_{\text{spore}}$  oscillate around  $\bar{k}_{x,\text{sim}} = 0$  ( $\bar{F}_x = 0$ ), an effect arising from the competing pulling forces of the hot spots on the bead. This effect is studied and described extensively in chapter 2. Spores with  $R_{\text{spore}}$  where  $k_{x,\text{sim}} < 0$  experience a stronger force from off-center hot spots and are pulled out of the central hot spot, whereas spores with  $R_{\text{spore}}$  leading to  $k_{x,\text{sim}} > 0$  experience a stronger force from the central hot spot and are pulled towards the central hot spot. The  $k_{y,\text{exp(sim)}}$  on the other hand are only weakly correlated with  $R_{\text{spore}}$  since the energy density varies slowly along the  $y$ -direction compared to the spore size. Contrary to  $k_{x,\text{sim}}$ ,  $k_{y,\text{sim}}$  exhibits weak oscillations with  $R_{\text{spore}}$  as the off-center hot spots along the  $y$ -direction are markedly weaker than those along the  $x$ -direction.

Accounting for the random phases at the exit facets of the 16 waveguides leads to a redistribution of the electromagnetic field energy within the trap  $U_{E,\text{PE}}$ , as is clearly shown in figure 4.11.

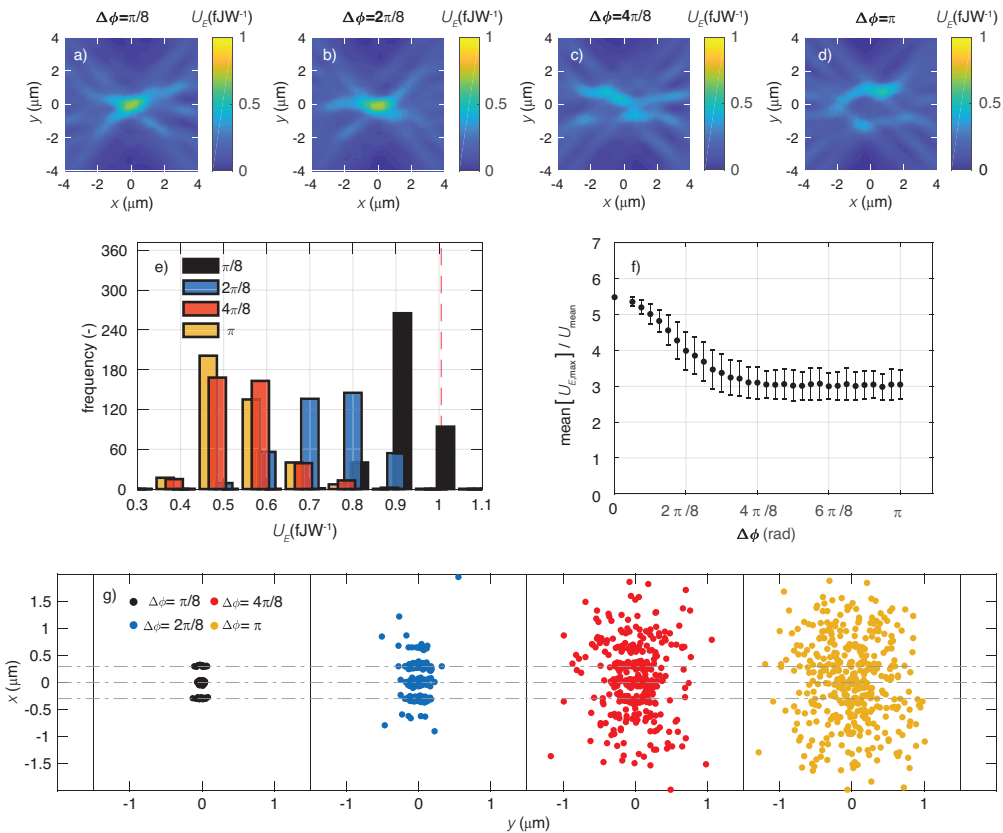


Figure 4.11: The spore averaged electric field energy density,  $U_{E,\text{PE}}$ , in the 16 waveguide trap with phase errors,  $\Delta\phi$ , from (a)  $\pi/8$ , (b)  $2\pi/8$ , (c)  $4\pi/8$  and (d)  $\pi$ . (e) The scatter plots portray the 180 locations  $(x_{\text{max}}, y_{\text{max}})$  of the global maximum electric field energy density,  $(U_{E,\text{PE,max}})$ , for  $\Delta\phi$  values in (a) to (d) while (f) the histograms represent the distribution of 180 global maxima values for the  $\Delta\phi$  shown in (a)-(d). (g) shows the mean in  $(U_{E,\text{PE,max}})$  histograms with corresponding standard deviations for  $\Delta\phi$  from 0 to  $\pi$ .

As  $\sigma_\phi$  increases, the spore averaged field energy is redistributed in the trap transitioning from a standing wave with a clearly defined central focus to a random interference pattern with hot spots (See figures 4.11 (a) to (d) ). This transition is clearly visualised in figure 4.11 (f), which shows the distribution in the location  $(x_{\max}, y_{\max})$  of the global maximum of the field energy density  $U_{E,PE,\max}$  and thus the strongest trapping location. For  $\sigma_\phi < 4\pi/8$  the possible  $(x_{\max}, y_{\max})$  are localised on the interference pattern hot spots. However when  $\sigma_\phi$  increases the  $(x_{\max}, y_{\max})$  gradually redistribute to a random location within a box of approximate size  $2 \mu\text{m} \times 3 \mu\text{m}$  around the origin, which is clearly seen in figure 4.11 (e) for  $\sigma_\phi = 4\pi/8$  and  $\pi$ . In addition,  $U_{PE,\max}$  becomes weaker and transitions from being a single, well-defined value to a distribution of values (See figure 4.11(g)). Between  $\sigma_\phi = 0$  and  $4\pi/8$ , the average  $U_{E,PE,\max}$  gradually drops from 5.5 to 3.05 times the average field energy within the trap  $U_{\text{mean}}$ , which remains constant for all  $\sigma_\phi$  (see figure 4.11(f)), while simultaneously the spread in  $U_{PE,\max}$  increases. For  $\sigma_\phi > 4\pi/8$ , both the average and spread in  $U_{PE,\max}$  remain constant. This is caused by the cyclic nature of the random phasors  $e^{-i\phi_j}$  at the basis of the formation of  $U_{PE}$  as expressed in equations 4.2 and 4.3, which output unique values for  $-\pi < \phi_j < \pi$ . For  $\sigma_\phi < 4\pi/8$ , the distribution in  $\phi_j$  is Gaussian. However as  $\sigma_\phi$  tends to  $4\pi/8$ , the cyclic nature of the phasors converts the  $\phi_j$  distribution to a uniform distribution, and the average and spread in  $U_{PE,\max}$  remain constant.

The intensity distribution inside the trapping region in the limit of large phase errors is reminiscent of a speckle pattern. The ratio of the maximum to the mean energy density  $U_{PE,\max}/U_{\text{mean}}$  may then be estimated with a model in which the light distribution is described by  $N$  statistically independent speckles, where the random intensity of each speckle follows Rayleigh statistics (exponential probability distribution). According to this model (see appendix B for a derivation),  $U_{PE,\max}/U_{\text{mean}}$  is equal to the so-called harmonic number  $H_N = \sum_{n=1}^N (1/n)$ , where  $N$  is the number of speckle patches. Taking the  $2 \mu\text{m} \times 3 \mu\text{m}$  region defined by the  $(x_{\max}, y_{\max})$  realizations and  $\pi(\lambda/2n_{\text{H}_2\text{O}})^2$  as the typical speckle area,  $N$  is estimated to be 86. This leads to  $H_N = 5.04$ , which is within a factor of two of our result of 3.05. We consider this a reasonable result in view of the crudeness of the model. Several effects are not accounted for, such as smearing out of the speckles due to convolution of the optical field with the spore refractive index, and the non-homogeneity of the speckle field where the average speckle intensity decays radially outward from the trap center. Modification of the model with these effects is expected to result in a lower value for  $U_{PE,\max}/U_{\text{mean}}$ , which would be closer to the experimental result.

In actual microfabricated waveguide traps, the randomly accumulated phase in each waveguide arm most likely have a spread  $\sigma_\phi \gg 4\pi/8$ . Causes of phase errors generation include waveguide side wall roughness, non-identical waveguide arm lengths, and microfluidic channel side-wall roughness, which all originate from the limited resolution of fabrication processes and the associated tolerances. According to the above results for the random phases, the actual phase distribution is uniform and  $U_{PE,\max}$  is  $3.05/5.5 \approx 0.55$  times the maximum field energy density in absence of phase errors. The trap stiffness is therefore approximately halved due to the random waveguide phases as is represented by the  $k_{x(y),\text{sim},PE}$  curves in figures 4.10(a) and (b), which are generated by scaling the  $k_{x(y),\text{sim}}$  by 0.55. The  $k_{x(y),\text{sim}}$  and  $k_{x(y),\text{sim},PE}$

show reasonable agreement with the  $k_{x(y),\text{exp}}$  values, both in magnitude, as in the dependency on  $R_{\text{spore}}$ . This result, along with the experimental vs. simulation trapping results in chapter 3, show the validity of the FDTD simulation models developed in chapter 2 to predict optical trapping of both synthetic and biological particles within multi-waveguide traps.

In practice the trapping strength in a multi-waveguide trap is reduced while the trapping location is shifted to a random location near the trap origin. The degree in which these effects occur is depends on the number of waveguides and the complexity of the waveguide circuitry. In a dual-waveguide trap, the trap strength approximately maintained as hot spot constituting  $U_{\text{PE,max}}$  only shifts in the direction of light propagation by  $\lambda/(4n_{\text{H}_2\text{O}}) \approx 150$  nm from the origin at most before being replaced by a neighbouring hot spot. With 16 waveguides, the trap strength is halved on average while the trapping location is shifted to a random location within a 2-3  $\mu\text{m}$  radius from the trap origin. Despite this we were able to stably trap 1  $\mu\text{m}$  B.subtillis spores practically in suspension within a relatively large trap of 15  $\mu\text{m}$  in diameter and  $P_{\text{trap}}$  as low as 30 mW. Stable trapping was also observed at lower powers. This result is a promising first step towards demonstrating the feasibility of stable on-chip trapping of EVs. The trap strength can be further improved by minimizing the accumulated phase errors. On the  $\text{Si}_3\text{N}_4$  platform this can be achieved by adding thermal optical modulators, otherwise known as heaters, to each waveguide and tuning the phase to minimise the resultant phase errors and maximise the collective coherent addition of the light from all waveguides.

#### 4.4. Conclusion

In this chapter we have demonstrated stable on-chip optical trapping of B. subtillis spores in a microfabricated multi-waveguide trap. Optical trapping experiments on 11 B. Subtillis spores were carried-out, where each spore was stably trapped at six optical powers with powers as low as 30 mW in the trap for time intervals on the order of minutes. Stable trapping of spores was even observed for lower powers. While trapped the confined Brownian motion of each trapped spore was recorded, and using a particle tracking algorithm confined Brownian motion time traces were measured. After post processing and analysis these led to trapping stiffnesses that for each spore depend linearly on power, as expected. Simulations with FDTD were carried out of the trap using a core-shell refractive index structured sphere to model the spore. The simulated force exerted on the spore was computed for various spore radii between 0.40 and 0.65  $\mu\text{m}$  and at different  $x$ -location and  $y$ -location close to the origin to then derive the trapping stiffness predictions from the simulated forces.

Special attention was given to the effects of random waveguide phases on the expected trapping performance. The optical field emitted by each waveguide was simulated separately, and then coherently added with a random phase term to model the field in the trap. This enabled the rapid generation of multiple instances of the optical field affected by the random waveguide phases. Using phases randomly sampled from a normal distribution with 32 standard deviation values between 0 and  $\pi$  we showed a clear transition of the field within the trap from a clear focus, to a distorted standing wave pattern to a speckle like interference pattern. Accordingly, the preferential trapping location, defined by the global maximum in the spore averaged field,

transitioned from being located at the origin for  $\sigma_\phi = 0$ , to somewhere on the standing wave fringes for  $0 < \sigma_\phi < 4\pi/8$ , to finally a random location within a  $2 \mu\text{m} \times 3 \mu\text{m}$  region around the origin for  $\sigma_\phi > 4\pi/8$ . The global maximum value in the spore averaged field and accordingly the trapping stiffness steadily decreased by 45% between  $\sigma_\phi = 0$  and  $4\pi/8$  to then remain constant for  $\sigma_\phi > 4\pi/8$ . Using this calculated decrease in stiffness, an estimated phase error affected trapping stiffness was obtained by scaling the simulated trapping stiffness in absence of phase errors. Comparison of the simulation predicted trap stiffnesses, with and without phase errors, with the experimentally determined trap stiffnesses, show reasonably good agreement in both the  $x$  and  $y$ -direction. These results serve as a verification and validation of the simulation models and method used in this chapter and previous chapters to predict the trapping behaviour of both synthetic and biological particles within micro-fabricated waveguide traps.

The trapping results show promise for the employment of micro-fabricated waveguide traps for on chip optical trapping of biological particles down to the size of EVs. In contrast to micro-fabricated dual-waveguide traps employed for trapping biological particles in the past, the multi-waveguide trap generates an intense hot spot of optical field energy near the center of a relatively large trapping volume of up to  $15 \mu\text{m}$  in diameter instead of near the waveguide facets. This shifts the preferential trapping area from near the waveguide facets to the trap center and thus truly in suspension without interference of surface effects of the micro-fluidic channel side walls. A big advantage of the multi-waveguide traps is that the trapping location is relatively far away from any surfaces that can influence the optical trap or the potential detection of a Raman signal. A disadvantage of the multi-waveguide trap are the random exit phases of the waveguide branches which lead to a halving of the optical trapping strength. This disadvantage, however, can probably be circumvented by implementing heaters on the waveguide branches as thermal optic phase modulators to correct for the phase errors.

## References

- [1] A. B. González, and J. Pozo, "The Biophotonics Revolution in Healthcare: Driven by the pilot lines in photonics." *Optik & Photonik* 12(3), 16-17 (2017).
- [2] I. Artundo. "Photonic Integration: New Applications Are Visible: Optical chips allow to miniaturize not only communication components, but also a new generation of life sciences devices," *Optik & Photonik* 12(3), 22-25 (2017).
- [3] L. G. Rikkert, P. Beekman, J. Caro, F. A. W. Coumans, et al., "Cancer-id: Toward identification of cancer by tumor-derived extracellular vesicles in blood," *Frontiers in oncology* 10, 608 (2020).
- [4] P. R. T. Jess, V. Garcés-Chávez, D. Smith, M. Mazilu, et al., "Dual beam fibre trap for Raman microspectroscopy of single cells," *Opt. Express* 14, 5779-5791 (2006).
- [5] S. Yu, J. Lu, V. Giniš, S. Kheifets, et al., "On-chip optical tweezers based on freeform optics," *Optica* 8, 409-414 (2021).
- [6] A. Katz, A. Alimova, M. Xu, P. Gottlieb, et al., "In situ determination of refractive

- index and size of Bacillus spores by light transmission," *Opt. Lett.* 30, 589-591 (2005).
- [7] P. S. Tuminello, E. T. Arakawa, B. N. Khare, J. M. Wrobel, et al., "Optical properties of Bacillus subtilis spores from 0.2 to 2.5  $\mu\text{m}$ ," *Appl. Opt.* 36, 2818-2824 (1997).
- [8] A. Driks, "Bacillus subtilis spore coat," *Microbiol Mol Biol Rev.* 63, 1-20 (1999).
- [9] G. Volpe, G. Volpe, "Simulation of a Brownian particle in an optical trap," *American Journal of Physics* 81, 224-230 (2013).
- [10] G. Loozen, "Confined Brownian motion analysis of 11 B.Subtillis spores trapped within a 16 waveguide optical trap," Zenodo. <https://doi.org/10.5281/zenodo.6345307>, (2022)
- [11] J. W. Goodman, "Speckle phenomena in optics: theory and applications," Roberts and Company Publishers, (2007).



# 5

## Conclusion and outlook

*The feasibility of on-chip optical trapping and Raman spectroscopy of extracellular vesicles using multi-waveguide traps and its applicability for bio-particle detection was studied in this thesis. To this end, we first conducted extensive simulation studies towards the feasibility, capabilities and limits of on-chip optical trapping of EVs using a dual-waveguide trap. We also attempted to improve the on-chip trap strength and Raman signal generation strengths by extending the dual-waveguide trap to multi-waveguide traps. We determined the multi-waveguide trap capabilities through optical trapping of single polystyrene beads and *B. Subtilis* spores and Raman spectroscopy of single polystyrene beads. Here we summarize the results of this work and present an outlook for future research.*

### 5.1. Conclusions

In the introduction, the main research question was divided into three sub-questions, which were separately addressed in the subsequent chapters of this thesis. In this section we summarize the results presented in this thesis and formally answer these sub-questions by reviewing the conclusions of the corresponding chapters. We then address the main overarching research question of this thesis.

**Question 1:** *What are the capabilities and limitations of the dual-waveguide trap for stable on-chip optical trapping of EVs?*

Chapter 2 presents an extensive and detailed numerical study of the trapping capabilities and limitations of the dual-waveguide trap for stable optical trapping of EVs.

Using FDTD simulations with Lumerical, we determined the optical fields arising within dual-waveguide traps, based on box-shaped composite  $\text{SiO}_2$ - $\text{Si}_3\text{N}_4$  waveguides, with and without EVs in the traps. The optical forces exerted on the EVs were then computed using Lumerical's volumetric technique which is based on the Lorentz force density model.

We computed the optical force for EV diameters in the range 50–1000 nm using two refractive index distribution models, viz. homogeneous and that of the realistic core-shell structure, and within three dual-waveguide traps with facet spacings of 5, 10 and 15  $\mu\text{m}$ . The results firstly reveal the conservative nature of the optical forces within traps with counter propagating beams, which leads to a cancellation of the two contributions to the scattering force. The fringe pattern arising from the interference of the counter-propagating beams, contains multiple highly confined hotspots of the optical field which all can function as a separate optical trap, and are shown to strongly contribute to the trapping stability and EV location confinement in the longitudinal direction, especially for smaller EVs. However, the trapping stability of the local hotspots fluctuates strongly with EV size for EVs larger than the characteristic hotspot size of 295 nm. For these EV sizes, multiple hotspots contribute to the resultant force exerted on the EV leading even to cancellation of the local longitudinal forces for certain EV sizes, leaving the global longitudinal force which make for a stable trap but weaker EV confinement. Finally, the EV shell of a mere 5 nm in thickness is shown to contribute considerably to the optical force and thus trap stability for EVs as large as 450 nm.

The conservative nature of the optical forces enable the computation of trapping potentials which lead to the so-called stability curves, which ultimately show the minimum optical power required for stable EV trapping as a function of EV size. These curves indicate that EVs with diameter in a wide range can be stably trapped with the attainable trapping power of 210 mW, down to a smallest size of 115 nm for the 5  $\mu\text{m}$  trap.

The simulation model and computation methods presented in chapter 2 are later verified and validated in chapters 3 and 4 through comparison of simulated trap stiffness values with experimentally determined trap stiffness, thus also confirming the results in chapter 2.

**Question 2:** *Can a micro-fabricated waveguide trap comprising more than two waveguides be realised with improved on-chip optical trapping and Raman signal generation compared with the dual-waveguide trap?*

Chapter 3 presents the full process flow of design, fabrication and functional performance demonstration of multi-waveguide devices for on-chip optical trapping and Raman spectroscopy of particles.

The design was guided by FDTD simulations to arrive at suitable  $\text{Si}_3\text{N}_4$  optical waveguides and waveguide arrangement around a microfluidic bath. The design of the waveguide connecting circuitry for realisation of the optical trap was done in collaboration with LioniX, the foundry responsible for the chip fabrication process, which is described in detail in chapter 3.

The optical trapping and Raman spectroscopy performance demonstration was carried out on 1 and 3  $\mu\text{m}$  diameter polystyrene beads with two device types, a 2 waveguide trap in a wide 15  $\mu\text{m}$  microfluidic channel and a 16 waveguide trap in a 15  $\mu\text{m}$  diameter microfluidic bath. Both device types show clear trapping events of both bead sizes, however for low optical powers the 2 waveguide trap exhibits preferential trapping near the waveguide facets as the bead hops from the center to one of the channel walls. On the other hand, the 16 waveguide trap shows preferential trapping in the center, which is according to design.

The normalized trap stiffness values were determined through a detailed study of the confined Brownian motion by tracking the position of the trapped beads. The resulting normalized stiffness of the 16-waveguide trap are higher than for the 2-waveguide trap. This is particularly visible for the trap stiffness values determined from the 1  $\mu\text{m}$  bead trapping data. In addition to stable trapping, Raman spectra of both beads, induced by the the same light that was used for trapping, was detected. The Raman signals contained distinct polystyrene peaks which were stronger for the 16 waveguide trap. This was again particularly visible for Raman spectra collected from the 1  $\mu\text{m}$  polystyrene bead.

Finally the difference in performance between the 16 waveguide and the 2 waveguide traps, for both the trap stiffness and the Raman signal generation, is shown to increase as the bead size becomes smaller. This is a result of the difference in energy density distribution between the two traps, where the energy density in the case of the 16 waveguide trap is concentrated in a relatively small region in the center of the trap. As a consequence, the difference in performance between the two traps in terms of both trap strength and Raman signal generation is expected to further increase as the particle size decreases towards the characteristic hotspot size (295 nm) of the multi-beam interference pattern formed within the traps.

**Question 3:** *Is on-chip optical trapping and Raman spectroscopy with a multi-waveguide trap feasible for micron sized biological particles?*

As a logical next step chapter 4 provides a detailed on-chip optical trapping study with the 16 waveguide trap on *Bacillus Subtillis* spores, biological particles as large as the 1  $\mu\text{m}$  polystyrene beads studied in chapter 3.

Stable trapping events of 11 *B. Subtillis* spores in multi-waveguide trap were recorded for optical powers as low as 30 mW in the trap and time intervals on the order of minutes. Unrecorded stable trapping events of spores were observed for even lower powers of light in the trap. Analysis of the recorded confined Brownian motion trapped spores with the particle tracking algorithm yielded trap stiffness values that depend

linearly on the optical power, in agreement with expectations. In addition, the experimental trap stiffness values agreed reasonably with values derived from FDTD simulations, which were carried out as explained in chapter 2 with the 16 waveguide trap and a core-shell refractive index model for the spore. These results provide further validation of the simulation models and methods employed throughout this thesis to predict on-chip optical trapping capabilities in multi-waveguide traps for both synthetic and biological particles.

In chapter 4 we also study the effects of random phase errors, accumulated during propagation in the waveguides, on the expected trapping performance. The optical field was shown through simulations to transition from a well defined interference pattern to a speckle-like field distribution, while still maintaining high field concentration and thus preferential trapping near the micro-fluidic bath center. However, the study also indicated an average decrease of the maximum energy density by a factor of two, which is also the expected factor with which the trap strength is expected to weaken.

In spite of the detrimental effects of the phase errors to the optical trap strength of the multi-waveguide trap, the trapping results obtained in chapters 3 and 4 for polystyrene bead and *B. subtilis* spores, respectively, show potential for stable optical trapping of even smaller particles, EVs in particular.

As for Raman spectroscopy, efforts have been made to detect a *B. Subtillis* spore related Raman signal, unfortunately to no avail. Raman acquisition was carried out using the same laser power as for the polystyrene beads in chapter 3 and with integration times ranging up to 10 minutes but this did not result in a distinguishable *B. Subtillis* Raman peak. Reasons for not being able to detect the Raman signal from the spore could be:

1. *Misalignment between the Raman excitation volume and the Raman detection volume.*

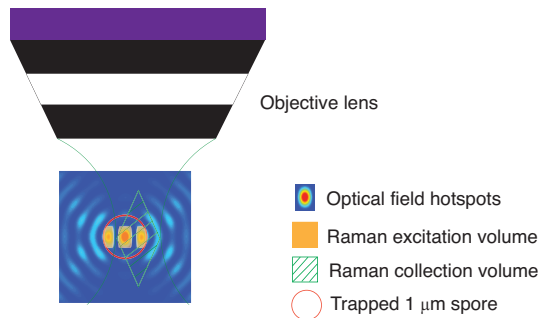


Figure 5.1: Schematic representation of Raman collection scheme in the 16 waveguide trap center while trapping of the EV. The optical field hotspots, Raman excitation volume, Raman collection volume, and trapped 1  $\mu\text{m}$  spore are visualised to scale.

The Raman signal is excited using the light for optical trapping. To be detected at the spectrometer, the Raman light must pass through a confocal microscopy beam path as depicted in figure 4.1 of chapter 4. This then leads to a collection volume in the region which is defined by the objective lens NA, the focal length

of lens L5 used for focusing light into the pinhole, and the confocal pinhole diameter. The light passing through the pinhole originates from a collection volume which is centered around the objective focal point. This Raman collection scheme is schematically depicted in figure 5.1. Maximising the detected Raman signal requires precise alignment of the Raman excitation and collection volumes. Furthermore as inferred from figure 3.9 of chapter 3, detection of polystyrene bead Raman spectra requires an integration time of about a minute at an optical power of 100 mW. As a result, aligning the Raman excitation and collection volumes requires substantial effort, is time consuming and can be prone to error.

2. *Raman signal excitation in a fraction of the Spore.* Only the spore fractions coinciding with intensity hotspot regions in the optical trapping speckle pattern generate a Raman signal, as is also apparent from figure 5.1. In contrast to the homogeneous material nature of the polystyrene beads, a *B. Subtillis* spore comprises multiple material constituents of which the main Raman contribution is from dipicolinic acid chelated with  $\text{Ca}^{2+}$  [1], located mainly in the spore core [2] (Ca-DPA). The Raman signal strength generated from trapped spores is highly dependent on the overlap with the intensity hotspot regions with the spore regions containing Ca-DPA.
3. *Weak Raman yield from B. Subtillis spore.* The Raman yield from *B. Subtillis* spores are at least 6 times lower than for polystyrene, as deduced in ref. [3]. The 16 waveguide trap presented in this research is capable of exciting a Raman signal of about 5 counts per second from a  $1\ \mu\text{m}$  polystyrene bead with 100 mW optical power injected in the trap as is evident from figure 3.9 (a) of chapter 3. In addition the spectra in chapter 3 were collected with an integration time of 60 s to clearly discern the Raman signal from the background noise. The optical power injected via fiber to the chip was 157 mW which converts to 88 mW in the optical trap taking into account -0.5 dB fiber-to-chip coupling transmission and -0.5 dB transmission at each of the Y-splitters. Consequently, detection of similar Raman signal levels from  $1\ \mu\text{m}$  spores in the 16 waveguide trap would require integration times of at least 6 minutes with 157 mW injected from fiber to chip and thus 88 mW injected directly into the trap. As a result, obtaining a Raman spectrum from a spore trapped in the 16 waveguide trap is impractical considering the required integration times, optical powers and the effort to align the Raman detection volume, formed by the objective, and the Raman excitation volume in the spore.

**Main research question:** *Is on chip optical trapping and Raman spectroscopy with multi-waveguide traps a viable technique for high throughput EV diagnosis?*

The optical feasibility study for EVs in a dual-waveguide from chapter 2 combined with the experimental optical trapping results presented in chapters 3 and 4 show promise for on-chip optical trapping of EVs. As shown in chapter 2, on-chip trapping of EVs with diameters of a few hundred nm is feasible with powers around 100 mW. Plausibility of this result is confirmed in chapters 3 and 4, on the one hand

through agreement between simulations and experimental results, and on the other hand through improved optical trapping strengths observed in the 16 waveguide trap as opposed to the 2 waveguide trap. Unfortunately, simultaneous Raman identification of the EVs proves to be significantly challenging, as deduced from the efforts to carry-out on-chip Raman identification of *B. Subtilis* spores. Moreover Raman spectroscopy on an EV in the 16 waveguide trap would require even more effort, as these are typically 3 to 10 times smaller than the *B. Subtilis* spore. Reasonably assuming linear proportionality between Raman signal and volume, the Raman signal strength for EVs is expected to be at least 9 times weaker than for *B. Subtilis* spores. As a result, detectability of a Raman signal from an EV would require integration times of close to an hour.

Consequently, the maximum throughput of the current chip-based laser tweezing Raman spectroscopy device is expected to be on the order of at most one EV per hour making this device unsuited for practical applications where throughputs of millions per second are required.

## 5.2. Outlook

This final section provides an outlook to further research aimed at tackling the problem of on-chip biochemical characterisation of EVs, in particular employing optical diagnostic techniques allowing for high throughput. In addition, this technique must be compatible with on-chip photonic integration and scale-up to fully exploit the advantages of lab-on-a-chip based diagnostics.

Based on the results detailed in the conclusion section on on-chip spontaneous Raman spectroscopy, a number of approaches can be followed for optical chemical characterisation of EVs. These include enhancing the induced Raman signal or incorporating other optical techniques such as Rayleigh scattering or fluorescence with on-chip trapping and a Raman spectroscopy scheme.

A straightforward method to enhance the Raman signal is through coherent anti-stokes Raman scattering (CARS), which also enables label free spectral finger printing [4]. This technique requires two picosecond pulsed lasers, one of these being tunable over a bandwidth of 100 nm. In addition, the complexity of this technique makes short term on-chip integration challenging. An attractive alternative for signal enhancement is surface enhanced Raman spectroscopy (SERS), which is based on the enhancement of the electromagnetic field with plasmons that are excited at metallic surfaces composed typically of gold (Au) and/or silver (Ag) [5, 6]. This electromagnetic field enhancement can give rise to Raman signal amplification with several orders of magnitude. A drawback is that the enhancement only occurs in close proximity to a conductive surface which can lead to surface adhesion effects interfering with the optical trapping.

In refs. [7, 8], SERS of EVs has been demonstrated by functionalizing single EV surfaces with synthesised silver coated gold nanoparticles, AuNP, silver coated gold nanoparticles, Au@AgNP, and effectively encapsulating single EVs with irregularly shaped Au@Ag nano-shells. Upon illumination with a focussed laser beam at 785 nm, local surface plasmons were excited in the Au@Ag, leading to strong enhancement of the field between 0 and 7 nm from the Au@Ag surface. This region of field enhancement corresponded with the EV membrane and led to SERS signal from the EV membrane

content with just 15 mW of optical power and 0.5 s of integration time. Previous attempts without metallic coating have resulted in no discernable Raman signal from EVs. Assuming applicability of this method to Raman amplification in the multi-waveguide traps, an integration time of 0.5 s per EV would lead to about 2400 EVs per hour. This is assuming 1.0 s transfer time between EVs using a micro-fluidic circuitry employed for EV supply to the optical trap as demonstrated in ref. [9]. In addition, powers as low as 15 mW open up the possibility of including the laser on-chip through hybrid integration of the multi-waveguide circuitry with a semiconductor chip laser, as demonstrated earlier [10, 11].

In the above studies the SERS spectra were collected from AgNP and Au@AgNP coated EVs adsorbed onto a  $\text{CaF}_2$  substrate in a 60  $\mu\text{L}$  droplet. In a single beam optical tweezer setup, the coated EVs would induce enhanced scattering forces due to the plasmonic resonances in the AgNP or Au@AgNP coating. As a result, the enhanced scattering forces will diminish trap stability in a traditional optical tweezer. However, in traps formed by counter propagating beams the scattering forces are practically canceled out, as shown in chapter 2 for the two waveguide trap. Moreover, this has been demonstrated already in ref. [12], where a standing wave optical trap was used to stably trap AuNPs as small as 100 nm. Consequently, the above method for SERS signal generation from EVs combined with the counter-propagating beams generated with the multi-waveguide traps studied in this thesis show promise for on-chip optical trapping and Raman spectroscopy of EVs. On the other hand, compared to spontaneous Raman spectroscopy, this method is no longer label free and thus requires additional sample preparation steps. In addition, plasmonic NPs are highly absorbing and can lead to sample heating. This poses a limitation on the maximum optical power, which is highly dependent on NP composition, size and concentration, and needs to be determined empirically.

Fluorescence detection is a different optical technique with potential for chemical identification of EVs based on their chemical content. Fluorescence signal levels are on the order of 1 million times stronger than those for Raman spectroscopy, which is clearly an inherent advantage for detectability and throughput. Promising results have been reported in the literature for fluorescence-guided identification of EVs [13, 14] particularly in the area of flow cytometry [15, 16]. In recent times, efforts have been made towards the development of on-chip solutions to flow cytometry [17]. These developments suggest an attractive solution in on-chip flow cytometry for EV characterisation. A multi-waveguide opto-fluidic chip is envisioned with a well-designed microfluidic circuit to generate a sheath flow and allowing for sequential passing of single EVs in the optically active region. In this region a single waveguide can be used for sample illumination while two others can then be employed to collect forward scattered light and another for sideways scattered light and fluorescence signal collection, as described in ref. [18]. Separation of the sideways scattered light and fluorescence signals can be achieved using a spectral demultiplexing building block such as an arrayed waveguide grating [19].

Optofluidics chips employing fluorescence signal detection have been reported to exhibit typical throughputs of 500 to 700 particles/s [18, 20], which is an order of magnitude smaller than what is typically observed for standard flow cytometry. The gap in throughput can be bridged by including multiple devices on a single chip and

testing in parallel, which is a particular strength of lab-on-a-chip devices. These reports and considerations indicate the potential that on-chip fluorescence cytometry offers a possible solution for high throughput detection and biochemical characterisation of EVs.

Identification of EVs based solely on above techniques is limited as Raman signals provide a volume averaged chemical fingerprint with response mainly originating from the phospholipid shell, while fluorescence provides only the presence of specific receptor molecules also from the shell. In addition, current gaps in knowledge on EV composition and the presence of contaminant particles in the EV size range, such as lipoproteins and protein aggregates, lead to false EV identification. This problem is approached by simultaneously recording the Rayleigh scattered signal to determine refractive index and particle size along side biochemical content. This has been demonstrated for Raman spectroscopy by measuring the back scattered light [21] and for fluorescence with recording both forward scattered and side scattered light [22]. Another such technique with Rayleigh scattered light is interference contrast imaging, as demonstrated for single viruses in ref. [23]. Here, Rayleigh scattered light from the particle which is combined with light from a reference beam to record an interference pattern. This interference signal is then analyzed to accurately yield particle size of single nanoparticles as small as a few tens of nm. This method can be employed with a fluidic channel for determination of nanoparticles like EVs based diameter with a throughput of 1000/s [24].

In conclusion, feasibility of on-chip bio-chemical characterisation of EVs by means of integrated optical techniques momentarily still requires prior labeling of the EVs. For Raman based characterisation, the throughput is expected to be limited to a few thousand particles per hour, which can possibly be improved with an order of magnitude through parallel characterisation with multiple device blocks on a single lab-on-a-chip. However, techniques based on Raman identification are low in throughput compared to flow cytometric methods, but there is a trade-off between the throughput and the specificity. Nonetheless, both methods are potential candidates for on-chip biochemical characterization of EVs on-chip.

## References

- [1] P. Zhang, P. Setlow, and Y.Q. Li, "Characterization of single heat-activated *Bacillus* spores using laser tweezers Raman spectroscopy," *Opt. Express* 17, 16480-16491 (2009).
- [2] S.S. Huang, D. Chen, P.L. Pelczar, V.R. Vepachedu, et al., "Levels of Ca<sup>2+</sup>-dipicolinic acid in individual *Bacillus* spores determined using microfluidic Raman tweezers," *J. Bacteriol.* 189(13), 4681-4687 (2007).
- [3] P. Zhang, L. Kong, P. Setlow, and Y. Li, "Multiple-trap laser tweezers Raman spectroscopy for simultaneous monitoring of the biological dynamics of multiple individual cells," *Opt. Lett.* 35, 3321-3323 (2010).
- [4] F. El-Diasty, "Coherent anti-Stokes Raman scattering: Spectroscopy and microscopy", *Vibrational Spectroscopy*, 55(1), 1-37 (2011).
- [5] C. Matricardi, C. Hanske, J. L. Garcia-Pomar, J. Langer, A. Mihi, et al. , "Gold

- nanoparticle plasmonic superlattices as surface-enhanced Raman spectroscopy substrates", *ACS Nano* 12(8), 8531-8539 (2018).
- [6] X. Dai, W. Fu, H. Chi, V. S. D. Mesias, H. Zhu, et al., "Optical tweezers-controlled hotspot for sensitive and reproducible surface-enhanced Raman spectroscopy characterization of native protein structures", *Nature communications* 12(1), 1-9 (2021).
- [7] S. Stremersch, M. Marro, B. Pinchasik, P. Baatsen, A. Hendrix, et al., "Identification of Individual Exosome-Like Vesicles by Surface Enhanced Raman Spectroscopy," *Small* 12(24), 3292-3301 (2016).
- [8] J.C. Fraire, S. Stremersch, D. Bouckaert, T. Monteyne, T. De Beer, et al., "Improved Label-Free Identification of Individual Exosome-like Vesicles with Au@Ag Nanoparticles as SERS Substrate", *ACS applied materials & interfaces* 11(43), 39424-39435 (2019).
- [9] S. Dochow, C. Krafft, U. Neugebauer, T. Bocklitz, T. Henkel, et al. , "Tumour cell identification by means of Raman spectroscopy in combination with optical traps and microfluidic environments," *Lab on chip* 11(8), 1484-1490 (2011).
- [10] A.T. Mashayekh, T. Klos, D. Geuzebroek, E. Klein, T. Veenstra, et al., "Silicon nitride PIC-based multi-color laser engines for life science applications," *Optics Express* 29, 8635-8653 (2021).
- [11] N. Lindenmann, G. Balthasar, D. Hillerkuss, R. Schmogrow, M. Jordan, et al., "Photonic wire bonding: a novel concept for chip- scale interconnects," *Opt. Express* 20, 17667-17677 (2012).
- [12] M.Y. Wu<sup>1</sup>, D.X. Ling, L. Ling, W. Li and Y.Q. Li, "Stable optical trapping and sensitive characterization of nanostructures using standing- wave Raman tweezers," *Scientific Reports* 7(1), 1-8 (2017).
- [13] K. Lee, K. Fraser, B. Ghaddar, K. Yang, E. Kim, et al. , "Multiplexed Profiling of Single Extracellular Vesicles," *ACS Nano* 12(1), 494-503 (2018).
- [14] A. Nanou, F.A. Coumans, G. van Dalum, L.L. Zeune, D. Dolling, et al. , "Circulating tumor cells, tumor-derived extracellular vesicles and plasma cytokeratins in castration-resistant prostate cancer patients," *Oncotarget* 9(1), 19283-19293 (2018).
- [15] Y. Tian, L. Ma, M. Gong, G. Su, S. Zhu, et al., "Protein Profiling and Sizing of Extracellular Vesicles from Colorectal Cancer Patients via Flow Cytometry," *ACS Nano* 12(1), 671-680 (2018).
- [16] L.G. Rikkert, L. De Rond, A. Van Dam, T.G. Van Leeuwen, F.A. Coumans, et al., "Detection of extracellular vesicles in plasma and urine of prostate cancer patients by flow cytometry and surface plasmon resonance imaging," *PLoS One* 15(6), e0233443 (2020).

- [17] R.J. Yang, F. Lung-Ming, and H.H. Hou, "Review and perspectives on microfluidic flow cytometers," *Sensors and Actuators B: Chemical* 266, 26-45 (2018).
- [18] X. Mao, A. A. Nawaz, S.S. Lin, M.I. Lapsley, Y. Zhao, et al., "An integrated, multiparametric flow cytometry chip using "microfluidic drifting" based three-dimensional hydrodynamic focusing," *Biomicrofluidics* 6(2), 024113 (2012).
- [19] Z. Hu, A. Glidle, C.N. Ironside, M. Sorel, M.J. Strain, "Integrated microspectrometer for fluorescence based analysis in a microfluidic format," *Lab chip* 12, 2850-2857 (2012).
- [20] Y.C. Tung, M. Zhang, C.T. Lin, K. Kurabayashi, and S.J. Skerlos, "PDMS-based opto-fluidic micro flow cytometer with two-color, multi-angle fluorescence detection capability using PIN photodiodes," *Sensors and Actuators B* 98, 356-367 (2004).
- [21] A. Enciso-Martinez, E. van der Pol, A.T. Lenferink, L.W. Terstappen, T.G. Van Leeuwen, "Synchronized Rayleigh and Raman scattering for the characterization of single optically trapped extracellular vesicles," *Nanomedicine: nanotechnology, biology and medicine* 24, 102109 (2020).
- [22] E. van der Pol, L. de Rond, F. A. Coumans, E.L. Gool, A.N. Böing, "Absolute sizing and label-free identification of extracellular vesicles by flow cytometry," *Nanomedicine: Nanotechnology, Biology and Medicine* 14(3), 801-810 (2018).
- [23] P. Kukura, H. Ewers, C. Müller, A. Renn, A. Helenius, V. Sandoghdar, "High-speed nanoscopic tracking of the position and orientation of a single virus," *Nature Methods*. 6 (12), 923-927 (2009).
- [24] A. Mitra, B. Deutsch, F. Ignatovich, C. Dykes, and L. Novotny, "Nano-optofluidic detection of single viruses and nanoparticles," *ACS Nano* 4(3), 1305-1312 (2010).

# Appendices



# A

## Particle tracking algorithm

This appendix provides a description of the particle tracking algorithm employed for the estimation of the location as a function of time of trapped polystyrene beads and spores in chapters 3 and 4, respectively, trapped within the multi-waveguide optical traps comprising 2 waveguides and 16 waveguides.

The algorithm for estimating and tracking the position of a particle throughout a sequence of image frames starts by identifying the particle amongst all other image structures within each frame. To that end we carry out a matched filtering procedure on each image frame to identify the sought for particle [1]. In a matched filtering procedure, an image of the particle in question is taken from the first frame in the frame sequence and is then used as a template. This is done by defining a region in the image that is small enough to include only the particle of interest. The template is then applied as a 2D filter for computing the 2D auto-correlation between the image frame and template. The maximum 2D auto-correlation value is obtained at the location of the particle within the image under analysis which defined the optimum match with the template. The next step is estimating the particle location with sub-pixel accuracy. This is achieved by interpolating the global maximum of each 2D auto-correlation maps from the template matching procedure with a 2D parabola fit. The 2D parabola fit is carried-out within a  $\sqrt{2} \cdot 2.5$  pixel radius of the auto-correlation global maximum, which is a surface comprising 25 pixels in total. The coordinates corresponding to the parabola maximum are the sub-pixel estimation of the particle.

The estimation error of the method is assessed by applying the full particle tracking algorithm to sequences of simulated  $1 \mu\text{m}$  bead images. Each bead image is simulated first by generating a binary circle template around the center of an  $N \times N$  grid, taking square grid pixels and pixel dimension  $\Delta = 20 \text{ nm}$ . Then random horizontal and vertical displacements of the circle center with respect to the grid center  $\Delta x$  and  $\Delta y$ , respectively, are generated using a normally distributed random number generator. The standard deviations  $\sigma_{x,\text{sim}} = \sigma_{y,\text{sim}} = \sigma_{\text{sim}}$  in  $\Delta x$  and  $\Delta y$ , respectively, are generated from trap stiffness values  $k_{\text{sim}}$  via the relation  $\sigma_{\text{sim}} = \sqrt{k_B T / k_{\text{sim}}}$  and are converted to pixel dimensions through  $\Delta$ . In this way the sub-pixel estimation accuracy of the particle tracking algorithm can be translated to accuracy in estimated  $\sigma_{\text{est}}$  and  $k_{\text{est}}$  values. The  $k_{\text{sim}}$  values are generated somewhat arbitrarily by taking the normalized experimental trap stiffness for a polystyrene bead in a 16 waveguide trap,  $k_{x,\text{exp},16} = 0.92 \text{ pNnm}^{-1} \text{ mW}^{-1}$ , from chapter 3 and computing  $k_{\text{sim}}$  values at five optical powers,  $P_{\text{sim}}$ , between 0 and 100 mW.

At each  $P_{\text{sim}}$ , we generate a sequence of 1000 circle templates with different combinations of  $\Delta x$  and  $\Delta y$ . The circle templates, which represent optical intensity field values from the simulated bead in the object space of the imaging system,

$I_{\text{object}}(x_1, y_1)$ , are then converted into bead optical intensity field values in the image space,  $I_{\text{image}}(x_2, y_2)$ , and thus bead images with the relation:

$$\tilde{I}_{\text{image}}(f_x, f_y) = \tilde{H}(f_x, f_y) \cdot \tilde{I}_{\text{object}}(f_x, f_y) \quad (\text{A.1})$$

where  $\tilde{I}_{\text{image}}$  and  $\tilde{I}_{\text{object}}$  are the 2D Fourier transforms of  $I_{\text{image}}(x_2, y_2)$  and  $I_{\text{object}}(x_1, y_1)$ , respectively, with spatial frequencies  $f_x$  and  $f_y$  along the  $x$  and  $y$  axis, respectively. Moreover, the image space coordinates  $(x_2, y_2)$  and object space coordinates  $(x_1, y_1)$  are proportionally related via the imaging magnification,  $M$ , as  $x_2 = Mx_1$  and  $y_2 = My_1$ . The incoherent optical transfer function  $\tilde{H}(f_x, f_y)$  is taken to be [2]:

$$\tilde{H}(f_x, f_y) = \frac{2}{\pi} \left[ \arccos \left( \frac{\sqrt{f_x^2 + f_y^2}}{2NA/\lambda} \right) - \left( \frac{\sqrt{f_x^2 + f_y^2}}{2NA/\lambda} \right) \sqrt{1 - \left( \frac{\sqrt{f_x^2 + f_y^2}}{2NA/\lambda} \right)^2} \right] \quad (\text{A.2})$$

where  $NA = 1.2$  is the numerical aperture of the objective lens used within the laser tweezing Raman microscope used in chapters 3 and 4, and the wavelength  $\lambda = 0.5\mu\text{m}$ . The intensity field of the bead image,  $I_{\text{image}}(x_2, y_2)$ , is obtained from an inverse Fourier transform of  $\tilde{I}_{\text{image}}(f_x, f_y)$ . Figures A.1 a) and b) illustrates one of the object and image imaging intensity pairs for a simulated  $1\mu\text{m}$  bead.

The final step in simulating the bead images is the addition of image noise. The noise in current cameras is predominantly Poisson/shot noise. The number of incident photons per pixel is estimated from the ADU counts with the camera specifications including temporal dark noise, bit depth, saturation capacity and the quantum efficiency. This data is listed in the camera specification sheet in [3]. Poisson noise is generated for each pixel with the Matlab poisrnd function using the estimated photon number. An example simulated bead image including Poisson noise is illustrated in Figure A.1c).

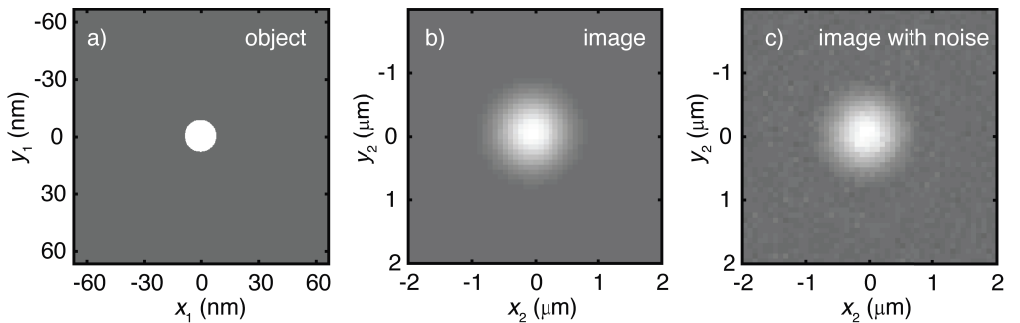


Figure A.1: a) The simulated bead imaging intensity field in the object space and b) the conjugate imaging intensity field in the image space resulting from incoherent imaging and image system magnification,  $M = 60$ , without Poisson noise, and c) with Poisson noise.

The sequence of simulated bead images including noise is then inserted into the particle position estimation algorithm. A subset of the estimated bead positions in the  $x$ - and  $y$ -direction is shown in Figs. A.2 a) and b), respectively.

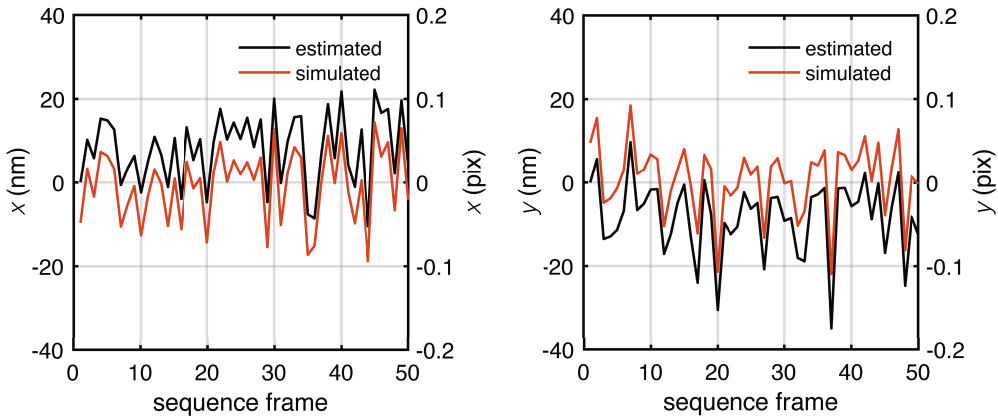


Figure A.2: The simulated  $1\ \mu\text{m}$  bead position and estimated, with the particle tracking algorithm, bead position in a) the  $x$ -direction and b) the  $y$ -direction. The simulated bead positions are generated with  $P_{\text{sim}} = 50\ \text{mW}$ . In both the plots, the left-side axis shows the bead positions in nm and the right-side axis shows the corresponding pixel values.

Comparison between the estimated bead positions and the simulated ones seem to show a systematic offset between the two. This is confirmed through analysis of the statistics of the difference in estimated and simulated bead position traces, as is shown in figure A.2.

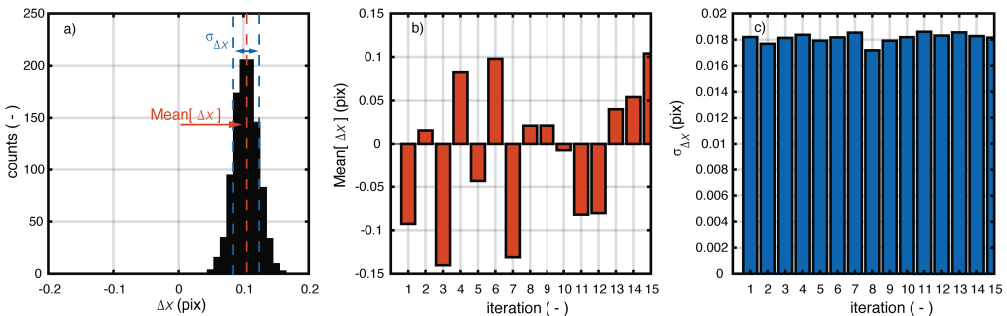


Figure A.3: The distribution of the difference between estimated and simulated bead positions in the  $x$ -direction in pixels and generated for bead diameter of  $1\ \mu\text{m}$  with  $P_{\text{sim}} = 50\ \text{mW}$ . The red arrow and dotted line shows displacement of histogram center with the origin,  $\text{Mean}[\Delta x]$ , showing tracking algorithm accuracy. The blue arrow and dotted lines indicate the histogram width in terms of standard deviation,  $\sigma_{\Delta x}$ , showing tracking algorithm precision. The variability in b)  $\text{Mean}[\Delta x]$  and c)  $\sigma_{\Delta x}$  between 15 estimation iterations with each iteration containing 1000 estimated bead positions. Results for the  $y$ -direction omitted as the behaviour is identical.

The histogram in difference of estimated and simulated bead position is centered approximately around 0.1 pixel. This confirms the systematic offset between estimated and simulated bead position shown in figure A.2. Furthermore, the offset for 15 iterations of the particle tracking algorithm, each with 1000 estimated positions, reveals varying offset values between tracking runs. Further investigation shows that the offset is caused by choice of template, chosen at the start of each tracking run, which is why the offset is constant with a tracking run and varies between tracking

runs. Such biases are known to occur in position estimation procedures based on maximizing a cross-correlation [4]. On the other hand, the width of the histogram in difference of estimated and simulated bead position fluctuates around 0.018 pix. Consequently, the precision of the particle tracking algorithm is around  $3 \sigma_{\Delta x} = 0.054$  pix.

Estimated trap stiffness values,  $k_{\text{est}}$ , are computed via  $k_{\text{est}} = k_B \cdot T / \sigma_{\text{est}}^2$  where  $k_B$  and  $T$  are Boltzman's constant and temperature, respectively. The  $\sigma_{\text{est}}$  is the standard deviation in the estimated position series resulting from a single particle tracking run. Based on above results, the  $\sigma_{\text{est}}$  and  $k_{\text{est}}$  are only limited by the precision of the particle tracking algorithm. The  $\sigma_{\text{est}}$  and  $k_{\text{est}}$  for  $1 \mu\text{m}$  and  $3 \mu\text{m}$  are shown in figure A.4 for corresponding  $P_{\text{sim}} \in [10, 100]$  mW together with  $\sigma_{\text{sim}}$  and  $k_{\text{sim}}$ , respectively, to illustrate the estimation error in  $\sigma$  and  $k$  achieved with the particle tracking algorithm.

For the  $1 \mu\text{m}$  bead,  $\sigma_{\text{est}}$  agrees well with  $\sigma_{\text{sim}}$  for  $\sigma_{\text{sim}} \gtrsim 10$  nm, corresponding approximately to 0.125 pix and  $P_{\text{sim}} = 50$  mW. While for smaller  $\sigma_{\text{sim}}$ , the discrepancies between  $\sigma_{\text{sim}}$  and  $\sigma_{\text{est}}$  become larger as  $\sigma_{\text{est}}$  approaches the position estimation precision limit of 0.054 pix with  $\sigma_{\text{est}} \approx 0.075$  pixel at  $P_{\text{sim}} = 100$  mW. This leads to an underestimation of  $k_{\text{est}}$  and a deviation from the expected linear relationship between  $k_{\text{est}}$  and  $P_{\text{sim}}$ , clearly apparent in figures A.4 (c) and (d) for  $k_{\text{est}} \gtrsim 0.04 \text{ pNnm}^{-1}$ .

On the other hand for the  $3 \mu\text{m}$  bead,  $\sigma_{\text{est}}$  agree well with  $\sigma_{\text{sim}}$  as small as 8.5 nm corresponding to 0.105 pix. This becomes more apparent from the  $k_{\text{est}}$  in figures A.4 (c) and (d) where the agreement with  $k_{\text{sim}}$  and thus the expected linear relationship with  $P_{\text{sim}}$  is extended to  $k_{\text{sim}}$  as high as  $0.06 \text{ pNnm}^{-1}$ . A higher estimation precision for larger bead sizes is expected as the image contains more pixels contributing to the generation of the 2D autocorrelation correlation curve, which leads to a broader autocorrelation curve. As a result, the autocorrelation curve extremum becomes smoother and the 2D parabolic fit for subpixel particle position becomes more precise.

Further inspection in figure A.4 (e) shows an average discrepancy of between  $k_{\text{est}}$  and  $k_{\text{sim}}$  below 5 % for  $k_{\text{sim}} \lesssim 0.03 \text{ pNnm}^{-1}$  for both the  $1$  and  $3 \mu\text{m}$  beads. As  $k_{\text{sim}}$  increases beyond  $0.03 \text{ pNnm}^{-1}$ , the discrepancy between  $k_{\text{sim}}$  and  $k_{\text{est}}$  becomes larger as  $k_{\text{est}}$  is increasingly and systematically underestimated, a consequence of the particle tracking precision limit.

In chapter 3, the stiffness values determined for  $1 \mu\text{m}$  polystyrene beads range between  $0.01 \text{ pNnm}^{-1}$  and  $0.08 \text{ pNnm}^{-1}$ , as is shown in figure 3.8 (a). Here, the trap stiffness values for  $k_{y,2(16)\text{wg}}$  are all below  $0.02 \text{ pNnm}^{-1}$  and are a good estimate of the actual trap stiffness according to the prediction shown in figure A.4 (e). This is further confirmed through the linear relationship with the optical power  $P_{\text{trap}}$  exhibited by the experimentally determined  $k_{y,2(16)\text{wg}}$ . The  $k_{x,16\text{wg}}$  values increase up to  $0.051 \text{ pNnm}^{-1}$  and also exhibit linear behaviour with  $P_{\text{trap}}$ . However the  $k_{x,16\text{wg}}$  data-set also contains points slightly deviating from linear behaviour both at low stiffness values as  $0.01 \text{ pNnm}^{-1}$  and at high values as  $0.051 \text{ pNnm}^{-1}$ . In the same way the  $k_{x,2\text{wg}}$  values also exhibit a linear relationship with  $P_{\text{trap}}$  for stiffness values as high as  $0.07 \text{ pNnm}^{-1}$ , also with slight deviations from linear behaviour. These deviations can be caused by several effects.

Firstly, the  $k_{x,2(16)\text{wg}}$  data visualised in chapter 3 each result from a single measurement while from figure A.4 (e) the stiffness is expected to vary by  $\pm 5\%$  of the ground truth. As a result, the deviating  $k_{x,2(16)\text{wg}}$  values may be less precise estimates.

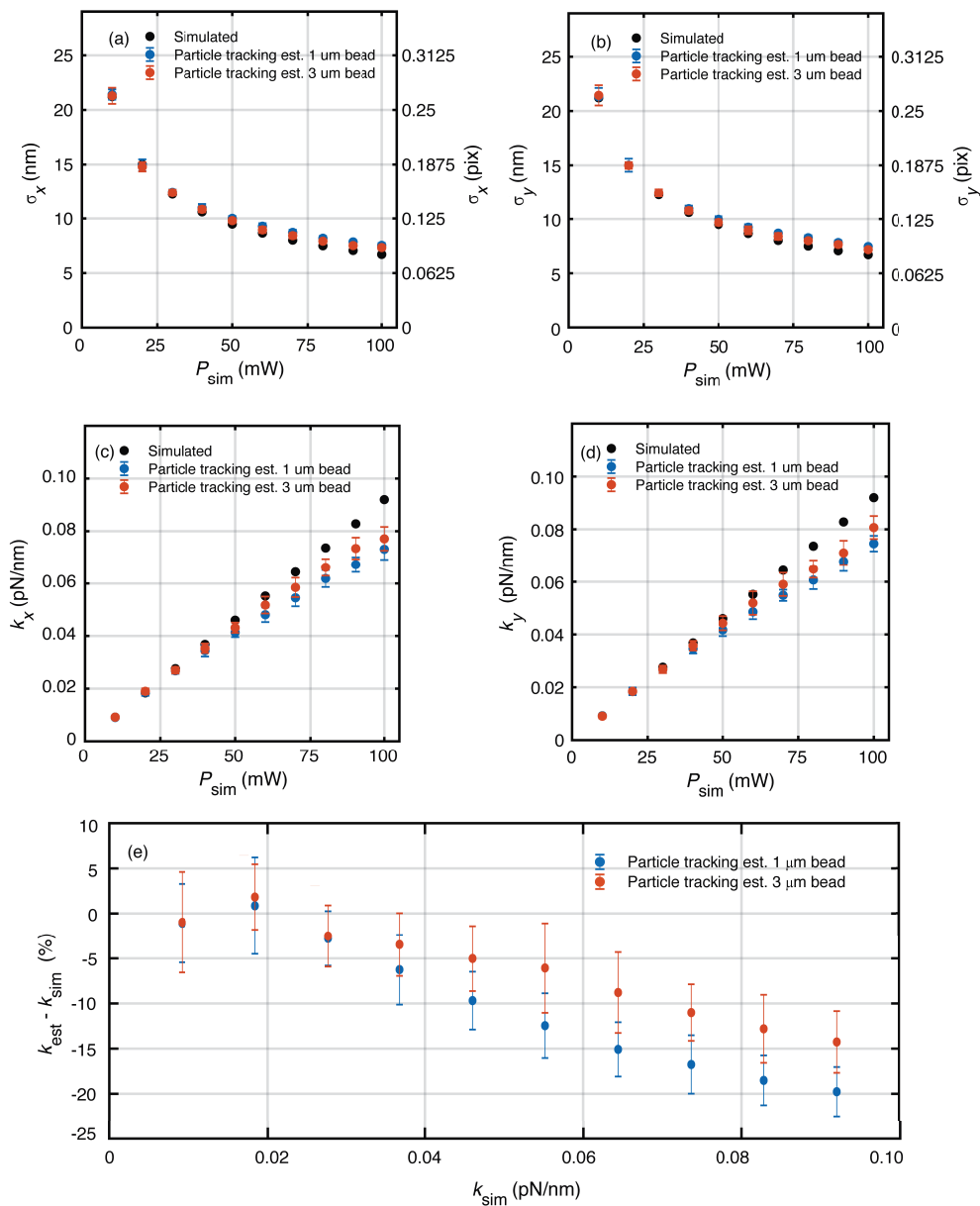


Figure A.4: The standard deviation in simulated bead position (black) and estimated bead position for a 1  $\mu\text{m}$  bead (blue) and 3  $\mu\text{m}$  bead (red), using the particle tracking algorithm in a) the  $x$ -direction and b)  $y$ -direction, and the corresponding trap stiffness in c) the  $x$ -direction and d)  $y$ -direction. In a) and b) the  $\sigma$  values are illustrated both in nm and corresponding pixel dimensions. e) shows the accuracy and precision of the estimated trap stiffness as a function of the simulated trap stiffness, employing the estimated trap stiffness data of both the  $x$ -direction and  $y$ -direction.

However according to figure A.4, stiffness values above 0.03  $\text{pNnm}^{-1}$  are always expected to be underestimated. Secondly, external contributions such as the channel movements which remained unfiltered out of the tracked particle time traces. The

channel movements are explained and shown extensively in chapter 4 lead to larger estimated trapped particle displacement and result in an underestimation of the stiffness. Finally, the simulated bead images presented here may not be an accurate enough representation of the bead images recorded in chapter 3, as the recorded bead image details are not captured in the simplified model employed for the simulated bead images. This may lead to a higher particle tracking precision in chapter 3 than estimated here for the simulated bead images and in turn resulting in a higher estimation accuracy for stiffness values above  $0.04 \text{ pNnm}^{-1}$ .

Moving to the results for the  $3 \mu\text{m}$  polystyrene beads, the stiffness values range between  $0.01 \text{ pNnm}^{-1}$  to  $0.2 \text{ pNnm}^{-1}$  as is shown in figure 3.8 (b). The  $k_{y,2(16)\text{wg}}$  are below  $0.05 \text{ pNnm}^{-1}$  and are expected to be accurate estimates of the actual trap stiffness, according to figure A.4 (e). This is again confirmed through the linear relationship which the  $k_{y,2(16)\text{wg}}$  exhibits with  $P_{\text{trap}}$ . The  $k_{x,2(16)\text{wg}}$  values on the other hand, are as high as  $0.2 \text{ pNnm}^{-1}$  while stiffness values above  $0.04 \text{ pNnm}^{-1}$  are expected to deviate from linear behaviour as the stiffness becomes increasingly inaccurate, as shown in figure A.4. However the  $k_{x,(2)16\text{wg}}$  values up to  $0.1 \text{ pNnm}^{-1}$  all exhibit a good linear relationship with  $P_{\text{trap}}$  which indicates accurate stiffness estimation. These results show that the stiffness accuracy range can be extended to larger stiffness values as the simulated bead images are probably not an accurate representation of the recorded bead images from chapter 3 leading to an underestimation of the accuracy limit of the estimated stiffness values for the trapped beads in chapter 3. However, the  $k_{x,2\text{wg}}$  go up to  $0.2 \text{ pNnm}^{-1}$  and continue to exhibit linear behaviour with  $P_{\text{trap}}$ , except for the two right-most data points in figure 3.8 (b) which appear underestimated. Possible reasons for underestimation of these data points are explained above for the case of a  $1 \mu\text{m}$  bead. Nevertheless, the estimation accuracy of the stiffness for  $3 \mu\text{m}$  beads can apparently be extended at least to  $0.2 \text{ pNnm}^{-1}$ . Furthermore, exclusion of the underestimated data points leads to alignment of the  $k_{y,2\text{wg}}$  and  $k_{y,16\text{wg}}$  lines and equal trapping forces for both traps along the  $x$ -direction. This result is not surprising since the  $3 \mu\text{m}$  bead is large enough to average out rapid spatial variations of the field, leaving the global field variations to contribute to the optical forces, resulting in similar optical force magnitudes for the 2 waveguide and 16 waveguide traps. As the trapped bead becomes smaller the rapid field variations become more dominant leading to a higher trapping force generated by the 16 waveguide trap, which contains stronger field gradients in the trap center.

In chapter 4, the stiffness values determined for the trapped spores are on average  $\leq 0.03 \text{ pNnm}^{-1}$  with a maximum value of  $0.051 \text{ pNnm}^{-1}$ , as shown in figure 4.7. According to figure A.4 (e), the estimated stiffness values for the trapped spores are underestimated by at most 5 % on average, which is acceptable. Moreover the estimated stiffness values in figure 4.7 of chapter 4 show the expected linear relationship with optical  $P_{\text{trap}}$  for all trapped spores.

In future studies, the range of trap stiffness values for which the analysis pipeline applies, could be extended by taking the estimation precision  $\sigma_{\text{prec}}$  into account in determining the distribution of bead or spore positions, by e.g. using  $\sigma = \sqrt{\sigma_{\text{est}}^2 - \sigma_{\text{prec}}^2}$  as the width of the position distributions instead of the apparent width  $\sigma_{\text{est}}$  directly obtained from the particle tracking.

# B

## Expected maximum intensity of a speckle pattern

Consider  $n = 1, 2, \dots, N$  speckle patches with intensity  $I_n$  according to Rayleigh statistics:

$$P(I_n) = \frac{1}{I_0} e^{-\frac{I_n}{I_0}} \quad (\text{B.1})$$

with  $I_0$  the average intensity, i.e. we have:

$$\int_0^{\infty} dI P(I) = 1 \quad (\text{B.2})$$

$$\int_0^{\infty} dI I \cdot P(I) = I_0 \quad (\text{B.3})$$

We look for the expected value of the maximum of the  $N$  speckle intensities:

$$\langle I_{\max} \rangle = \int_0^{+\infty} dI_1 \dots dI_N P(I_1) \dots P(I_N) \max(I_1, \dots, I_N) \quad (\text{B.4})$$

Insertion of equation B.1 gives:

$$\langle I_{\max} \rangle = \frac{1}{I_0^N} \int_0^{\infty} dI_1 \dots dI_N e^{-\frac{I_1 + \dots + I_N}{I_0}} \max(I_1, \dots, I_N) \quad (\text{B.5})$$

To solve equation B.5 we implement a change of variable  $I_j = -I_0 \log(z_j)$  giving  $z_j = e^{-\frac{I_j}{I_0}}$  and  $dI_j = -(I_0/z_j) dz_j$ . This leads to a uniform probability distribution of the  $z_j$  over the interval  $[0, 1]$  and an expected value for the maximum:

$$\frac{\langle I_{\max} \rangle}{I_0} = \int_0^1 dz_1 \dots dz_N \max(-\log(z_1), \dots, -\log(z_N)) \quad (\text{B.6})$$

which can be rewritten to:

$$\frac{\langle I_{\max} \rangle}{I_0} = - \int_0^1 dz_1 \dots dz_N \log(\min(z_1, \dots, z_N)). \quad (\text{B.7})$$

Defining  $z_0 = \min(z_1, \dots, z_N)$  this can also be expressed as:

$$\frac{\langle I_{\max} \rangle}{I_0} = - \int_0^1 dz_0 D(z_0) \log(z_0). \quad (\text{B.8})$$

where  $D(z_0)$  is the Probability Distribution Function (PDF) of  $z_0$ . For one value of  $j$  we have  $z_j = z_0$ , the remaining values  $z_k > z_0$  for all  $k \neq j$ . An expression for  $D(z_0)$  then follows as:

$$D(z_0) = N(1 - z_0)^{N-1} \quad (\text{B.9})$$

Using computer algebra tools (e.g. Wolfram Alpha) it can subsequently be found that:

$$\frac{\langle I_{\max} \rangle}{I_0} = H_N \quad (\text{B.10})$$

where the so-called harmonic number  $H_N$  is defined by:

$$H_N = \sum_{n=1}^N \frac{1}{n} \quad (\text{B.11})$$

## References

- [1] I. T. Young, R. Ligteringen, Stochastic Signal Processing – An Introductory Textbook (2019).
- [2] J. Goodman, Introduction to Fourier optics, Roberts and Company Publishers (2005).
- [3] Allied Vision technologies Gmbh., <https://www.alliedvision.com/en/support/technical-documentation/mako-u-documentation/>
- [4] T. Q. Pham, M. Bezuijen, L.J. van Vliet, K. Schutte, and C.L. Luengo Hendriks, "Performance of optimal registration estimators," In Visual Information Processing XIV 5817, Visual Information Processing XIV(2005)



# Curriculum Vitæ

## G.B. Loozen

Born 15<sup>th</sup> of January 1990 in Willemstad, Curaçao.

### Education

- |           |  |
|-----------|--|
| 2002–2007 | HAVO, scholengemeenschap Bonaire   |
| 2007–2012 | Ing. in Applied Physics<br>The Hague university  |
| 2012–2013 | Bridging programme in Applied Physics<br>Delft University of Technology  |
| 2013–2015 | Ir. in Applied Physics<br>Delft University of Technology   |
|           | <i>Thesis:</i> Monitoring of pulsating flows with dynamic speckle fields   |
| 2015–2019 | Cancer-ID PhD project<br>Quantitative Imaging group<br>Imaging physics department<br>Delft University of Technology                |
|           | <i>Thesis:</i> Towards lab-on-a-chip optical trapping and Raman spectroscopy of extracellular vesicles using multi-waveguide traps |



# List of Publications

## Peer-reviewed articles

3. L.G. Rikkert, Pepijn Beekman, J. Caro, F.A.W. Coumans, A. Enciso-Martinez, G. Jenster, S. le Gac, W. Lee, T.G. van Leeuwen, **G.B. Loozen**, A. Nanou, R. Nieuwland, H.L. Offerhaus, C. Otto, D.M. Pegtel, M.C. Piontek, E. van der Pol, L. de Rond, W.H. Roos, R.B.M. Schasfoort, M.H.M. Wauben, H. Zuillhof, and L.W.M.M. Terstappen, "Cancer-id: Toward identification of cancer by tumor-derived extracellular vesicles in blood", *Frontiers in Oncology* 10, 608 (2020).
2. **G.B. Loozen**, A. Karuna, M.M.R. Fanood, E. Schreuder, and J. Caro, "Integrated photonics multi-waveguide devices for optical trapping and Raman spectroscopy: design, fabrication and performance demonstration", *Beilstein Journal of Nanotechnology* 11, 829–842(2020).
1. **G.B. Loozen**, and J. Caro, "On-chip optical trapping of extracellular vesicles using box-shaped composite  $\text{SiO}_2 - \text{Si}_3\text{N}_4$  waveguides", *Optics express* 26(21), 26985-27000 (2018).

## Conference proceedings

1. M.M. Rafiee Fanood, **G.B. Loozen**, E. Schreuder, and J. Caro, "Multiple-waveguide trapping devices: a 3D-FDTD simulation study", *Proceedings Symposium IEEE Photonics Society Benelux*(2017).

## Oral presentations

1. **G. B. Loozen**, "Multiple-waveguide trapping devices: a 3D FDTD simulation study", Oral presentation at the IEEE Photonics Benelux 2017. November 27-28, 2017, Delft, The Netherlands.

## Poster presentations

1. **G.B. Loozen**, and J. Caro, "Simulation study of optical trapping of vesicles with a dual-waveguide trap", poster at the Annual Meeting-ISEV2016, May 4-7, 2016, Rotterdam, The Netherlands.



# Acknowledgements

With this thesis I close a very challenging, adventurous and educational part of my life which was made possible with the support of many people.

First, I want to thank my supervisor Jaap Caro, who could not be present today, for giving me the opportunity to be involved in this project. Although our collaboration had its ups and downs, I am grateful for the guidance offered throughout the main phase of my PhD.

I also thank Sjoerd Stallinga for guiding and motivating me in the final phases of my PhD to successfully wrap up this thesis and for offering to stand-in as one of my promotors.

I thank my other promotor, Lucas van Vliet, for his supervision throughout the whole process, and his guidance in making important decisions at crucial moments of the PhD process.

A special thanks goes out to Jeroen Heldens, with whom I spent many days collaborating in the lab. I look back on that time with fond memories of the work we carried out together and the conversations we had. On the same note I thank Mohammad and Arnica for their collaboration and contributions during the later stages of my PhD.

I thank my office mates Jos van Rooij and Boling as well as Robert Moerland, Jelle van der Horst, Leon and Christiaan for all their valuable help and support throughout and after my whole PhD period.

Within the Quantitative Imaging group I especially thank Ron, Ronald, Annelies, Angela and Nicolette for all their support and motivation, and for the friendly environment they provided within the group. On the same note I want to thank all of the current and former group members Quantitative Imaging group: Bernd, Jeroen K., Frans, Ted, Anna, Lena, Mojtaba, Jelle S., Pierre, Taylor, Marijn, Ellen, Joost, Aloys, Marten, Hamidreza, Rasmus, Tian, Joor, Jos de W., Yan, Tom, Martijn, Nadia, Jelena, Marco, Davide, Juan Pedro, Kadir, Babak, Emile and Robiël. From the other Imphys sections and other groups within TNW, I want to thank Jack, Alberico, Junhai, Dong, Shan, Nicollo, Laura Maddalena, Mario G., Sarwan, Antonio, Ronan, Mahzar, Soufiane for their collaboration and/or contribution to making my time as a PhD candidate fun and enjoyable. Besides I want to thank Giuseppe Radaelli for his support as well and the enjoyable lunches on campus.

I give a shout out to my fellow PhD candidates within the Cancer-ID program, Agustin, Woojie, Pepijn, Leonie, Afroditi, Melissa and the others including Edwin, Frank, Herman and Cees for the collaborations, interesting meetings, and fun times.

I thank Photonfirst for giving me leeway to write my thesis. Here I want to thank Pim, Thijs, Vincent, Jorrit, Jelmer, Morris, Michael Haverdings, Oscar, Elvis, Maurice, Sven and Michael Sieval for their support.

I am especially grateful to my christian community that has been my existential basis since the day I arrived here in the Netherlands to pursue a higher education and still is my basis to this day. I want too thank by name: Serge & Isabel, Stef & Willemien,

Marcelo & Chantal, Luc, Johnny, Henry, Marco C., Mario A., Jan, Wilson & Nora, Richard & Piedad, Fred & Sandra, Bart & Simona, Jonathan & Kenia, Leroy & Brenda, Francesco & Gloria, Giovanni & Paula, Raffael & Analisa, Cesar & Sara, Thomas & Sara, Luis & Lara, Manuel & Priscila, David & Maddalena, Yamileth, Amanda, Anne-Christie, Karin, Emil, Eric, Dino, Andrzej.

I extend a warm embrace to my dearly departed sister Liliana, thank you for your support and love since my arrival here in the Netherlands and may your soul rest in peace.

I thank the redemptoris mater seminar of nieuwe niederorp, with rectors Luc and Jose Manuel, the seminarians Emil, Eric, Dino, Stefan, Diego, Josue, David, and Matteo, and the elderly sisters, for all their support and offering me a peaceful and structured environment for me to finish writing most of this thesis. On the same note I thank the Gattone family, Marco & Mathilde, Giovanni, Paolo, Filippo, Agnese, Teresa and Francesco, and the Mores Family, Mario & Teresa, Francesco, Maddalena and Chiara.

A very special thanks goes to my brother and sister-in-law, Paolo and Maria-Theresa, cheering me on and supporting me along a large part of the thesis writing process and who also were a driving force in allowing me to meet my dear wife, Damaris.

To my dear friend Marco Marciani, I am thankful for the time we spent together as housemates for nearly six years, and your support and company throughout those years.

To wrap-up I thank my dad, mom, and brother Dylan for loving me and supporting me through thick and thin and finally my wife Damaris for her love, patience, support and motivation, I can honestly say that being with you has made me a better man.